National Physical Laboratory

NPL Report MAT 58

Q-factor Measurement by using a Vector Network Analyser

Andrew P Gregory

DECEMBER 2021

Department for
Business, Energy
& Industrial Strategy

FUNDED BY BEIS

Q-factor Measurement by using a Vector Network Analyser

Andrew P Gregory

Electromagnetic Technologies Group
Electromagnetic and Electrochemical Technologies Department

ABSTRACT

This report describes procedures for automated measurements of Q-factor that are based on a Vector Network Analyser (VNA). An efficient algorithm (NLQFIT) for fitting Q-factor and resonant frequency to swept-frequency complex S-parameter data is outlined. This can be applied to measurements by transmission and by reflection, and can fit the length of uncalibrated line between calibration reference planes and couplers as an option. A weighting scheme to improve measurement precision when the VNA uses a linear frequency sweep is also described. Listings of computer code for Matlab and Python implementations of NLQFIT are given in an appendix. Experimental studies of Q-factor measurements made using both transmission and reflection methods are presented. Aspects that are reported on include measurement repeatability, VNA calibration, measurements using an uncalibrated VNA, simulations of the effect of uncalibrated line sections, traceability, and the effect of varying the VNA power-level setting. The evaluation of the uncertainty associated with Q-factor measurements is studied. An overview of methods for determining dielectric loss angle and the associated uncertainty from measurements of the Q-factor of resonators is presented.

NPL Report MAT 58

ISSN 1754-2979

https://doi.org/10.47120/npl.MAT58

National Physical Laboratory
Hampton Road, Teddington, Middlesex, TW11 0LW

Approved on behalf of NPLML by R. A. Dudley,

Science Area Leader

CONTENTS

TABLES

FIGURES

CODE LISTINGS

Organisation of this report

Section 1 introduces methods for Q-factor measurement by using a Vector Network Analyser, based on equivalent circuit models. An overview of existing publications on this subject is given.

Section 2 describes a new two-stage algorithm (NLQFIT) for fitting Q-factor to complex S-parameter data that can be implemented easily by using matrix arithmetic. Topics discussed include a weighting scheme that provides an optimum fit when the VNA sweep has equal-sized frequency steps (Section 2.4), computation of unloaded Q-factor (Section 2.5) and the practical application of NLQFIT (Section 2.6).

Section 3 considers experimental techniques for measurement of Q-factor by transmission and reflection methods (and which to choose). Aspects that are considered include coupling requirements, the effects of uncalibrated lines, and whether the VNA needs to be calibrated.

Section 4 describes seven experiments that are used to investigate different aspects of Q-factor measurement.

Section 5 considers evaluation of the uncertainty of Q-factor measurements.

Section 6 describes how the loss angle of dielectric materials can be determined from measurements of the Q-factor of resonators. Evaluations of uncertainty are considered.

Section 7 provides conclusions.

Appendix A provides listings of computer code for Matlab[1] / GNU Octave[2] and Python[3] implementations of NLQFIT.

Revision History

December 2021: Initial release.

June 2022: Added references to the implementation of NLQFIT in the scikit-rf open-source library. Minor edits in Section 2.6.

[1] MathWorks Inc., https://uk.mathworks.com/products/matlab.html
[2] Free Software Foundation https://www.gnu.org/software/octave/
[3] Python Software Foundation, https://www.python.org

1 INTRODUCTION

The Q-factor [1–4] of cavities and tuned-circuits can be measured by using modern digital instruments of two main types: Vector Network Analysers (VNAs) and Impedance Analysers. Such instruments may not provide a direct readout of Q-factor, but it can be found either by fitting to swept frequency data or, with less precision, by a simple calculation from a few readings if a marker/cursor facility is available. Practical measurements of Q-factor are straightforward, but to obtain uncertainty ≤ 1% (which is considered to be low for Q-factor measurement) requires attention to several aspects of the experimental procedure. In this report, methods for determining Q-factor from frequency-domain VNA measurements of scattering parameters (S-parameters [5]) are described and compared. A fitting algorithm to improve precision and allow experiments to be automated is presented. Evaluation of the uncertainty of measured Q-factors presents a number of difficulties, which are examined. Some practical methods of obtaining an uncertainty evaluation are suggested. The ability to measure small Q-factor changes is considered as it is particularly important for the measurement of the loss angle of low-loss dielectric materials [4]. The techniques developed can also be applied more generally for characterising resonant circuits used in electronic devices [6], NMR and MRI experiments [7, 8], and wireless charging systems [9, 10].

VNAs are heterodyne systems that use two synthesised microwave sources [11]. The synthesisers are locked to a stable timebase (typically an oven-controlled 10 MHz quartz-crystal oscillator). It is convenient to refer to "swept frequency" measurement of S-parameters, but it should be understood that data is acquired over a staircase of precise frequency steps. This is a key difference from earlier generations of instrument based on analogue "sweepers". Measurements of resonant width are increased because sources are not perfectly "monochromatic". A convolution calculation shows that the measured width is expected to be of the same order as the sum of the width of the resonance and the linewidth of the source (exactly so if both are Lorentzians [12]). In practice, there are other considerations that arise from the complex design of VNAs. Nevertheless, it is possible to measure very high Q-factors by using VNAs because the synthesised signals have very narrow linewidth, and the frequency steps are set very precisely. A VNA locked to a rubidium frequency standard has been used to measure the Q-factor of superconducting cavities ($Q \approx 10^{10}$) [13].

The Q-factor of a resonator is defined by $Q = \dfrac{2\pi U}{\Delta U}$ where U is the average energy stored by the resonator and ΔU is the decrease in the average stored energy per wave cycle at the resonant frequency [1]. Time-domain ("ring down") methods [2] enable measurement of the *loaded* Q-factor Q_L, in which U and ΔU pertain to the entire system comprising of the resonator and the instrument that is used for observing resonances. The time-domain method requires excitation of a resonance followed by a measurement of the exponential decay of the amplitude (or stored energy). Methods of performing time-domain Q-factor measurements are described in references [14–16].

Characterisation of resonances from measurements in the frequency-domain can be achieved through equivalent-circuit models. The faithfulness of these is a prime consideration for the VNA methods of measuring Q-factor that are described in this report.

1.1 EQUIVALENT CIRCUIT MODELS

References [2, 17–19] show how resonators can be represented by equivalent circuit models, such as that shown in Figure 1. These references show that, for a high Q-factor resonator (in practice, $Q_L \gtrsim 100$), the S-parameter response of a resonator measured in a calibrated system with reference planes at the resonator couplings is

$$S = S_D + d\frac{e^{-2j\delta}}{1+jQ_L t}. \tag{1}$$

This equation can be applied to measurements by transmission ($S \equiv S_{21}$ or $S \equiv S_{12}$) or reflection ($S \equiv S_{11}$ or $S \equiv S_{22}$). S-parameters are dimensionless ratios, but by convention are often shown as having dimensions of "Units" (U). The radius of the Polar/Smith chart is One Unit.

Other symbols are defined by:

S_D	The detuned S-parameter measured at frequencies far above or below resonance. *For measurement by transmission* S_D represents the combined effect of leakage between the VNA ports, and mutual and radiative coupling (Figure 1 shows physical leakage paths superimposed on the equivalent circuit). It will be referred to as the leakage vector in this report. *For measurement by reflection* S_D lies on the edge of the polar chart for lossless coupling as off-resonance almost all of the energy is reflected (i.e. $\lvert S_D \rvert = 1$ Unit). A value for the phase angle of S_D cannot be presumed as it depends on the nature of the coupling.
Q_L	The loaded Q-factor.
f_L	The loaded resonant frequency.
f_o	The unloaded resonant frequency.
f	The frequency at which S is measured.
d	The diameter of the Q-circle measured in a calibrated system (Units). Where necessary, the diameters of Port 1 (S_{11}), Port 2 (S_{22}) and transmission (S_{21}) Q-circles are denoted by d_1, d_2 and d_{21} respectively.
δ	A real-valued constant that defines the orientation of the Q-circle.
t	The fractional offset frequency given by $$t = 2\frac{f-f_L}{f_o} \approx 2\frac{f-f_L}{f_L} \tag{2}$$ where $f_o \approx f_L$.

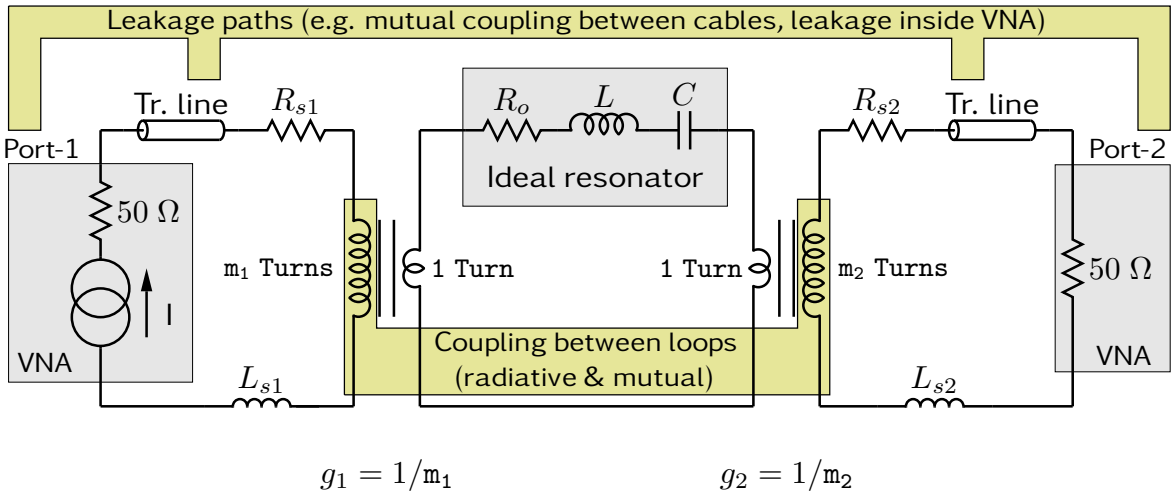

Figure 1: Series LC-circuit representation of transmission measurement of Q-factor for a loop-coupled resonator. Couplings are represented by transformers. Loss associated with couplings is represented by series resistors R_{s1} and R_{s2}. Coupling series inductances are marked L_{s1} and L_{s2}. Transformer turns ratios are represented by g_1 and g_2. Unwanted couplings that can give rise to measurement error are shown in yellow.

Equation (1) can be recognised as a *bilinear transform* (also known as a *Möbius transform* or a *linear fractional transformation*). A property of bilinear transforms is that they map straight lines onto circles and circles onto straight lines on the complex plane [20]. The fractional offset frequency, t, is on the abscissa of the complex plane as it is real valued. Hence, a plot of S as a locus of frequency f over a finite range is a circular arc that is referred to conventionally as a Q-circle (Figure 2). A full circle can never be observed as part of it lies in an unmeasurable range as the minimum frequency of the VNA is above zero and the maximum is below ∞. The point on the Q-circle at $S = S_D$ (where $f = \pm\infty$) is referred to as the pole of the resonance.

Equation (1) can be applied to measurements by transmission and absorption for two-port resonators, and reflection for one-port resonators:

Transmission resonators: For a transmission resonator, the pole of the resonance would be at the origin of the polar chart in the absence of the unwanted couplings shown in Figure 1. In practice, leakage causes it to be offset from the origin by S_D, as shown in Figure 2. The traditional scalar method for determining Q-factor, by finding the "3 dB points" of a sweep of $|S_{21}|$ or $|S_{12}|$ data [4] using the VNA cursor/marker facility requires that $|S_D| \ll d$ for accurate measurement. If this is not the case then the magnitude response becomes asymmetric and the Q-factor measurement is in error. The effect of leakage on measurements is a major theme of this report. Experimental technique for measurement of Q-factor by transmission is discussed in Section 3.1.1.

Absorption resonators: In electronic circuits, two-port absorption resonators are used as "notch" filters that attenuate signals over a small band of frequencies. The detuned transmission coefficient is on the perimeter of the Polar/Smith chart (i.e. $|S_D| = 1$) assuming that other signal paths, such as leakage inside the VNA test-set, are small enough to neglect. Further discussion on this resonator type is deferred to Section 4.7.

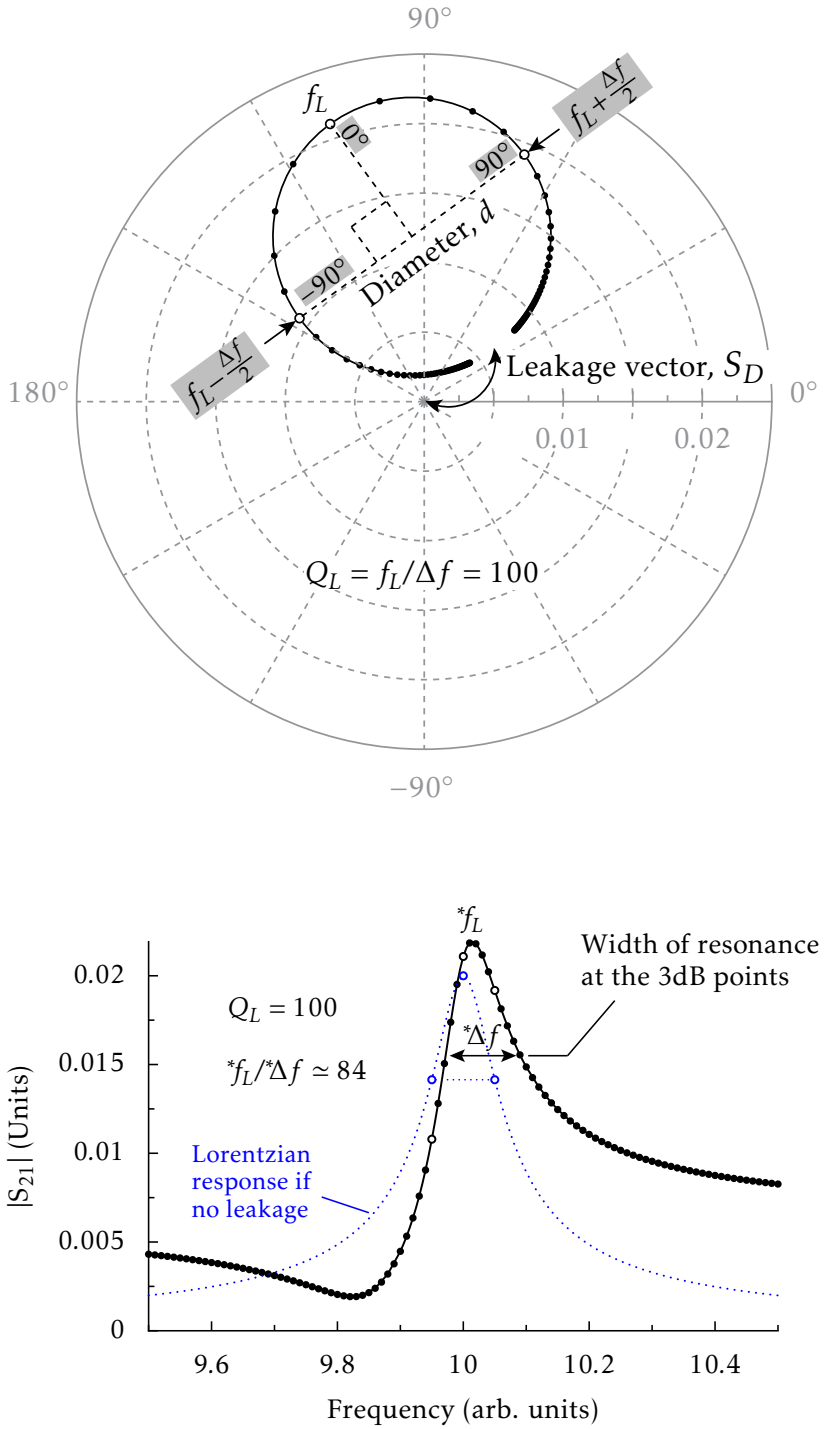

Figure 2: Polar (top) and magnitude vs frequency plots of transmission (S_{21}) at resonance. The resonant frequency and width obtained by the "3 dB points" method are marked with asterisks on the magnitude plot. These show that the "3 dB point" method of measuring of Q-factor is not accurate when there is significant leakage. The -90°, 0° and 90° points are identified with open circles.

Reflection resonators: For lossless coupling, the detuned reflection coefficient is on the perimeter of the Polar/Smith chart (i.e. $|S_D| = 1$) as there is no absorption of energy by the resonator at the extremes of frequency. If loop coupling is used, the shape of the measured Q-circle is modified as a result of loop inductance [21]. For a restricted frequency range close to resonance, however, it approximates to a part of a circle that is inset from the edge of the Polar/Smith chart. For further details, see the discussions below on the calculation of unloaded Q-factor (Section 2.5.1) and on experimental technique (Section 3.1.2).

1.2 Modifications for the effects of uncalibrated lines: phase delay and attenuation

If the uncalibrated line sections between the VNA calibration reference planes and the resonator couplings (Figure 3) are attenuating, then calibrated S-parameter measurements can to a good approximation be described by a modified form of equation (1),

$$S_a = \alpha(f)\, e^{-\mathrm{j}\phi} e^{-\mathrm{j}\Delta\phi} \left[S_D + d\, \frac{e^{-2\mathrm{j}\delta}}{1 + \mathrm{j}Q_L t} \right], \tag{3}$$

where ϕ and $\Delta\phi$ represent constant and frequency-dependent phase delays given by

$$\phi = 2\pi \bar{l} \sqrt{\epsilon_r}\, f_L / c \tag{4}$$

and

$$\Delta\phi = 2\pi \bar{l} \sqrt{\epsilon_r}\, (f - f_L) / c\,. \tag{5}$$

Other symbols not previously defined are:

$\alpha(f)$	A real-valued number (≤ 1.0) that describes transmission through uncalibrated line sections as a function of frequency. The value of $\alpha(f)$ is determined by mismatches and losses (in dielectrics and metal conductors) associated with the uncalibrated lines.
$\bar{l}$	$\bar{l} = \ell$ *For measurement of Q-factor by transmission.* $\bar{l} = 2\ell$ *For measurement of Q-factor by reflection.*
ℓ	The physical length of uncalibrated coaxial line sections (see Figure 3). For transmission measurements this is the total length for both ports.
c	The velocity of light in a vacuum.
ϵ_r	The relative permittivity of the dielectric between the coaxial conductors of the uncalibrated lines (real valued). For a composite air/polymer dielectric, ϵ_r is the effective permittivity.

The quantity S_D in equation (3) is a frequency-independent leakage term that describes leakage signals between resonator couplings due to mutual or radiative coupling. Leakage signals elsewhere, such as mutual coupling between cables [22] and leakage inside the VNA test set, also occur. These are described only approximately by S_D, but are usually at an insignificant level unless very weak coupling is used.

Q-factor measurements are made within a narrowband of frequencies. This enables equation (3) to be simplified and made applicable for measurements with an uncalibrated VNA by making two assumptions:

$$\alpha(f) \approx \text{Const.} \quad S \approx S_m \times \text{Const.} \tag{6}$$

where the two constants are scalar. S_m is described by

S_m | The complex S-parameter of a resonator that is measured by the VNA (calibrated or uncalibrated). The resonator is connected to the VNA via uncalibrated lines. Measurements of S_m are affected by noise and, unless 50 Ω characteristic impedance is maintained throughout the uncalibrated lines, by multi-path effects. Additional multi-path effects occur if an uncalibrated VNA is used.

If the constants are combined, the following equation is obtained:

$$A\, S_m = e^{-\mathrm{j}\phi} e^{-\mathrm{j}\Delta\phi} \left[S_D + d \frac{e^{-2\mathrm{j}\delta}}{1 + \mathrm{j} Q_L t} \right] \tag{7}$$

where A is described by

A | A real-valued scaling-factor that allows magnitude corrections to be applied when the VNA is uncalibrated, or when the uncalibrated lines attenuate the signal. It is assumed to be independent of frequency within the measured range and is, in effect, the calibration coefficient for a scalar response calibration at reference plane(s) at the resonator coupling(s). A_{11}, A_{22} and A_{21} are the scaling factors associated with S_{11}, S_{22} and S_{21} respectively.

According to this definition, A can never be less than unity if the VNA is calibrated. The value of A is needed to obtain the unloaded Q-factor Q_o (Section 2.5).

1.2.1 Rotational transformation of the Q-circle as a result of phase delay

The Q-circle is subject to a rotational transformation around the centre of the Polar/Smith chart by the angle $-\phi$. The value of ϕ will in practice be subject to uncertainty as the lengths and propagation constants of uncalibrated lines will themselves have an associated uncertainty. The phase centre (the location of the origin of emitted fields) of couplings is not known precisely, which could be a significant consideration if large loops or probes are used.

The symbol S_V is used to represent the rotated de-tuned complex S-parameter. It is defined by

$$S_V = S_D e^{-\mathrm{j}\phi}. \tag{8}$$

If the VNA is used uncalibrated, the reference planes for phase measurement will not be exactly at the VNA ports so the value of ϕ will be modified.

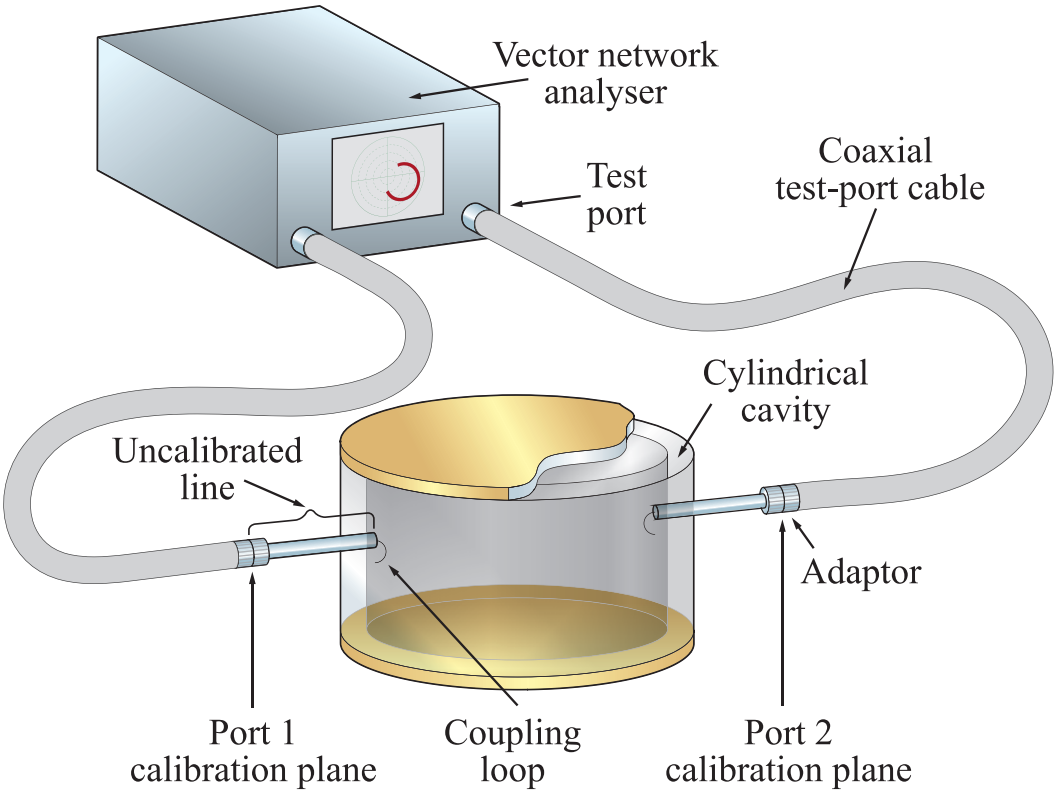

Figure 3: A typical experimental set up for Q-factor measurement by transmission. If vector measurements are made, the locations of phase reference planes must be considered. For uncalibrated measurements these are not well defined, but in practice are usually close to the ports on the VNA's front panel. If a calibration is used the reference planes are precise locations chosen by the experimenter (typical locations are marked).

1.2.2 Frequency dependent phase delay, $\Delta\phi$

If $\Delta\phi$ is of sufficient size (i.e. cables are long), a non-circular response may be seen on the VNA's polar display (examples are shown later in this report in Figures 9 and 13). In this case, determinations of Q-factor by fitting that use complex data will be in error unless the uncalibrated line sections are accounted for (although measurements by scalar methods are unaffected). The effect of uncalibrated lines can be characterised in terms of the unsigned change in phase delay caused by uncalibrated line between 0° (at the resonant frequency) and the 90° point of the Q-circle (see Figure 2), which is given by

$$\Delta\phi_w = 180\,\bar{l}\,\frac{\sqrt{\epsilon_r}}{c}\,\frac{f_L}{Q_L} = 180\,\bar{l}\,\frac{\sqrt{\epsilon_r}}{Q_L\,\lambda_o} \quad \text{degrees.} \tag{9}$$

Modelling (Section 3.3) shows that the effect of uncalibrated lines for typical vector transmission measurements is small unless they are particularly long, or the leakage is high compared to the diameter of the Q-circle. For measurement by reflection, however, comparatively-short uncalibrated lines have a pronounced effect on the shape of Q-circles at microwave frequencies.

1.3 Methods of obtaining Q-factor from swept S-parameter data

Q-factor can be fitted to scalar and vector S-parameter data (reflection or transmission[4]) by using a number of methods. References [23, 24] compare various fitting algorithms. For vector methods, the effects of uncalibrated lines should be considered. Where this is significant, the total length of the uncalibrated line can be included as a fitted parameter (Section 2.3).

1.3.1 Fitting in the complex plane

A least-squares method can be used to fit equation (1) to complex S-parameter data S_i at frequencies f_i where $i = 1 \ldots N$. This is the technique developed in this report. There are a number of approaches to fitting in the complex plane described in the literature. Kajfez [18, 19, 21] develops algorithms in which Q_L is fitted as a complex quantity. The imaginary part, which is small-valued, is discarded. The full detail of Kajfez's method is given in reference [18]. Cox and Jones [25] use a non-linear least-squares routine from a standard library. Faby and Schunemann [26] make a change of variables to obtain equations which are amenable to solution by a linear least-squares method. Inoue et al. [27] use a linear least-squares method of solution for measurement by transmission when S_D can be taken to be zero.

1.3.2 The circle-fitting method

In this method, the position of the centre of the Q-circle is obtained by fitting a circle in the complex plane [24, 28, 29]. The Q-factor and resonant frequency are then obtained from fitting the progression of phase around the measured Q-circle. The circle-fitting technique is particularly appropriate when the measured signal is subject to significant phase noise, as this follows the trajectory of the Q-circle. An example of this arises during measurement of complex permittivity by the Open Resonator [30] method in the author's laboratory. This is because open resonators have very high Q-factor (of the order of 100 000 at 36 GHz), which makes measurements susceptible to the effect of air-pressure variations and environmental vibrations.

[4] In some publications the term Transmission Mode Q-factor (TMQF) is used to describe frequency-domain measurements by transmission.

1.3.3 The scalar fitting method

Figure 2 shows the swept-frequency scalar response of a resonator measured by transmission ($|S_{21}|$ or $|S_{12}|$ data). For an ideal resonator, the observed peak is a Lorentzian. The Q-factor can be obtained by fitting using algorithms described in references [17, 31, 32]. When weak coupling is used, resonances are often observed to be asymmetric on account of leakage. An additional parameter that represents "skew" can be fitted to improve the accuracy of Q-factor measurements when there is leakage [24]. Weak resonances may have a significant noise floor (or background) as random noise is, in effect, rectified. The fitting process can be modified to minimise the effect of the noise floor on measurements [17, 24, 31, 33].

A one-port resonator is highly reflecting except at resonance (where a dip in the magnitude of the reflected signal is observed). Kajfez [34] describes how Q-factor can be fitted to swept-frequency scalar measurements of reflection coefficient ($|S_{11}|$ or $|S_{22}|$ data). The noise floor is not usually a consideration for measurement by reflection because strong coupling is used.

1.3.4 The resonance curve area method

The Resonance Curve Area method [23, 24, 35, 36] uses the fact that Q-factor is inversely proportional to the area underneath the $|S_{21}(f)|$ curve for a Lorentzian measured by transmission. It is assumed that the noise floor and leakage vector do not have significant effect. The area beneath the curve can be calculated numerically.

1.4 Fano resonances

The methods described in this report assume that resonances have Lorentzian form. In multimodal systems, it is assumed that resonances are independent, and that the Q-factor of a mode can be obtained from observations over a limited frequency range. As an aside, the topical subject of *Fano resonance* [37] is introduced. Fano resonances have a non-Lorentzian profile and are therefore not fitted accurately by the algorithms given in this report. They can be simulated in classical systems based on coupled springs [38] and equivalent-circuit models [39, 40]. Numerous papers from the last decade describe scalar observations of Fano resonance from research on optical resonators [41], optical surface-plasmons [42], optical metamaterials [43], and nanomechanical resonators [44].

Fano resonance occurs in systems in which a "bright" mode is excited directly by a signal, and a "dark" mode is excited indirectly via the "bright" mode. If the "dark" mode has high Q-factor, interference effects result in an asymmetric resonance with increased Q-factor. Nakanishi and Kitano [45] describe a scenario in which a microwave split-ring resonator has a pair of eigenmodes that are characterised by symmetric and antisymmetric current flow. These, respectively, result in an induced electric dipole moment and an induced magnetic dipole moment. The symmetric mode can be excited by an external E-field, but the antisymmetric mode cannot and is therefore "dark". If the split-ring is asymmetric, a Fano resonance occurs as there is coupling between these modes. There are a number of papers describing highly-sensitive sensors based on arrays of asymmetric split-rings [46].

2 NLQFIT Algorithm for Fitting Q-Factor to Complex S-parameter Data

This section describes an efficient algorithm for fitting Q-factor and resonant frequency to complex transmission or reflection S-parameter data with uncalibrated line sections ($\ell \neq 0$) as shown in Figure 3. First the simplest case is analysed: when the uncalibrated lines are short ($\Delta\phi_w \approx 0$) and have negligible effect on the shape of measured Q-circles. Equation (7) may then be written in the form

$$S_m = \frac{a't + \mathrm{j}a''t + b' + \mathrm{j}b''}{1 + \mathrm{j}Q_L\, t} \tag{10}$$

where the coefficients a' etc. are real-valued. The difference between the value calculated with the model equation above, and the measured S-parameter S_i at the ith frequency, is given by

$$r_i = S_i - \frac{a't_i + \mathrm{j}a''t_i + b' + \mathrm{j}b''}{1 + \mathrm{j}Q_L\, t_i} \tag{11}$$

where t_i are calculated from the measured frequencies f_i and f_L. A least-squares minimisation of r_i is used to find Q_L, f_L and a' etc. The de-tuned S-parameter S_V and the diameter of the Q-circle d can then be calculated. Statistical errors in S_i are assumed to be uncorrelated across the frequency sweep. It is also assumed that there are no correlations between the real and imaginary parts of r_i at each point.

A two-step minimisation process is used to give reliable convergence to a solution; an approximate linear solution followed by a non-linear optimisation.

2.1 Step (1): Approximate Linear Solution

Equation (11) is written as:

$$r_i = y_i S_i - y_i \left[b' + jb'' + \left(a' + ja'' - \mathrm{j}Q_L S_i\right) t_i \right] \tag{12}$$

where the complex quantity y_i is given by

$$y_i = \frac{1}{1 + \mathrm{j}Q_L t_i}. \tag{13}$$

It may be observed that the y_i act only as weighting factors and that if fixed values are assumed then the equation is linear. Therefore, by using an estimate for f_L, a solution for the remaining five coefficients Q_L and a' etc. can be found by using the linear least-squares method [47]. As f_L is not optimised the coefficients obtained cannot be assumed to be accurate, but nevertheless they are useful as initial values in a further process, Step (2). An estimate for f_L can be obtained by searching S_i for the point that has largest magnitude (for transmission), or the smallest magnitude (for reflection). While it is often sufficient to assume that all $y_i = 1$, experiments have shown that for unfavourable conditions, e.g. when the span of the frequency range is much greater than the width of the resonance, convergence in Step (2) is more likely if y_i are calculated using estimates for Q_L and f_L. The estimate of Q_L need only be correct to within an order of magnitude.

The five coefficients are found by minimisation of r_i. Equation (12) becomes:

$$\begin{bmatrix} \text{real}(r_1) \\ \vdots \\ \text{real}(r_N) \\ \text{imag}(r_1) \\ \vdots \\ \text{imag}(r_N) \end{bmatrix} = \boldsymbol{G} - \boldsymbol{M} \begin{bmatrix} a' \\ a'' \\ b' \\ b'' \\ Q_L \end{bmatrix} \tag{14}$$

where

$$\boldsymbol{M} = \begin{bmatrix} \text{real}(y_1 t_1) & -\text{imag}(y_1 t_1) & \text{real}(y_1) & -\text{imag}(y_1) & \text{imag}(S_1 y_1 t_1) \\ \vdots & \vdots & \vdots & \vdots & \vdots \\ \text{real}(y_N t_N) & -\text{imag}(y_N t_N) & \text{real}(y_N) & -\text{imag}(y_N) & \text{imag}(S_N y_N t_N) \\ \text{imag}(y_1 t_1) & \text{real}(y_1 t_1) & \text{imag}(y_1) & \text{real}(y_1) & -\text{real}(S_1 y_1 t_1) \\ \vdots & \vdots & \vdots & \vdots & \vdots \\ \text{imag}(y_N t_N) & \text{real}(y_N t_N) & \text{imag}(y_N) & \text{real}(y_N) & -\text{real}(S_N y_N t_N) \end{bmatrix} \tag{15}$$

and

$$\boldsymbol{G} = \begin{bmatrix} \text{real}(y_1 S_1) \\ \vdots \\ \text{real}(y_N S_N) \\ \text{imag}(y_1 S_1) \\ \vdots \\ \text{imag}(y_N S_N) \end{bmatrix}. \tag{16}$$

The matrix $\boldsymbol{M}$ and the column vector $\boldsymbol{G}$ can be calculated from the measured data. The solution [47] is given by

$$\begin{bmatrix} a' \\ a'' \\ b' \\ b'' \\ Q_L \end{bmatrix} = \boldsymbol{C}^{-1} \boldsymbol{q} \tag{17}$$

in which

$$\boldsymbol{C} = \boldsymbol{M}^T \boldsymbol{P} \boldsymbol{M} \tag{18}$$

and

$$\boldsymbol{q} = \boldsymbol{M}^T \boldsymbol{P} \boldsymbol{G}. \tag{19}$$

The solution vector in equation (17) can be found by a method such as *Gauss-Jordan elimination*. The linear-equation solver in programs such as Matlab can also be used. The matrix $\boldsymbol{P}$ permits *weighting factors* to be applied. If real and imaginary weighting factors are taken to be equal, $\boldsymbol{P}$ is given by

$$\boldsymbol{P} = \begin{bmatrix} W_1 & \cdots & 0 & 0 & \cdots & 0 \\ \vdots & & \vdots & \vdots & & \vdots \\ 0 & \cdots & W_N & 0 & \cdots & 0 \\ 0 & \cdots & 0 & W_1 & \cdots & 0 \\ \vdots & & \vdots & \vdots & & \vdots \\ 0 & \cdots & 0 & 0 & \cdots & W_N \end{bmatrix} \tag{20}$$

where W_i are real-valued weighting factors. In the author's procedure $\boldsymbol{P}$ is omitted in Step (1) for an unweighted fit.

2.2 Step (2): Optimisation

A numerically efficient way to proceed is to optimise the approximate solution and estimated f_L (i.e. six real-valued coefficients) iteratively. The optimisation must now account for y_i comprehensively. Equation (11) can be written as:

$$r_i = S_i - \left[m_1 + \mathrm{j} m_2 + (m_3 + \mathrm{j} m_4)\, y_i \right] \tag{21}$$

in which real valued coefficients are defined by

$$\begin{aligned} m_1 &= a''/m_5 = \mathrm{real}(S_v)/A \\ m_2 &= -a'/m_5 = \mathrm{imag}(S_v)/A \\ m_3 &= b' - m_1 \\ m_4 &= b'' - m_2 \\ m_5 &= Q_L \\ m_6 &= f_{\mathrm{lwst}}\, Q_L / f_L \\ y_i &= \frac{1}{1 + \mathrm{j} Q_L\, t_i} = \frac{1}{1 + 2\mathrm{j}\left(\dfrac{m_6 f_i}{f_{\mathrm{lwst}}} - m_5 \right)} \,. \end{aligned} \tag{22}$$

The lowest frequency f_{lwst} of the measured trace is used as a convenient scaling factor to ensure that m_6 is unit-less, otherwise the matrix equation that must be solved can become badly scaled when the frequency data has a large magnitude (this arises if high-frequency data is given in Hz rather than GHz). The optimisation uses the gradient descent method: Changes Δm_k in m_k (for $k = 1 \ldots 6$) that minimise the summed squares of the real and imaginary parts of e_i in equation (23) are found by using a linear least-squares method similar to that given by equations. (14) to (20), with $\boldsymbol{M}$ and $\boldsymbol{G}$ re-defined for this problem. Then all m_k are updated ($m_k \rightarrow m_k + \Delta m_k$). The process is repeated until convergence is obtained. Initially $\boldsymbol{P}$ is set to the identity matrix for an unweighted fit (weighting factors are discussed in Section 2.4). The values of y_i , given by equation (13), must be re-calculated in each iterative loop using the latest values of m_5 and m_6. The equation for e_i is

$$\begin{bmatrix} \mathrm{real}(e_1) \\ \vdots \\ \mathrm{real}(e_N) \\ \mathrm{imag}(e_1) \\ \vdots \\ \mathrm{imag}(e_N) \end{bmatrix} = \begin{bmatrix} \mathrm{real}(r_1) \\ \vdots \\ \mathrm{real}(r_N) \\ \mathrm{imag}(r_1) \\ \vdots \\ \mathrm{imag}(r_N) \end{bmatrix} - \boldsymbol{M} \begin{bmatrix} \Delta m_1 \\ \Delta m_2 \\ \Delta m_3 \\ \Delta m_4 \\ \Delta m_5 \\ \Delta m_6 \end{bmatrix} \tag{23}$$

where

$$\boldsymbol{M} = - \begin{bmatrix} \mathrm{real}\left(\frac{\partial r}{\partial m_1}\right)_1 & \cdots & \mathrm{real}\left(\frac{\partial r}{\partial m_6}\right)_1 \\ \mathrm{real}\left(\frac{\partial r}{\partial m_1}\right)_N & \cdots & \mathrm{real}\left(\frac{\partial r}{\partial m_6}\right)_N \\ \mathrm{imag}\left(\frac{\partial r}{\partial m_1}\right)_1 & \cdots & \mathrm{imag}\left(\frac{\partial r}{\partial m_6}\right)_1 \\ \mathrm{imag}\left(\frac{\partial r}{\partial m_1}\right)_N & \cdots & \mathrm{imag}\left(\frac{\partial r}{\partial m_6}\right)_N \end{bmatrix} . \tag{24}$$

The partial differentials in equation (24) can be found analytically without much difficulty. They are evaluated for points $i = 1 \cdots N$ as indicated by suffixes. As reasonably accurate initial estimates are available, rapid convergence is obtained and so few iterations are needed. This being the case it can be sufficient to use a fixed number of iterations. It may, however, be preferred to use a suitable test at the end of each iterative loop to verify formally whether or not adequate convergence has been obtained. The method used in the code examples (Appendix A) is to calculate the root weighted mean square deviation between fit and data:

$$\sigma = \sqrt{\frac{\sum_{i=1}^{N} W_i |r_i|^2}{\sum_{i=1}^{N} W_i}} . \tag{25}$$

Convergence can be said to have occurred when the change in σ between one iterative loop and the next is less than a small fraction (e.g. 10^{-5}) of the magnitude of the largest point in the data array S.

2.3 Accounting for phase delay in uncalibrated lines

If there are uncalibrated lines (Figure 3) that have significant length, Q-circles become distorted and so a 6-coefficient fit will be in error. Simulations (see Sections 3.3.1 and 3.3.2) show how the error in fitted Q-factor depends on the frequency, Q-factor, coupling factor, the total length of uncalibrated line ℓ, and (in transmission) the leakage vector. *De-embedding* [5] can be used to correct for such error if ℓ is measured. Alternatively, equations (21) to (24) may be extended to include a real-valued and unit-less phase factor m_7 that accounts for the frequency-dependent phase coefficient $\Delta\phi$ defined by equation (5). Step (2) is modified to fit 7 coefficients. Equation (21) becomes

$$r_i = S_i - \left[m_1 + \mathrm{j}m_2 + (m_3 + \mathrm{j}m_4)\, y_i\right] e^{\mathrm{j}m_7 (f_i - f_L)/f_{\mathrm{lwst}}} \tag{26}$$

where m_7 is related to $\bar{l}$ by

$$m_7 = -\frac{2\pi \bar{l} \sqrt{\epsilon_r}\, f_{\mathrm{lwst}}}{c} \quad \left[\, \bar{l} = \ell \text{ for transmission, } \bar{l} = 2\ell \text{ for reflection} \right] . \tag{27}$$

If $|S_V| \ll d$, then the 7-coefficient fit requires solution of linear equations that are not well conditioned. This has the practical consequence that the optimisation process is less robust for measurement by transmission than by reflection (the 7-coefficient fit is normally used only for reflection measurement). In the author's software, uncalibrated line is de-embedded from the measured S-parameter data using an estimated length, and the initial estimate for m_7 is zero. The shorthand NLQFIT7 is used to indicate that the data is fitted by equation (26) in Step (2).

2.4 Weighting by rate of angular progression (ANGWTS)

In most experiments, S-parameter measurements are made by using a VNA in linear sweep mode (i.e. the frequency points have a regular spacing). This implies that the measured points are clustered in the "tails" (flanks) of the resonance and widely spaced at the peak. It is quite often the case that some departure from the expected Q-circle occurs in the tails, so the clustering of points has the effect of increasing systematic error. These can be reduced by applying weighting factors W_i in proportion to the rate of change of angle with frequency relative to the centre of the Q-circle. In this report, ANGWTS is used as an abbreviation for this weighting scheme. By using calculus, it is found that

$$W_i = \frac{1}{\left[\dfrac{2Q_L\,(f_i - f_L)}{f_L}\right]^2 + 1} . \tag{28}$$

The above weighting factors can be calculated once a provisional unweighted fit has been obtained, and applied in a repeat of Step (2) of the fitting process[6] after assigning them to the diagonal elements of matrix P – see equation (20). Applying ANGWTS reduces errors from the phase delay of uncalibrated lines (see tabulated data in Figure 9, Section 3.3).

Kajfez in his publications [18, 19] describes a weighting function for reducing the effect of statistical variations of the S-parameter data that are uncorrelated with frequency (for example,

[5] Uncalibrated lines are "removed" numerically from S-parameter data by multiplying by $e^{\mathrm{j}2\pi\bar{l}f\sqrt{\epsilon_r}/c}$.

[6] This weighting scheme is applied to all NLQFIT results in this report except where indicated in Figure 9.

VNA receiver noise). ANGWTS and Kajfez weighting schemes both give a higher weight at resonance than in the tails, and in this respect are similar. Only the ANGWTS scheme is applied for the NLQFIT results given in this report.

2.5 Estimation of unloaded Q-factor, Q_o

The *loaded* Q-factor, Q_L, describes energy dissipation within the entire resonant system comprising of the resonator itself and the instrument used for observing resonances – see Section 1. Historically, Q_L was sometimes referred to as the *indicated* Q-factor. The term *loading* refers to the effect that the *external circuit* has on measured quantities. The external circuit consists of the measuring instrument and uncalibrated lines, but not the couplings of microwave resonators. Loading by an instrument that has 50 Ω impedance, such as a VNA, causes Q_L to be reduced substantially if strong coupling is used. Its effect on the resonant frequency (*frequency pulling*), however, is usually small enough to neglect.

For most applications the quantity that is desired is the *unloaded* Q-factor Q_o, which is determined by energy dissipation associated with the resonator only and therefore gives the best description of the resonant mode. In other words, Q_o is the Q-factor of the uncoupled resonator. The value of Q_o can be estimated from measurements of Q_L, but cannot be measured directly. For the closed cavity-resonator shown in Figure 3, Q_o is largely governed by ohmic loss arising from surface currents in the metal conductors (walls and loop couplings), and from dielectric loss in any insulating materials that may be present.

Energy dissipation in the external circuit is characterised by the *external* Q-factor, Q_e. For both series and parallel equivalent circuits, the three Q-factors are related by

$$\frac{1}{Q_L} = \frac{1}{Q_o} + \frac{1}{Q_e}. \tag{29}$$

The coupling factor β is defined by [1–3]

$$\beta = \frac{Q_o}{Q_e}. \tag{30}$$

For a two-port resonator, designed for measurement by transmission, a coupling factor is defined for each port. The diameter of the Q-circle displayed by the VNA provides a visual indication of whether the coupling is strong or weak. There are many publications that can be consulted for more information on coupling factors (see references [1–3, 18, 48] for example).

Q_o can be calculated from the measured Q_L when coupling factor(s) are known, Analysis of equivalent circuits [2, 18, 19, 21, 34] shows that coupling factors can be calculated from calibrated Q-circle diameters. From the parameters fitted by NLQFIT to swept S-parameter data the Q-circle diameter, d is given by

$$d = A|b + \mathrm{j}a/Q_L| \tag{31}$$

where equations (22) are used to calculate the complex values $a = a' + \mathrm{j}a''$ and $b = b' + \mathrm{j}b''$ from the fitted coefficients. Equation (31) follows from equation (10) as tuned and detuned points on the Q-circle are diametrically opposite. The magnitude correction factor A will depend on which S-parameter is measured for a two-port resonator.

2.5.1 Calculation of Q_o from reflection measurements

The series inductance of the coupling of a loop-coupled cavity causes the Q-circle to become distorted (Section 3.1.2). Nevertheless, for a limited range of frequency centred on the resonance, it approximates to a circle that is inset from the edge of the Polar/Smith chart (i.e. $|S_V| < 1$ Unit, where $|S_V|$ is defined by equation (8)). Figure 4 shows the expected Q-circle for a loop coupling. Precise observation of $|S_V|$ requires the VNA to be calibrated and attenuation in the uncalibrated line to be negligible. If this is the case and loop coupling is used, *Method 2* (below) can be used to calculate Q_o. *Method 1* is preferred when the series inductance of the coupling is low enough to neglect as a relative value for $|S_V|$ then suffices for calculating Q_o.

The coupling factor β is given by [18, 19, 21, 34]

$$\beta = \frac{1}{\frac{D}{d} - 1} \tag{32}$$

where D is the diameter of the *touching circle*, defined by Kajfez [19] and marked on Figure 4. Q_o is then found easily, as from equations (29) and (30)

$$Q_o = Q_L\left(1+\beta\right). \tag{33}$$

Method 1 (generally suitable for undercoupled resonators): If the coupling series impedance is assumed to be zero, the calibrated detuned magnitude $|S_V|$ must be 1 Unit as the resonator effectively acts as a short-circuit at frequencies far above or below resonance (refer to the equivalent circuit, Figure 8). Therefore, the scaling factor A (page 6) can be calculated from a fit to S-parameter data when there is uncalibrated attenuation (or the VNA is not calibrated). It is given by

$$A = 1/(|m_1 + \mathrm{j}m_2|)\ . \tag{34}$$

Alternatively, A can be estimated by measuring the reflection coefficient "off resonance" by de-tuning the resonator or changing the frequency; $A_{11} = 1/|S11|$ if the resonator is attached to port 1. The calibrated Q-circle diameter d can now be obtained using equation (31). Q_o can be determined using equations (32) and (33), where D = 2 Units, that is, the diameter of the Polar/Smith chart.

Practical measurements on reflection resonators are normally made with $0.1 < d < 1.0$ Units, so the above correction is very significant. *Method 1* can be used to correct for attenuation in the uncalibrated line in a system in which the VNA is calibrated. It can also be applied if the VNA is uncalibrated, although multi-path effects will cause some loss of precision.

Method 2 (use for coupling with a large loop): This method requires a calibrated VNA to be used. Normally, the calibration reference plane would be located close to the coupling, so that attenuation in the uncalibrated line is small enough to neglect and $A = 1$. If the reactance of the coupling is assumed not to change significantly within the measured frequency range, the Q-circle is undistorted but inset from the edge of the Polar/Smith chart [21]. An expression for D, equation (35), can be derived [18, 19], using an equivalent circuit that incorporates the

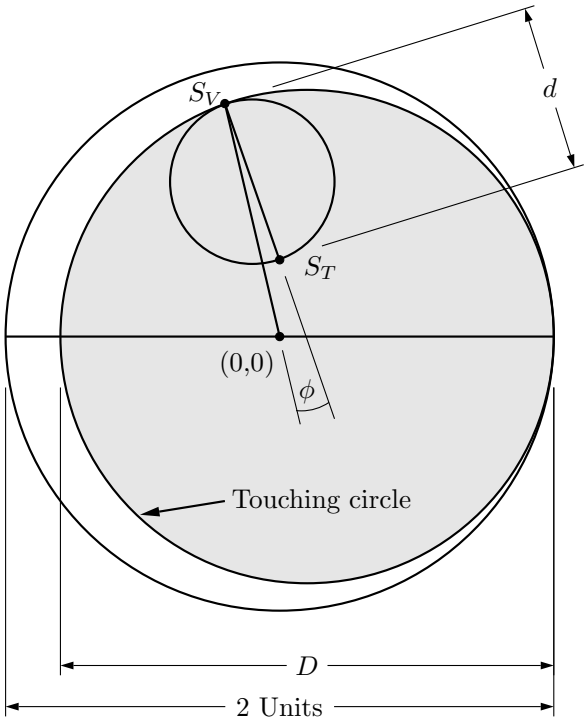

Figure 4: S_{11} of a resonator with loop coupling plotted on the complex plane (based on Kajfez [18, 19]). The touching circle touches the circumferences of the Q-circle and the polar chart.

series inductance of the coupling (Figure 8). Q_o can then be determined using equations (32) and (33) using

$$D = \frac{1-|S_V|^2}{1-|S_V|\cos(\phi)} \tag{35}$$

where

$$\cos(\phi) = \frac{|S_V|^2 + d^2 - |S_T|^2}{2d|S_V|} \tag{36}$$

in which the tuned reflection coefficient is

$$S_T = Ab = A(m_1 + m_3 + \mathrm{j}m_2 + \mathrm{j}m_4). \tag{37}$$

If the coupling inductance is low, then the equivalent circuit (Section 3.1.2, Figure 8) becomes close to that of an ideal three-component RLC resonator, so the magnitude of the reflection coefficient off-resonance $|S_v| \approx 1$ and the diameter of the touching circle $D \approx 2$. Measurements using a small loop coupling given in Table 6 (Section 4.2) provide practical evidence that Q_o results obtained by *Method 1* and *Method 2* do not, in this case, differ significantly. When $|S_v|$ is close to 1, *Method 1* would normally be preferred because the value of D calculated with equation (35) for *Method 2* is sensitive to small errors in the data.

2.5.2 Calculation of Q_o from transmission measurements

The equivalent circuit, Figure 1, shows that dissipation in the couplings (in R_{s1} and R_{s2}) and in the resonator (in R_o) cannot be distinguished by measurement of S_{21} or S_{12} alone. Without additional data Q_o can only, therefore, be calculated assuming that the coupling loss is negligible. For cavity resonators with weak coupling, this is normally a realistic assumption for transmission measurements of Q-factor.

If the VNA is calibrated and any uncalibrated lines are matched and do not attenuate the signal, then the scaling factor $A_{21} = 1.0$. If this does not apply, then calculation of Q_o requires A_{S21} to be measured by a suitable procedure. The attenuation of transmission lines is frequency dependent, so this measurement must be performed at (or close to) the resonant frequency. A_{S21} can be taken to be $1/|S_{21}|$ measured if the resonator is replaced by a "thru" (i.e. direct) connection.

Ideally the "thru" connection would be made between coupling planes, but in practice there will be uncalibrated line sections that remain uncharacterised; for example, the semi-rigid cables that are often used as couplers (Figure 5) for cavity resonators. For a weakly-coupled resonator these usually have a marginal effect. They can, if necessary, be conveniently accounted for by determining A_{21} using the same length of the same type of cable as the "thru". An alternative approach is to measure their attenuations and apply them as a correction. If coupling loss can be neglected, this can be achieved from measurements on the resonance by reflection at both ports of the resonator if the VNA is calibrated; either by measuring the off-resonance $|S_{11}|$ and $|S_{22}|$ or, more precisely, by fitting Q-circles – see Section 4.3.

Once A_{21} has been measured, the calibrated diameter of the transmission Q-circle d_{21} can be calculated using equation (31). If the coupling factors of the two couplings can be taken to be equal, and the coupling loss is negligible, Q_o can then be determined by using the expression [4, 49]

$$Q_o = \frac{Q_L}{1 - d_{21}} \ . \tag{38}$$

Using weak couplings ($|S_{21}| \approx -40\,\text{dB}$ at resonance) is advantageous for measurement by transmission, as then $Q_o \approx Q_L$ and a small imbalance between the coupling factors has little effect (see Section 4.4).

A comprehensive analysis of the effect of loading by lossy non-equal couplings has been given by Leong and Mazierska [48] (summarised in a conference paper [50]). Simplified equations, based on reference [48], for the case of non-equal but lossless couplings are presented below.

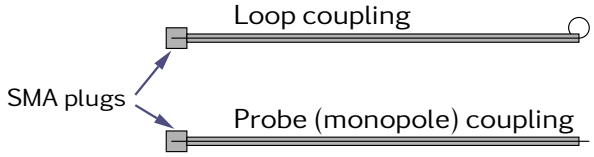

Figure 5: Loop and probe couplers (for H-field and E-field excitation of cavity resonances respectively) made from semi-rigid cable.

When there is dissipation in the external circuits connected to the two couplings, Q_o is given by

$$Q_o = Q_L\left(1+\beta_1+\beta_2\right) \tag{39}$$

where the coupling coefficients β_1 and β_2, are determined from the calibrated diameters of the port 1 (S_{11}) and port 2 (S_{22}) reflection Q-circles, d_1 and d_2. As it is assumed that the impedance of the couplings is negligible, *Method 1* described can be used: d_1 and d_2 are determined using equations (31) and (34) and the diameters of the port 1 and port 2 touching circles are $D_1 = D_2 = 2$ Units. The following equations then apply [48, 50]:

$$\beta_1 = \frac{d_1}{2-d_1-d_2} \tag{40}$$

and

$$\beta_2 = \frac{d_2}{2-d_1-d_2}. \tag{41}$$

Therefore, for couplings that have low impedance,

$$Q_o = \frac{2Q_L}{2-d_1-d_2}. \tag{42}$$

Reference [48] shows that the S_{21} Q-circle diameter is the geometric mean of that of the S_{11} and S_{22} Q-circles, i.e. $d_{21} = \sqrt{d_1 d_2}$. Therefore, if the coupling factors at each port are equal, $d_{21} = d_1 = d_2$. It follows that equation (42) can be simplified to give equation (38).

2.6 Application of NLQFIT

The predicted S-parameter response of a resonance (a circular arc in the complex plane) is obtained from equivalent circuit models of resonators such as that shown in Figure 1. While such models generally provide good descriptions, they are simplifications. Furthermore, mismatches, uncalibrated lines, and frequency dependency of coupling factors and leakage affect the measured response. It is therefore unsurprising that even when resonances are well-shaped, slight deviations from the expected circular form may be seen in measurements over a broad band. Q-factor is actually defined at resonance, so it is justifiable to select a narrow frequency span centred on the peak to reduce systematic error. Often the best strategy is to use a two-stage measurement and fitting process, using data acquisition software to control the VNA: First, a preliminary measurement (Figure 6a) is made with a wide frequency span to obtain approximate values of f_L and Q_L. Then, a more precise measurement (Figure 6b) is made with the sweep range reduced and centred on the resonance. In this report the optimum sweep range is taken to be $f_L \pm f_L/Q_L$, making the arc of the Q-circle 70.5 % of a full circle (for convenience referred to as a 70 % Q-circle). In the author's experiments, ANGWTS (Section 2.4) are applied to both fits. While it is usual to choose the swept range so that the resonant peak is at the centre, Q-factor can also be fitted when all of the data lies to one side of the peak. Restricting the frequency range makes it possible to reduce the effect of a nearby unwanted mode (see Section 4.5).

For a well-shaped resonant mode, such as the resonance of a *Split-Post Dielectric Resonator*[7] (SPDR) [51] shown in Figure 6, the Q-factors fitted by NLQFIT may have acceptable accuracy when the sweep span is many times broader than the width of the resonance. NLQFIT fits $Q_L = 7160$ and $Q_L = 7454$ respectively for the uncalibrated transmission data for broad and optimised spans shown in Figures 6a and 6b respectively. In this case, omitting the ANGWTS has a fairly small effect even for the broad span; $Q_L = 7271$ is obtained. The respective values fitted by the Fortran program QZERO[8] developed by Kajfez [18] are $Q_L = 5342$ and $Q_L = 7455$, so optimising the VNA sweep range is more critical if this program is used. Accurate fitted solutions when the data has a broad frequency span are needed when measurements can only be performed once, for example, for observations during chemical reactions [52].

The measurement shown in Figure 6b was repeated after the VNA had been calibrated (Table 2) leaving only short uncalibrated line sections, as shown in Figure 3. Measurements both with and without calibration are in very good agreement; providing evidence that for measurement by transmission, it is not necessary to calibrate the VNA for a weakly-coupled resonator with high Q-factor (see Section 3.1.1 for further discussion). The values of Q_L calculated by QZERO are also seen to be in very good agreement. The values of Q_o calculated with QZERO are not shown as they are for a reflection resonator.

Reference planes associated with the factory correction (Section 3.2) of an uncalibrated VNA are generally in the locality of the front-panel connectors. The total length of uncalibrated line (i.e. the cables) is approximately 1.5 metres. De-embedding this length of cable for the data shown in Figure 6b changes the fitted Q-factor by only 0.01 %. This is because the Q-factor is high and $|S_D| \ll d$ (see Section 3.3.1). In this experiment the leakage observed occurred predominantly in the locality of the resonator; an isolation measurement using matched loads on both VNA ports showed that the internal S_{21} leakage is an order of magnitude smaller.

Extra coefficients that represent the length of uncalibrated lines (Section 2.3) or a dependence of the leakage vector on frequency (Section 4.5) can be fitted if required. Implementations of NLQFIT referred to in this report are suffixed by the total number of fitted coefficients (Table 1).

2.6.1 Code examples

Appendix A provides source code for Matlab/Octave and Python implementations of NLQFIT. These can be downloaded from https://doi.org/10.47120/npl.MAT58. An alternative Python implementation was added to the scikit-rf open-source library in June 2022.

If the data is poor, NLQFIT may not be able to reach a satisfactory solution, or an exception (divide by zero etc.) may occur. For real applications, these code modifications to handle such events cleanly may be needed:

- Check that the fitted Q_L is not unreasonably small or negative. If the estimated f_L is not sufficiently accurate, or if the peak in the data is not a result of resonance, then a successful but meaningless fit can be obtained.
- Trap exceptions.

[7] Now manufactured by QWED Sp. Z o. o, Warsaw, http://www.qwed.eu
[8] QZERO is supplied on disk with reference [18] as a compiled DOS program.

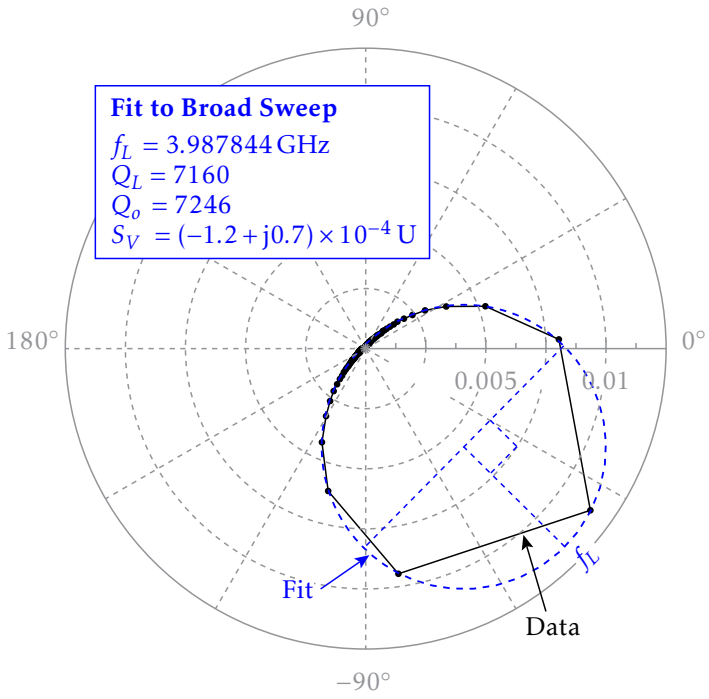

(a): First measurement

A preliminary result is obtained using a wide frequency span (50 MHz for data shown). The plotted S_{21} data points are connected by straight lines.

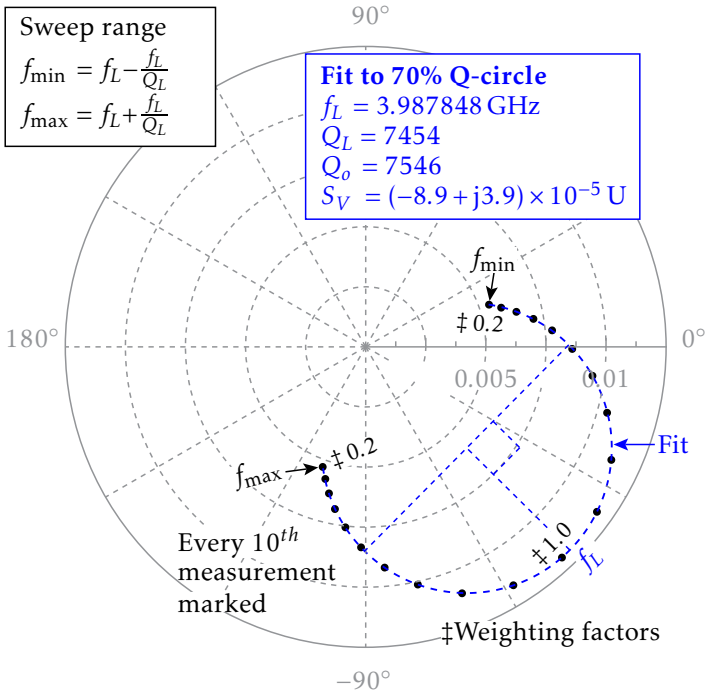

(b): Second (optimised) measurement

Prior to triggering this measurement, the VNA sweep is set to $f_L \pm f_L/Q_L$ (using the first measurement of f_L and Q_L). This makes the Q-circle an arc that spans 70.5 % of a full circle For convenience, this is referred to as a 70 % Q-circle in this report.

Figure 6: Q-factor determination from uncalibrated measurements of complex transmission coefficient (S_{21}) at 201 equally-spaced frequencies by fitting using NLQFIT6. The quasi-TE01δ mode of a split-post dielectric resonator [51] was measured. (a) shows a preliminary measurement with the VNA sweep set to a broad range. This was used to obtain provisional values of the resonant frequency and Q-factor, which were used to set the optimum sweep frequency range prior to the more precise second measurement, (b). ANGWTS were applied to both measurements. The data is shown scaled by A_{21} which was obtained from a measurement on a "thru" $A_{21} = 1/|S_{21}|^{(\text{thru})} = 1/0.874$. Corrections for the phase of cables (total length 1.5 metres) were not applied. Coupling factors at each port were adjusted so that they were approximately equal. Weak coupling was used; at resonance $|S_{21}| \approx -40$ dB.

Table 1: NLQFIT algorithms referred to in this report.

NLQFIT6	Finds least-squares minimum of equation (21). Six real-valued coefficients are fitted.
NLQFIT7	Finds least-squares minimum of equation (26). Seven real-valued coefficients are fitted, including one that characterises the length of uncalibrated line.
NLQFIT8	Finds least-squares minimum of equation (43). Eight real-valued coefficients are fitted. A model for frequency dependency of the leakage vector is used (see Section 4.5).

Table 2: Comparison of measurements of Q-factor with the VNA uncalibrated[9], and calibrated. The uncalibrated measurements are shown in Figure 6b. Q-factor was determined with the VNA frequency sweep set to the optimum range, $f_L \pm f_L/Q_L$ (3997.8 ± 0.5 MHz). These measurements were made by transmission with weak couplings. Values of Q_L were fitted to the same data sets using the program QZERO [18] are also shown. Q_o is calculated by using equations (31) and (38).

		NLQFIT6		**QZERO**
	$*A_{21}$	Q_o	Q_L	Q_L
Uncalibrated	†1.144	7546	7454	7455
GPC-7 Cal.	1.000	7537	7447	7447

*Attenuation in uncalibrated lines is neglected.
†Obtained from an S_{21} measurement on a "thru" connection: $A_{21} = |S_{21}|^{-1} = 1/0.874$.

3 Experimental Technique

In this section, experimental techniques for measurement of Q-factor by transmission and reflection methods are compared. Aspects that are considered include coupling requirements, the effects of uncalibrated lines, and whether the VNA needs to be calibrated.

3.1 On Coupling and Calibration Requirements

3.1.1 Transmission

An equivalent circuit of the transmission resonator shown in Figure 1 can be simplified by transforming input and output circuits to the middle loop [2] – see Figure 7. This provides some useful insights. *Weak coupling* is seen to step the VNA 50 Ω line impedance down to a low value as the turns ratios g_1 and g_2 of Figure 1 are both small ($\ll 1$). The loading by the

[9] In uncalibrated mode all of the models of VNA used in this report apply internal corrections (so that measured S-parameters have approximately the correct magnitude). VNA calibration is discussed in Section 3.2.

VNA test ports is therefore minimal. Furthermore, measurement by transmission with loop couplings is seen to be a particularly favourable technique, as the three component RLC model (not accounting for leakage) is sufficient to describe the resonance in the presence of coupling loss and inductance, so an undistorted Lorentzian response should be obtained. Inductive loading from coupling loops will nevertheless cause *frequency pulling* [2].

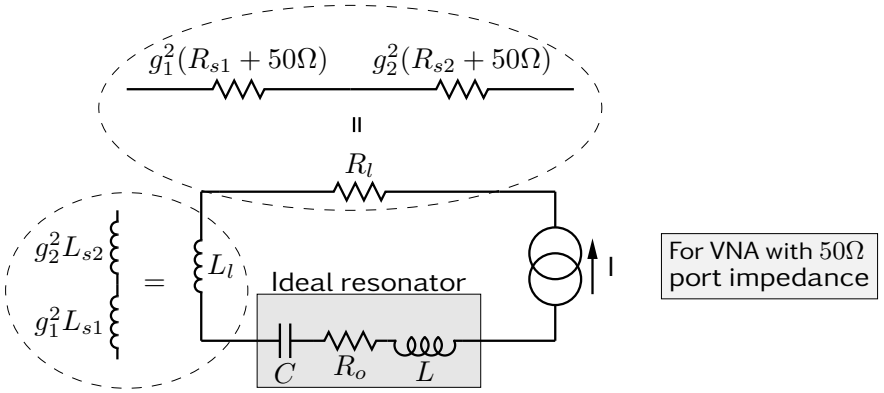

Figure 7: Equivalent circuit for transmission measurement of Q-factor (Figure 1 with input and output circuits transformed to the middle loop, where g represents the turns ratio). Coupling series impedances R_{s1} etc. are defined in Figure 1. Two components, R_l & L_l, are sufficient to represent the circuit that loads the resonator.

Weak coupling lessens the effect of any inaccuracy in the fitted Q-circle diameter d (and therefore in A) on the calculated Q_o – see equation (38), but if the couplings are too weak the signal to noise ratio is lower and variations between repeated measurements are increased. Typically, couplings are set so that a measurement of transmission between the two ports of the resonator shows 40 dB attenuation at resonance (corresponding to d_{21} = 0.01 Units). For resonant cavities, couplings must therefore be physically small or located in a low-field region, so they have minimal perturbing effect – an inherent advantage of the transmission method. Small couplings have lower dissipative loss, and also produce less radiative loss for open resonant structures, such as Hakki-Coleman dielectric resonators [53].

Table 2 compares calibrated and uncalibrated measurements and demonstrates that calibration brings no advantage for measurements on a high Q-factor resonator with weak couplings (this point is also made by Inoue et al [27]). This favourable situation arises because there is little loading by the VNA test ports, and because (in general) small mismatches only have a second-order effect on transmission coefficient. Using VNAs uncalibrated for transmission measurements does not impair the shape of Q-circles (see Figure 6). As there is no requirement for calibration, inexpensive VNA test-port cables can be used. Measurements made with different uncalibrated VNAs are found to very consistent (see Section 4.1). As with all Q-factor measurements, best measurement accuracy is usually obtained when Q-factor is high, as the coupling factors, mismatches and leakage will be practically constant in a narrow bandwidth. Q-factors fitted to complex data can be affected by uncalibrated lines, although such effects are small for typical microwave measurements by transmission (Section 3.3.1).

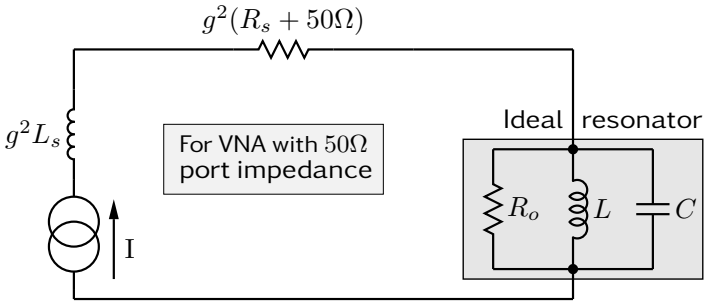

Figure 8: Equivalent circuit for reflection measurement of Q-factor using a loop coupling. Loss and self-inductance associated with the coupling are represented by R_s and L_s. A transformer representation of the coupling is used, where g represents the turns ratio.

3.1.2 Reflection

To obtain reliable measurements in reflection, *strong coupling* is normally used (i.e. with a large loop, probe or iris), otherwise the change in reflection coefficient at the resonance is very small compared to the detuned reflection coefficient S_D [54] of equation (1). Measurements may be made *overcoupled* ($d > 1$ Unit), *critically coupled* ($d = 1$ Unit), or *undercoupled* ($d < 1$ Unit). Critical coupling implies a match to 50 Ω at resonance. Undercoupling with $0.1 < d < 1.0$ Units generally gives the best measurement accuracy. The equivalent circuit of a loop-coupled cavity, Figure 8, has five components and gives an asymmetric non-Lorentzian response. When the coupling series inductance L_s is negligible, Figure 8 simplifies to the three-component RLC circuit on which equation (1) is based. If $L_s > 0$, a good fit to the RLC model over a narrow band of frequencies near the resonance may be obtainable; although the fitted f_L and Q_L are changed as a result of the inductive loading. If S is plotted on a polar chart for wide sweeps when $L_s > 0$, the Q-circle is observed to become ovoid and cross over itself [21, 48]. This is utilised in the *critical points method* for measuring Q-factor [55, 56], which requires the two values of frequency that occur at the cross-over point to be measured. It is important to be aware that the Q-circle can also become ovoid and cross over itself if the calibration reference plane is offset from the coupling (i.e. there is an uncalibrated line) – see Figures 9c and 13. In either case, $|S| < 1$ Unit at the cross-over point. If the sweep span is small so that only part of the Q-circle is visible, it may not be clear whether (i) the Q-circle crosses-over itself, or (ii) the measured Q-circle is inset from the edge of the polar chart because of attenuation in the uncalibrated line [21]. S_V is a fitted complex quantity defined by equation (8) that depends on the coupling impedance and the length of uncalibrated line.

Multi-path interference effects occur in an uncalibrated system, or if there are mismatches in the uncalibrated line. For measurements by reflection, calibrated VNA measurements are recommended where possible, as measurement uncertainties can be significantly reduced. It is also important to ensure that mismatches in the uncalibrated line are kept to a minimum. In Section 3.3.2 the effects of matched and mismatched uncalibrated lines are demonstrated by using simulations.

3.2 An overview of VNA calibration procedures

The VNA receiver systems allow *uncorrected* S-parameter ratios to be obtained at each frequency. The measurements that the VNA presents to the user may have been processed according to *factory* data stored inside the instrument; uncorrected S-parameter ratios may, for example, have been multiplied by a scaling factor so that they have approximately the correct magnitude. Some types of instrument also apply corrections for non-linearity. The components of a VNA system (couplers, mixers, tuned amplifiers, cables etc.) are not themselves calibrated, so if precise measurements are needed the user must follow a *calibration* procedure [57]. This determines a set of complex calibration coefficients that characterises the mismatches within a VNA system, and defines *calibration reference planes* to which measurements of phase are referenced. Manufacturers refer to this as the *system error correction*. Corrected S-parameters can then be calculated from uncorrected ratios measured by the VNA.

VNAs can be calibrated by measuring artefacts from a *calibration kit* [57]. Calibration kits typically contain calculable impedance standards that are based on open or short-circuited precision coaxial lines that have known dimensions. In some cases, they also contain precision two-port artefacts such as coaxial lines. *Two-port* (transmission & reflection) calibration enables calibrated measurements on all four S-parameters. If only reflection measurements are required, a simpler *one-port* calibration can be performed. The calibration process can be automated by using *electronic calibrators* [58] that contain switchable calibration artefacts. The preferred form of calibration is known as a *full mismatch correction*, but simplified (and less precise) approaches to calibration that use fewer calibration coefficients can be used. VNAs have built-in calibration software, and usually incorporate an *interpolation* algorithm that allows calibrations to still be applied if the swept frequency range is reduced. This flexibility is particularly useful for measurements of Q-factor by reflection, as calibrated S-parameter measurements are needed for the best precision.

After manufacture, VNAs are subject to a *factory calibration*[10]. Some manufacturers use impedance standards to obtain an approximate broadband calibration that is referred to as a *factory correction*. This is applied as a default if no other calibration is available. If precise measurements are required, an instrument that only has a factory correction must be considered to be *uncalibrated*. In this report the term calibrated is only used when the system (VNA and test-port return cables[11]) has been calibrated immediately before use with impedance standards. Reference planes for measurements of phase with VNAs that are uncalibrated (or only have a factory calibration) are normally located approximately at the front-panel connectors.

3.2.1 Establishing measurement linearity

Traceable tests of the linearity of VNA receivers

Traceability requires the *linearity* of the VNA receivers to be demonstrated over an amplitude range from 0 dB to the lowest measured (a *dynamic range* of 50 dB is typically required for measurement of Q-factor by transmission). Each uncorrected S-parameter measurement is a ratio of two signals (transmitted or reflected signal, and a sample of the source signal)

[10] Calibration and trimming of all of the subsystems of the instrument by the manufacturer. The calibration data created is stored within the instrument.

[11] High quality flexible cables that have been engineered to produce minimal changes in phase and mismatch on bending. Calibrated measurements require such cables to be used. They are available from a number of manufacturers.

measured by superheterodyne receivers (mixers, tuned amplifiers & analogue to digital converters) [11]. The mixer in either receiver could be subject to *compression* at high power levels. The source power setting is adjustable allowing the user to choose an appropriate compromise between linearity, measurement speed and noise if the manufacturer's default setting is not satisfactory. For measurements by transmission, the dynamic range is limited by leakage in the coaxial couplers used in the test-set and noise. Subtler effects, for example limitations in the performance of low pass filters that are placed after the mixers for image rejection, can also reduce the dynamic range. The linearity performance of VNAs is likely to vary with frequency; for instruments that are designed for operation over a frequency range that spans several decades (e.g. 100 kHz to 10 GHz) it tends to degrade at the lowest frequencies.

Linearity can be checked in transmission by using a technique that uses a *gauge block* (an attenuator that can be switched in/out by a repeatable mechanism) and a calibrated adjustable *rotary vane attenuator* [59]. Alternatively, the VNA can be checked against a *stepped attenuator*. Typically, steps 0→10 dB, 0→20 dB etc. (up to 0→80 dB) are measured and compared to the calibration data for the attenuator at the measured frequency. The VNA should be used calibrated (with a two-port full mismatch correction) for both of these methods.

Measurements on the Q-factor as a function of power level at the VNA port can also be used as a practical demonstration of linearity. The power level is set by the VNA source power and stepped attenuator (if provided) controls, and is traceable to the factory calibration of the instrument against reference standards owned by the manufacturer. An outcome of experiments on an Agilent 8753ES VNA (Section 4.6) is that, for measurement by transmission, the power level at which compression becomes apparent is increased when the resonator has high insertion loss. For a weakly-coupled resonator, it may therefore be possible to improve repeatability by setting the power-level above the manufacturer's default, yet still remain in the linear region. This does not apply to the reflection method (Section 4.6); compression effects were observed at the highest source-power settings.

The "3 dB points" method at constant power by attenuator series substitution

Peak and 3 dB points can be measured at the same power level if a calibrated 3 dB attenuator can be switched in and out with a repeatable switch [4]. Therefore, Q-factor can be measured traceably without requiring a linear detection system. The technique does not account for leakage signals that bypass the resonator, so traceable measurement also requires that these are at a negligible level. A switched attenuator is typically calibrated in a 50 Ω system, so the resonator coupling (which is very close to being an open circuit) requires a parallel load of 50 Ω. Pads (fixed attenuators matched to the 50 Ω system impedance) are normally placed either side of the switched attenuator. These reduce uncertainty associated with mismatches. Resonance-width methods can also be used to determine Q-factor when the attenuation step has an arbitrary (but known) value [60]. The confidence in measurements can therefore be improved by repeating them with another calibrated attenuator (e.g. 6 dB).

3.3 On the effects of uncalibrated lines

Frequency-independent phase delay (ϕ) in uncalibrated lines causes rotational transformation of the Q-circle around the origin of the Polar/Smith chart, but has no effect on the values of f_L, Q_L and d obtained from the six coefficients fitted by NLQFIT6 (equation (22)). Frequency dependent phase delay ($\Delta\phi$), however, causes the shape of Q-circles to be modified as points at the highest frequency are rotated farther (Section 1.2.2). This effect increases in proportion

to the frequency and to the length of uncalibrated line ($\bar{l}$), and can be especially significant at millimetre-wave frequencies [26] and higher. If Q-factor is obtained by fitting in the complex plane it may be necessary to account for uncalibrated lines by (i) by removing them numerically (de-embedding), or (ii) by including $\bar{l}$ as a fitted quantity. De-embedding a coaxial line requires its *electrical length* $\bar{l}\sqrt{\epsilon_r}$ to be obtained (where ϵ_r is the effective permittivity of its dielectric).

Simulations presented in Section 3.3.1 show that, for transmission measurement of Q-factor, uncalibrated lines with typical length ($\Delta\phi_w < 1°$) have little effect on results in a low leakage system. Therefore, it is sufficient to de-embed uncalibrated lines using an approximate length and then fit Q-factor using NLQFIT6. Indeed, this is often the best approach. NLQFIT7, which has a fitted parameter to account for uncalibrated lines (Section 2.3), proves to be less "robust" and for typical transmission data ($|S_D| \ll d$) may not converge to a solution.

The fitted Q-factor is quite sensitive to the length of uncalibrated lines for measurement by reflection (see Section 3.3.2) – a consequence of the location of the pole of the resonance near the edge of the polar chart. To ensure that measurements are accurate, uncalibrated lines must be considered. The best approach is usually to fit the total length of uncalibrated line by using NLQFIT7, therefore avoiding the need to de-embed it. This technique can be applied when the length of uncalibrated line is not directly measurable, e.g. for an uncalibrated VNA for which the reference plane is not defined. The fitted length can be influenced by the size and nature of the coupling as: (i) the phase centre of couplings is offset from the cable end, (ii) Q-circles become asymmetric if loop couplings have significant inductance – see Section 4.2.

For a coaxial line that has solid PTFE dielectric (most semi-rigid cables), the refractive index $\sqrt{\epsilon_r}$ = 1.43 at room temperature. Flexible cables typically use an air/PTFE dielectric (microporous or "tape-wrap") which has a lower effective refractive index. For typical VNA test-port return cables $\sqrt{\epsilon_r} \approx 1.2$ according to manufacturers' data.

3.3.1 Simulations of the effect on transmission measurements

The Q-circles seen on the VNA display (described by equation (7)) are not perfectly circular if uncalibrated lines are present. For long cables and low leakage ($|S_D|/d \ll 1$), a broad frequency span gives a cardioid-shaped response that is almost symmetric, as shown in Figure 9b. If the leakage is significant, as shown in Figure 9a, the Q-circle becomes distorted even for comparatively short cables. The broad spans shown in Figure 9 were chosen to allow the effects of cables to be demonstrated. Measurements of Q-factor would normally be made using comparatively narrow spans to achieve the best accuracy (see Figure 6b).

Maximum errors in Q_L caused by uncalibrated lines as a function of $\Delta\phi_w$ were estimated by simulation with the aid of computer software. Q-factors were determined by fitting to simulated phase-delayed data with NLQFIT6. A linear frequency sweep was assumed so the data was weighted in proportion to the rate of angular progression around the Q-circle (ANGWTS) by using equation (28). The frequency span was chosen to be the recommended optimum $f_L \pm f_L/Q_L$, as shown in Figure 6b. Figure 10 shows the results of the simulation. The presence of uncalibrated line causes an increase in the apparent value of Q_L. For typical transmission measurements of Q-factor at microwave frequencies, the increase is only significant if the magnitude of the leakage vector is an appreciable fraction of the Q-circle diameter and long uncalibrated lines are used. If the frequency span is set wider, the fitted Q_L can instead be decreased – see Figure 9a.

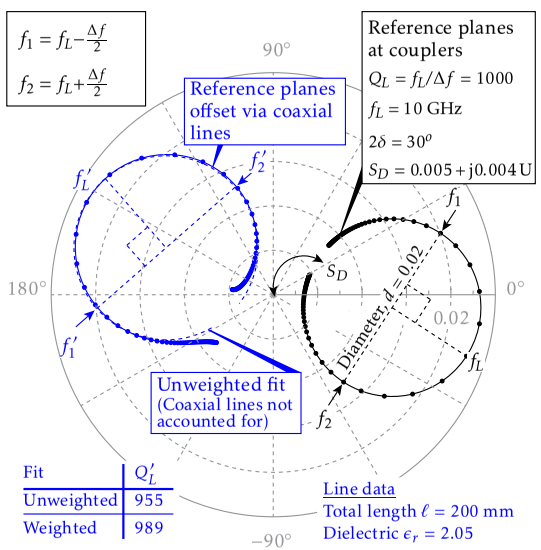

(a): Transmission with leakage signal, $|S_D| > 0$.
The left (blue) Q-circle shows an asymmetric response obtained with uncalibrated coaxial line sections, total length 200 mm, $\Delta\phi_w = 1.7°$.

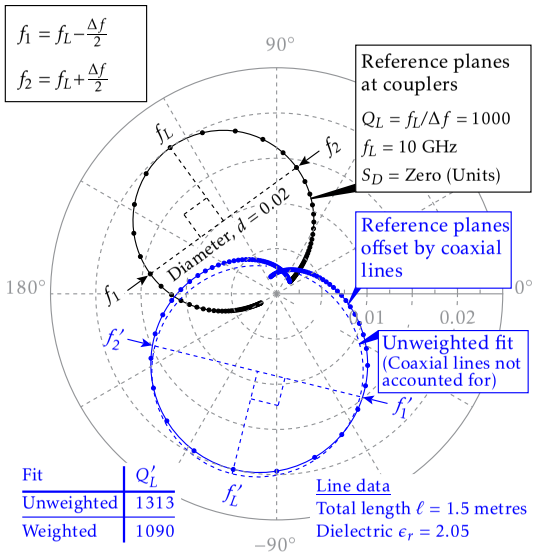

(b): Transmission with no leakage signal.
The lower (blue) Q-circle shows the cardioid response obtained with uncalibrated coaxial line sections, total length 1.5 metres, $\Delta\phi_w = 12.9°$.

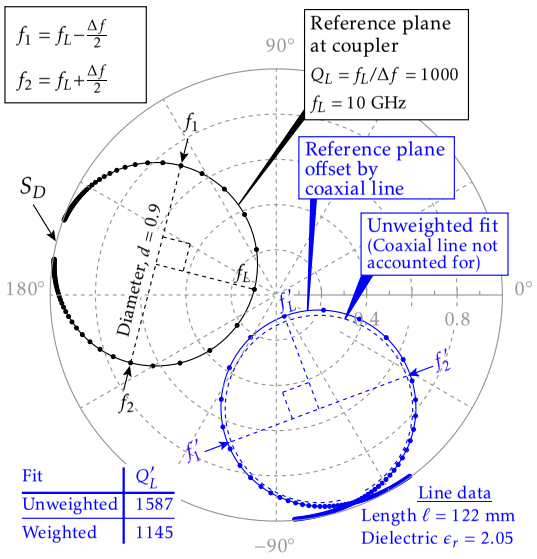

(c): Reflection.
The lower Q-circle (blue) shows the effect of an uncalibrated coaxial line section, length 122 mm, $\Delta\phi_w = 2.1°$. Calculated for lossless coupling.

Figure 9: Calculated Q-circles of transmission and reflection resonators for $Q_L = 1000$. The marked points are simulated S-parameters, S_m, calculated by using equation (7) for a calibrated VNA ($A = 1$). If there are no uncalibrated lines, i.e. calibration plane(s) are at the coupler(s), the Q-circles shown in black are obtained. Solid blue lines show the predicted non-circular responses when there are non-attenuating uncalibrated line sections that are matched to the VNA (50 Ω impedance).

Q-factors were fitted (with and without weightings) to the simulated data by using NLQFIT6 without the uncalibrated lines being accounted for. Dashed blue Q-circles are the unweighted fits (weighted fits are not shown for clarity). Apostrophised symbols f_1' , Q_L' etc. refer to fitted quantities. The quantity $\Delta\phi_w$ is defined by equation (9). The purpose of these plots is to show that neglecting uncalibrated line sections can cause error if Q-factor is determined by fitting in the complex plane. The data shown is calculated for a broad frequency span to make the effect of uncalibrated lines clearer. In actual measurements, a smaller span would normally be used (see Section 2.6).

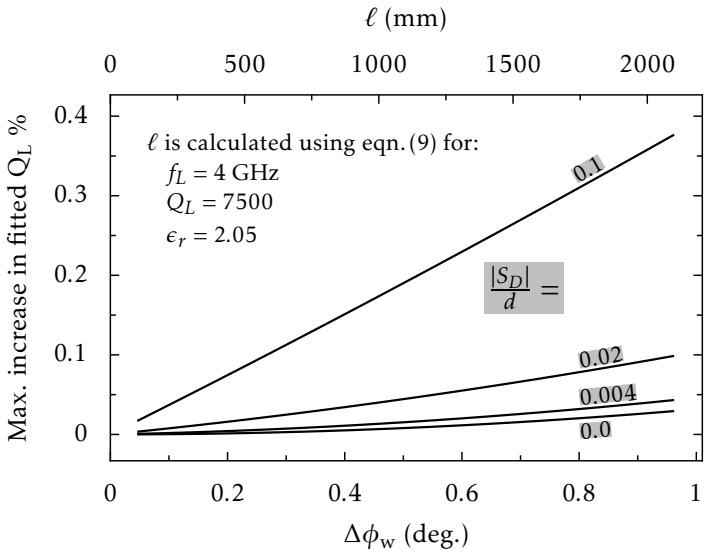

Figure 10: Predicted maximum errors in fitted Q-factor caused by uncalibrated lines as a function of $\Delta\phi_w$ and $|S_D|/d$ for a transmission resonator. The data were obtained by fitting to simulated complex data with sweep range $f_L \pm f_L/Q_L$ (70% Q-circle) with NLQFIT6. ANGWTS were applied. Arg(S_D) could in practice have any value, so was varied through 360° to find the maximum error. The predicted errors are a function of $\Delta\phi_w$ and the ratio $|S_D|/d$ only. The top axis gives the equivalent total length of uncalibrated lines ℓ calculated for the measurement given in Figure 6b assuming that the lines are coaxial and have solid PTFE dielectric.

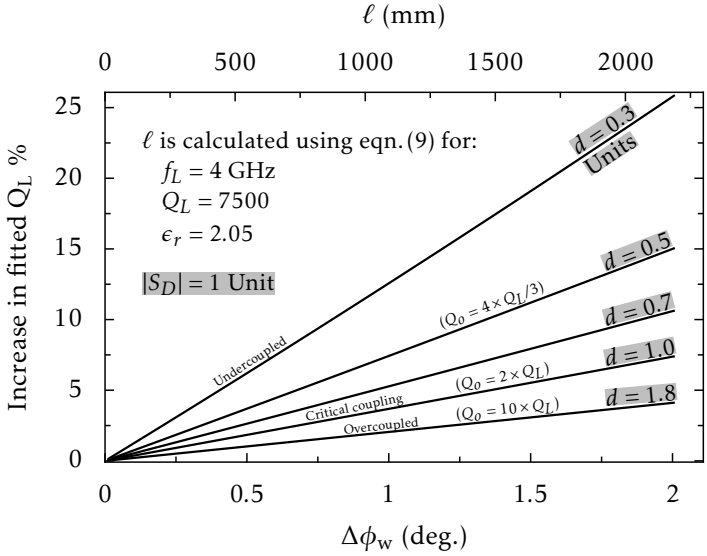

Figure 11: Predicted errors in fitted Q-factor caused by uncalibrated lines as a function of $\Delta\phi_w$ and d for a reflection resonator with lossless coupling. The data were obtained by fitting to simulated complex data with sweep range $f_L \pm f_L/Q_L$ (70% Q-circle) with NLQFIT6. ANGWTS were applied. The predicted errors are a function of $\Delta\phi_w$ and d only. The top axis gives the equivalent total length of uncalibrated line ℓ calculated for the values of f_L, Q_L, and ϵ_r given in Figures 6b and 10 to allow direct comparison.

The length equivalent of $\Delta\phi_w$ calculated with equation (28) is plotted on the top axis of Figure 10 for a resonator that has loaded Q-factor Q_L 7500 and resonant frequency 4 GHz (data similar to the measurement shown in Figure 9b). Coaxial uncalibrated lines with solid PTFE dielectric (shown in Figure 17) were assumed. For the worst-case leakage shown on the graph, $|S_D|/d = 0.1$, then if ℓ = 600 mm the error in measured Q_L is likely to be less than 0.1 %.

3.3.2 Simulations of the effect on reflection measurements

Matched uncalibrated line. Figure 9c shows how the Q-circle measured in reflection becomes ovoid when there is a matched uncalibrated line, in this case causing it to cross over itself. The inductance of a loop coupling (Section 3.1.2) also causes the Q-circle to cross over itself. Neither effect may be apparent unless measurements are made over a broad frequency span.

The simulations described in Section 3.3.1 were repeated for measurements of Q_L by reflection. The process was the same: simulated phase-delayed data was fitted by NLQFIT6 with the frequency span set to $f_L \pm f_L/Q_L$ and ANGWTS applied. Errors in Q_L caused by an uncalibrated line as a function of $\Delta\phi_w$ are plotted in Figure 11. Uncalibrated lines are observed to have an increased effect when the resonator is undercoupled (i.e. $d < 1$ Unit). The simulation does not account for distortion of Q-circles associated with strong coupling, e.g. the effect of the inductance of a loop coupling.

The length equivalent of $\Delta\phi_w$ plotted on the top axis of Figure 11 is calculated by using equation (9) for a resonator that has loaded Q-factor Q_L 7500 and resonant frequency 4 GHz. If this resonator is used with critical coupling, the length of uncalibrated line (with solid PTFE dielectric) must not exceed 30 mm to ensure that the error in $Q_L < 0.1$ %. This is much less than for the transmission measurement on a similar resonator discussed in Section 3.3.1.

Mismatched uncalibrated line. The effect of mismatches was simulated for the mismatched uncalibrated line shown in Figure 12. Fits were made by using NLQFIT7, so a matched uncalibrated line has no effect on the simulated measurements of Q_L and Q_o. The mismatched line is formed from a non-attenuating semi-rigid cable that incorporates an air space. The Q-circles (Figure 13) appear ovoid and have a crossing point as a result of the frequency-dependent phase delay given by equation (5). Q_o is obtained by using *Method 1*. Q_L is expected to depend on the mismatch as this changes the loading by the external circuit, but variations in Q_o are a result of error caused by interference effects. Data for the matched case $L_a = 0$ is plotted in black. A rather extreme situation with large air space, high resonant frequency and low Q-factor is simulated to make an important point: the shape of Q-circles cannot be used as an indicator of whether or not there are mismatches. Further simulations show that the effect of mismatches on Q_o is reduced (Table 3) when they are a fraction of a wavelength from the resonator (as is the case at 1 GHz) and when the Q-factor is high.

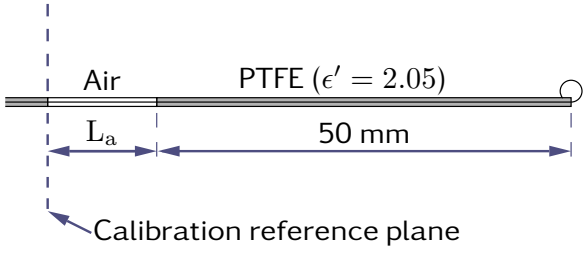

Figure 12: Mismatched uncalibrated line and loop coupling for reflection resonator.

Table 3: Simulations of the effect of a mismatched uncalibrated line (Figure 12) on Q-factor fitted by using NLQFIT7 for measurement by reflection. The frequency span was set to $f_L \pm f_L/Q_L$ and ANGWTS were applied.

L_a	0 mm	2 mm	4 mm	6 mm	8 mm
†Data for the resonator	**Q_o calculated from fitted coefficients by using *Method 1***				
f_L=10 GHz Q_L=100	167	164	167	170	171
f_L=1 GHz Q_L=100	166.67	166.67	166.67	166.68	166.68
f_L=10 GHz Q_L=1000	1667	1664	1667	1670	1671

†The Q-circle diameter was specified as $d = 0.8$ in a matched 50Ω system in all cases.

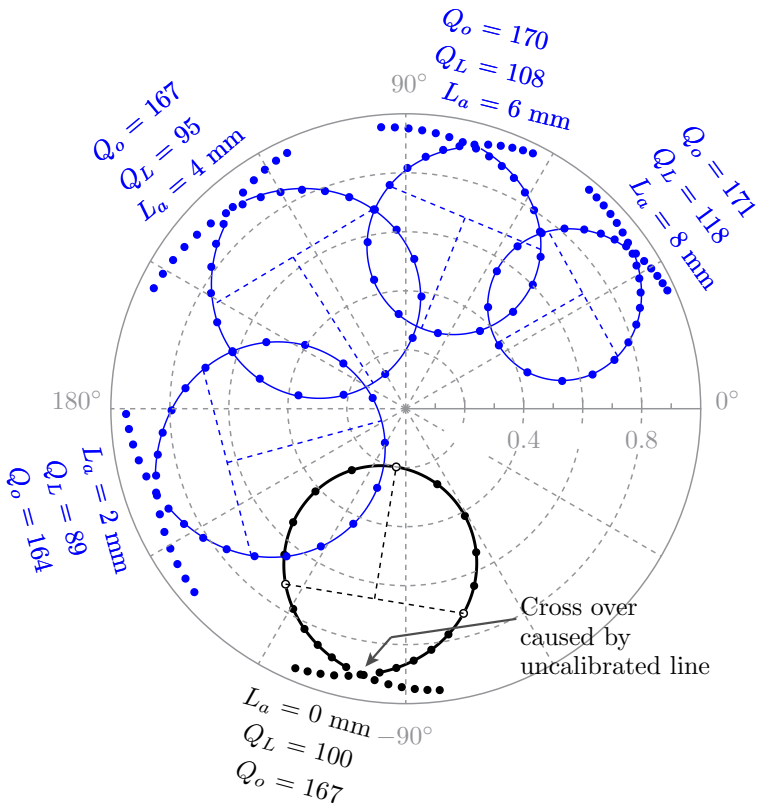

Figure 13: Simulated Q-circles (blue) for a reflection resonator as a function of the length L_a of a mismatched section of the uncalibrated line, as shown in Figure 12. The black Q-circle is obtained when the uncalibrated line is matched ($L_a = 0$). The values of Q_L shown, and the traces marked with solid lines, were obtained by fitting to data points in the frequency range to $f_L \pm f_L/Q_L$ by using NLQFIT7. ANGWTS were applied. The values of Q_o shown were calculated from the fitted coefficients by using *Method 1*. Data for the resonator in a matched 50Ω system: Q-circle diameter $d = 0.8$, $f_L = 10$ GHz, $Q_L = 100$.

3.4 WHICH MEASUREMENT TECHNIQUE TO CHOOSE?

Table 4 presents a comparison of methods for measuring Q-factor by fitting to (either|or) *uncalibrated*|*calibrated*, *vector*|*scalar* and *transmission*|*reflection* S-parameter data in every permutation. The table is devised on the assumption that uncalibrated lines are present as shown in Figure 3. Numbered points are used to represent the many details that must be considered in a compact form. Scalar methods are not described in detail in this report, but more information can be found in references [2, 3, 17, 31, 32, 34, 61].

The most important decision, whether or not to use a transmission or a reflection method, merits some further discussion. By most criteria the transmission method with weak couplings is the best method to choose; it is generally easier to use as it is not usually necessary to calibrate the VNA (although Q_o can be obtained with lower uncertainty if the transmission of a "thru" is measured). Moreover, phase delay caused by uncalibrated lines has a smaller effect on Q_o for typical vector measurements by transmission ($|S_D| \ll d$) than by reflection. Another aspect that should be considered is the effect of mismatches in uncalibrated lines. For transmission measurements, mismatches are not usually a cause of significant uncertainty as they have only a limited second order effect on measurements of S_{21}. For measurements by reflection, however, significant uncertainty may result, especially if d <0.1, because mismatches have a first order effect on measurements of S_{11}. Low-cost SMA connectors that are commonly used for making couplings (Figure 5) typically have a mismatch of $\gtrsim 0.01$ in magnitude at microwave frequencies. In many applications, the greatest advantage of the transmission method is that weak couplings that are physically small can be used. This brings a number of benefits:

- $Q_o - Q_L$ is comparatively low-valued, which helps to improve the accuracy of determinations of Q_o.
- *Frequency pulling* caused by inductive loading by the coupling itself is reduced.
- *Frequency pulling* caused by the reactive component of the load presented by the external circuit (VNA & cables) is reduced.
- Numerical models for cavities that use simple geometric forms (cylinder, rectangular box etc.) have improved accuracy when couplings are small. The perturbing effect of couplings is demonstrated by reference [62], which presents measurements of f_L of a coaxial resonator as a function of the length of a probe coupling.

The transmission method has a further advantage if loop coupling is used: the series impedance of the coupling can be described by increases to the 'R' and 'L' in the equivalent circuit (Figure 7) rather than additional components. This is significant as NLQFIT is based on the three-component equivalent circuit. Coupling using series capacitors – or monopole probes (Figure 5) for a cavity resonator – is not represented exactly by Figure 7, but precise measurements are still possible if weak coupling is used.

A reflection method with strong coupling ($0.1 < d < 1.0$) can be advantageous if small changes in Q-factor are to be measured, as the variation between repeated measurements is usually smaller than for the transmission method at the same VNA power level. However, to avoid compression effects the power level may have to be set lower – see Section 4.6 for more discussion.

Table 4: Comparisons of methods of Q-factor measurement by fitting to S-parameters under different calibration conditions.

Technique				**Calibration conditions**		
Method of fitting	**Fitted S-parameter**	**Coupling factor(s)**	**Ideal Q-circle diameter d (in Units)**	**VNA calibrated (with lossless* uncalibrated lines)**	**VNA calibrated (with attenuating uncalibrated lines‡)**	**VNA uncalibrated (or factory correction only)**
Vector	Transmission	Weak	$d \approx 0.01$	✓1,2,3	✓2,3,4	✓2,3,5
	Reflection	Strong	$0.1 < d < 1.0$	✓1,6,7	(✓) 6,9	✗6,8,9
Scalar	Transmission	Weak	$d \approx 0.01$	✓1,3,10	✓3,4,10	✓3,5,10
	Reflection	Strong	$0.1 < d < 1.0$	✓1,7,11	(✓) 9,11	✗8,9,11

Key (see opposite for explanation of numbered points):

* The column applies when uncalibrated lines (as shown in Figure 3) are matched to the VNA test ports (50 Ω) and are short enough to allow their attenuation to be assumed to be negligible.

‡ The column applies to a typical measurement situation in which there are uncalibrated lines that are matched only approximately to 50 Ω (so there are small mismatches). It is assumed that the attenuation of the uncalibrated lines is quite low ($\lesssim$3 dB in total), but unmeasured.

✓ Suitable for traceable measurement of Q_o with low uncertainty (typically ≈1% at coverage factor k=2) for resonances that are well-shaped and have high Q-factor.

(✓) Spurious signals reflected from mismatches in the uncalibrated line will impair the accuracy of measurements by reflection, so it is important to use cables and connectors that are as well-matched as possible.

✗ If there are uncorrected mismatches, measurements by reflection are not traceable and, in general, have increased uncertainty. Results are more likely to be satisfactory when the wavelength is appreciably longer than the uncalibrated lines (frequency <100 MHz for typical experiments). For vector measurements, the uncalibrated line has arbitrary length as the reference plane is not defined, so it must be accounted for by fitting – see Point 6.

Key to numbered points in Table 4

1. The scaling factor A is 1.0 for a calibrated measurement with non-attenuating and matched uncalibrated line sections.
2. For measurement of Q-factor by transmission it is usually sufficient to "remove" uncalibrated lines by de-embedding them from measured S-parameters using the line effective permittivity ϵ_r and length ℓ. Figure 10 can be used to estimate the largest acceptable value of $\Delta\phi_w$, so the precision to which ℓ must be determined can be found by using equation (9).
3. For a transmission-only method, the coupling losses are not determined. For weak coupling, it can normally be assumed that the effect that these have on the measured Q_o is negligible. Coupling losses can be accounted for if all four S-parameters are measured [48, 50].
4. The attenuation of uncalibrated lines may be too low to change the Q_o result significantly for weak coupling, in which case the scaling factor A = 1.0. If necessary, A can be increased to account for attenuation of uncalibrated lines by using additional measurement data (see Sections 2.5.2 and 4.3).
5. The scaling factor A can be taken to be $1/|S_{21}|$ of a "thru" connection measured at or near f_L (it can normally be assumed to be independent of frequency within the swept range). The attenuation of uncalibrated lines may be too low to change the Q_o result significantly for weak coupling but, if necessary, it can be counteracted by using a line of the same type and length as the "thru", or by increasing A on the basis of additional measurement data (Sections 2.5.2 and 4.3).
6. Q-factor fitted to vector reflection-coefficient data is subject to error if the phase delay $\Delta\phi$ caused by uncalibrated lines is not considered (see Figure 11). Usually, the best approach is to make the length ($\bar{l}$) one of the fitted quantities (NLQFIT7 algorithm). An approximate value for $\bar{l}$ can be de-embedded from the S-parameter data beforehand to make the fitting process more reliable.
7. Section 2.5.1 gives two possible methods of determining Q_o (*Method 1* and *Method 2*) for measurement by reflection when the VNA is calibrated. *Method 2* can give better accuracy when large loops are used, provided that the uncalibrated-line section is matched and has negligible attenuation.
8. The results given in Table 6 show that, for uncalibrated measurements by reflection, using a wide frequency span can increase measurement error substantially. It is therefore especially important to optimise the span and apply weighting factors as described in Section 2.6.
9. Q_o can be estimated by using *Method 1* described in Section 2.5.1.
10. Fitting a Lorentzian to scalar transmission data may not be sufficiently precise on account of leakage and the noise floor (Section 1), especially if very weak coupling is used. Modified fitting procedures can be used to improve precision [17, 24, 31, 33].
11. Calculation of Q_o from scalar reflection-coefficient data [1–3, 34] requires it to be known whether the resonator is overcoupled ($d > 1$ Unit) or undercoupled ($d < 1$ Unit). In manual experiments, this can be ascertained from the polar display of a VNA, or if using a scalar instrument, by observing the effect of increasing or decreasing the coupling by mechanical adjustment. It is important to note that the "3 dB point" method cannot be used for measurement of Q-factor by reflection. A convenient method for manual measurement with a scalar VNA is given by Kwok and Liang [61].

4 Measurement Examples

Various aspects of Q-factor measurement were studied in the following experiments:

Section 4.1: The repeatability of measurements made on an SPDR by transmission under the same conditions as those presented in Section 2.6.

Section 4.2: Measurements by reflection on a rectangular cavity which has $Q_o \approx 700$.

Section 4.3: A comparison of transmission and reflection methods for an SPDR that has $Q_o \approx 7500$.

Section 4.4: A study of the effect of an imbalance in coupling factors on measurements of Q_o by transmission for a weakly-coupled resonator.

Section 4.5: Measurements by using NLQFIT on resonances that overlap or are poorly shaped.

Section 4.6: Investigation of the effect of changing the VNA power-level setting on measurements of Q-factor by both transmission and reflection.

Section 4.7: Measurement on a superconducting absorption resonator that is measured by transmission. Q-factors fitted by NLQFIT and circle-fitting algorithms are compared.

4.1 Repeatability measurements by transmission with weak coupling

Perturbation methods of measuring the dielectric permittivity and loss of materials [63–65] require small changes in f_L and Q_o to be measured with high precision. Sets of measurements of these quantities fitted by NLQFIT6 are plotted as histograms (Figure 14) to allow measurement repeatability to be studied. The data shown was obtained for an SPDR measured by transmission using an uncalibrated Agilent 8753ES VNA. The couplings were adjusted so that $|S_{21}| \approx -40\,\mathrm{dB}$ at resonance. IF Bandwidth (IFBW) settings of 3 kHz (the default value) and 100 Hz were used. Reducing the IFBW improves signal to noise ratio, but also increases the time required to acquire the data. The resonant f_L and Q_o suffered from thermal drift, particularly at IFBW 100 Hz as the time required for the set of measurements was comparatively long (20 minutes). As the drift rate was fairly constant it was possible to apply simple corrections to reduce broadening of the histograms. For the f_L data it is likely that the correction will not eliminate broadening effects entirely as the drift rate was comparatively high (400 Hz/min.) and not precisely constant. Nevertheless, the histograms show that the repeatability of measurements of f_L is approximately one part in 10^7. The repeatability (1-sigma) of the Q-factor measurements is approximately $\pm 0.05\,\%$ at IFBW 100 Hz, and $\pm 0.2\,\%$ at IFBW 3 kHz. Measurement of small changes in Q-factor will usually require a low value of IFBW to be selected, or some averaging to be applied.

The variability of measurements of Q-factor made with different VNAs was also investigated – see Table 5. To reduce thermal drift, the SPDR was wrapped in bubble-wrap, and the measurements were made in immediate succession. The scatter of results falls within the histogram of repeated Q-factor measurements plotted in Figure 14.

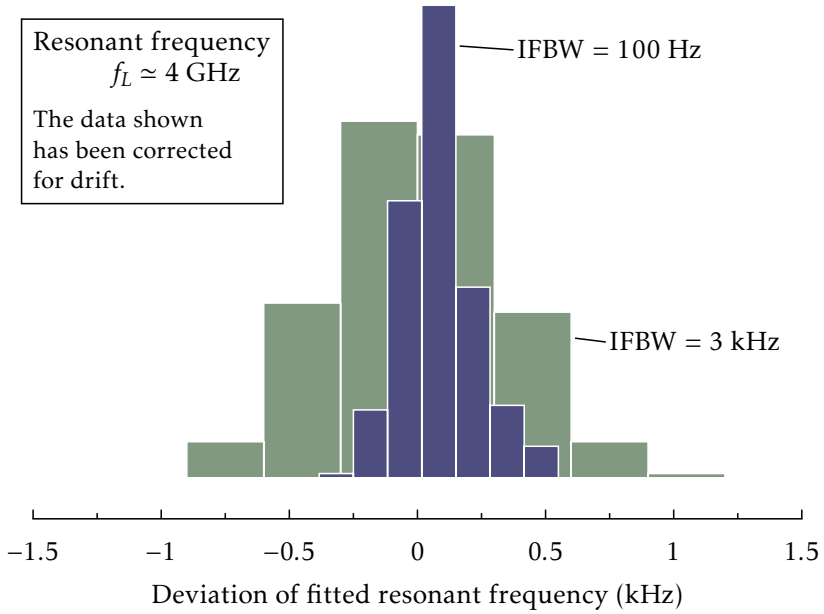

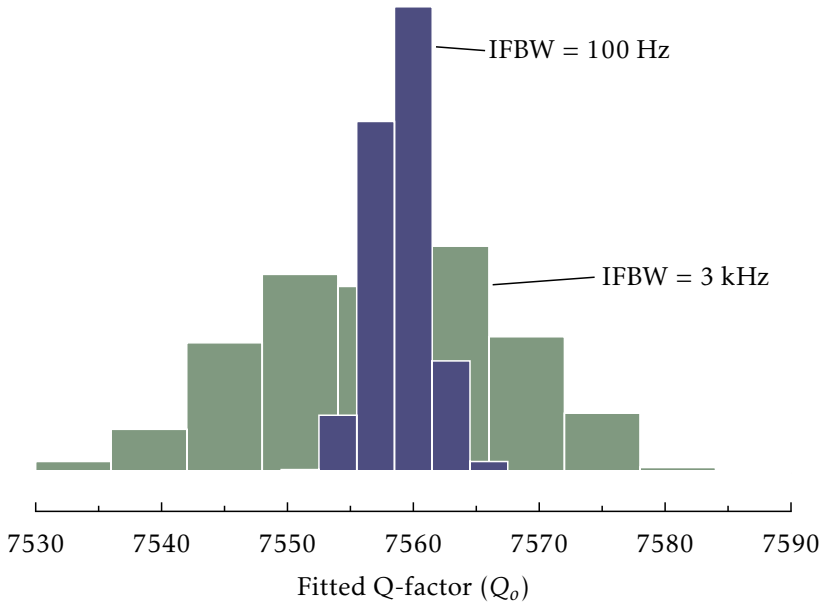

Figure 14: Histograms showing 500 repeated measurements of f_L and Q_o of a split-post dielectric resonator [51]. These results were obtained by fitting to complex S_{21} data with NLQFIT6. The VNA (Agilent 8753ES) was used uncalibrated, but the span was optimised as shown in Figure 6b. The couplings were adjusted to give equal coupling at each port, and so that at resonance $|S_{21}| \approx -40$ dB. Measurements were carried out with VNA IF bandwidth settings of 100 Hz and 3 kHz. Other VNA settings: 201 points, power level 0 dBm, averaging factor 1. Measurement repeatability as a function of the VNA power level is presented in Section 4.6.

Table 5: Measurements of Q-factor by transmission on a 4 GHz SPDR made with three different uncalibrated VNAs. A measurement on a 'thru' connection was made for each VNA for calculating Q_o (Section 2.5.2). All other conditions were the same for the three measurements. These results were obtained by fitting to complex S_{21} data with NLQFIT6.

VNA Model	Calibration	IFBW Setting	Measurements		
			A	Q_L	Q_o
Hewlett-Packard 8753E	Uncalibrated	100 Hz	1.107	7611	7706
Agilent 8753ES	Uncalibrated	100 Hz	1.048	7601	7706
Rohde and Schwarz ZVB20	Factory corr.	1 kHz	1.129	7602	7709

4.2 Reflection measurements

Measurements of the Q-factor of a one-port rectangular cavity (Figure 15) were made by the reflection method. Loop couplings of three sizes, formed from thick copper wire (1.5 mm diameter), were used for these measurements. Q-factors of a TE mode resonant at 3.7 GHz were fitted to complex S_{11} data by using NLQFIT7 and to $|S_{11}|$ data by using SCALARQ[12]. NLQFIT7 was used to measure Q_o with the VNA calibrated and also uncalibrated. SCALARQ, which uses a simplification to permit a three-coefficient fit [34], was used to find Q_o for calibrated measurements only as the calculation assumes that the VNA is calibrated and that the uncalibrated line is non-attenuating. The value of Q_o that is calculated by SCALARQ is corrected for the loop inductance if the fitted value of $|S_V|$ is significantly lower than unity (Figure 4). Coaxial GPC-7 standards were used to calibrate the VNA at the reference plane marked in Figure 15. The adaptor and SMA connector form an uncalibrated coaxial line (total length approximately 40 mm) that contains air and solid PTFE dielectric sections. The conductor diameters are chosen so that 50 Ω impedance is maintained throughout. To an approximation, the air and PTFE sections can be represented by a uniform material that has effective refractive index $\sqrt{\epsilon_r} = 1.3$.

Q-circles for the three coupling loops are shown in Figure 14, and Q-factors fitted with the VNA calibrated and uncalibrated are shown in Table 6. The size of the coupling is observed to have an appreciable effect on the cavity Q_o. For the large coupling the resonator is overcoupled, but for the other couplings it is undercoupled. The results provide several insights: Consistent results are obtained for different span widths (with some deterioration for wide spans using the VNA uncalibrated), which provides confidence in the measurement procedure. The diameter of the Q-circle for the large coupling is not much greater than that for the medium coupling, despite a considerable difference in the length of the wire forming the loop. In other words, the coupling factor is almost the same. This is in agreement with results presented in reference [66], which shows that, for an overcoupled resonator, loop inductance causes the coupling factor to be reduced. The fitted value of ℓ (shown in Table 6 for calibrated measurements fitted by NLQFIT7) is observed to be comparable to the physical length of the uncalibrated line for small and medium-sized couplings, but considerably greater for the large coupling (manifested by the visible asymmetry of the Q-circle).

Kajfez [21] provides an explanation for these observations: the Q-circle is asymmetric because the series reactance of the coupling loop depends on frequency. To investigate further, ℓ and the values of the components in the equivalent circuit (Figure 8) were fitted to the calibrated S_{11} data by using a library function (Levenberg-Marquardt method). Including L_s as a fitted parameter did not change the fitted results significantly; they were similar to the NLQFIT7

[12] SCALARQ is supplied on disk with reference [19] as a compiled DOS program.

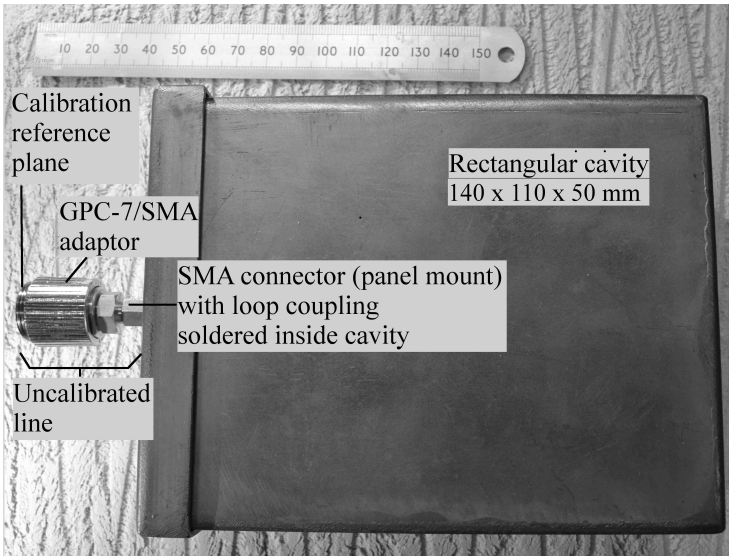

Figure 15: Rectangular cavity with loop coupling. Measurements of Q-factor by the reflection method are shown in Figure 16 and Table 6. A TE mode resonant at 3.7 GHz was selected for these measurements.

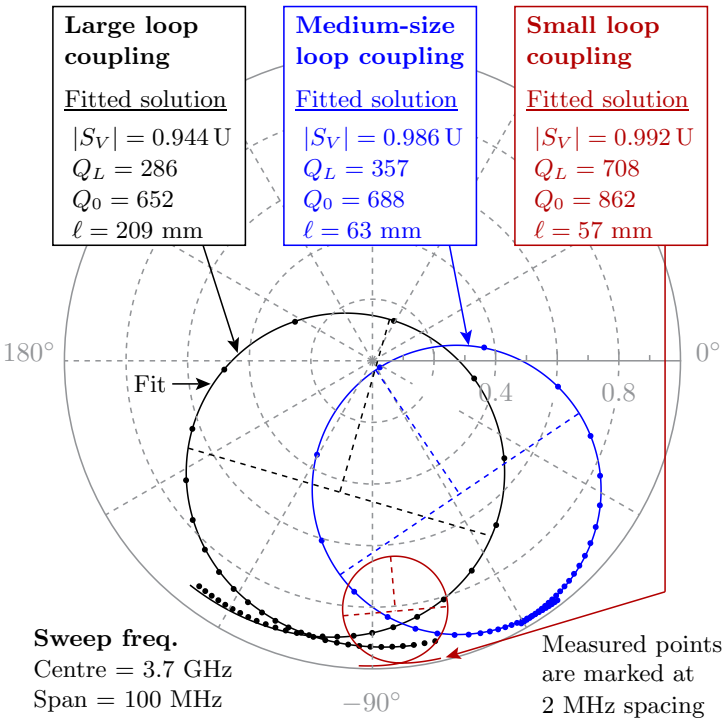

Figure 16: Measured complex reflection coefficients (S_{11}) of a rectangular cavity with loop couplings of three different sizes (made from 70 mm, 30 mm and 15 mm lengths of copper wire 1.5 mm diameter). These measurements were made with the VNA calibrated at the reference plane marked in Figure 15. Q-factor was determined by using NLQFIT7. The length of uncalibrated line ℓ is calculated from the fitted m_7 (see Section 2.3). The expected value of ℓ is 40–50 mm, but for the large coupling loop the fitted value is much higher.

Table 6: Measurements of the Q-factor of a rectangular cavity (resonant frequency 3.7 GHz) obtained by fitting to complex reflection coefficient data. Loop couplings with three sizes were used for these measurements. The results shown were obtained by fitting to calibrated and uncalibrated complex S_{11} data with NLQFIT7. ANGWTS are applied. Fits to the magnitude of the data obtained by using SCALARQ [34] are also presented. VNA settings: IFBW 100 Hz, averaging factor 1, source power level 0 dBm.

		NLQFIT7				**SCALARQ**
		Uncalibrated	*GPC-7 cal.*			*GPC-7 cal.*
		Q_o	†Q_o	‡Q_o	*ℓ	Q_o
Span	27 MHz	679	675	654	204	648
	50 MHz	681	675	654	204	650
	100 MHz	684	675	652	209	653

(a) Large coupling loop (70 mm length of copper wire formed into a loop).

		NLQFIT7				**SCALARQ**
		Uncalibrated	*GPC-7 cal.*			*GPC-7 cal.*
		Q_o	†Q_o	‡Q_o	*ℓ	Q_o
Span	27 MHz	693	696	693	63	691
	50 MHz	675	694	690	63	688
	100 MHz	663	691	689	63	686

(b) Medium-size coupling loop (30 mm length of copper wire formed into a loop).

		NLQFIT7				**SCALARQ**
		Uncalibrated	*GPC-7 cal.*			*GPC-7 cal.*
		Q_o	†Q_o	‡Q_o	*ℓ	Q_o
Span	27 MHz	841	863	862	57	861
	50 MHz	821	863	862	57	860
	100 MHz	806	862	862	57	859

(c) Small coupling loop (15 mm length of copper wire formed into a loop).

† Q_o is calculated by using *Method 1*. A_{11} is found from the fitted solution by using equation (34) to define a scalar calibration factor for a reference plane at the coupling loop.

‡ Q_o is calculated by using *Method 2*, which should give better accuracy than *Method 1* when the inductance of the coupling, L_s, is high. The calibration reference plane is marked in Figure 15. The attenuation of the uncalibrated line section is assumed to be negligible, i.e. $A_{11} = 1$.

* ℓ is calculated from the fitted m_7 value by using equation (27). The effective refractive index in the uncalibrated line (air and solid PTFE dielectrics) is taken to be $\sqrt{\epsilon_r} = 1.3$. For uncalibrated measurements, ℓ is not shown.

results shown in Table 6. For the large loop (100 MHz span), the fitted value of ℓ was 212 mm (i.e. greater than the actual length, but similar to the 209 mm fitted by NLQFIT7). The other fitted parameters were g = 0.32, d = 1.14, R_s =1.5 Ω, $\sqrt{LC} = 1/\omega$ = 42 ps, and L_s =−158 nH. How to interpret the data for the large loop is therefore rather unclear.

Consistent values for Q_o are fitted by NLQFIT7 and SCALARQ to calibrated S_{11} data for each of the loops. Uncalibrated measurements show greater dependence on span (suggesting that systematic uncertainties are significant). NLQFIT7 Q_o results calculated using *Method 1* and *Method 2* (Section 2.5.1) are similar to SCALARQ results for the small and medium-sized loops, but for the large loop *Method 2* gives better agreement. This experiment demonstrates that Q-factor measurements on a loop-coupled cavity should be made with couplings that have low inductance. This implies that they are small and therefore provide under-coupling. This finding is consistent with a published study of loop-coupled cavities by analytical and FEM methods [66].

4.3 Simultaneous transmission and reflection measurements

The ideal conditions for reflection and transmission measurement of Q-factor are opposite; requiring strong and weak coupling respectively. While strong coupling is the norm for measurements by reflection, convergence on a solution by using the NLQFIT algorithm can also be obtained if the coupling is weak. In this section, Q-factor measurements on a 4 GHz Split-Post Dielectric Resonator (SPDR) [51] made by both methods are compared. Attenuation in the uncalibrated lines (the semi-rigid cables shown in Figure 17) can be obtained from the fitted reflection Q-circles (if the VNA is calibrated and the coupling loss is negligible) and applied as a correction to Q_o measured by the transmission method. This procedure is described here, and the size of the correction is discussed.

One of the features of the SPDR is that it allows coupling factors to be changed with adjusters that move the coupling loops. Measurements were made with reflection Q-circle diameters at both ports set to 0.01, 0.05 and 0.1 Units to test the procedures used. The transmission Q-circle diameter is given by the geometric mean of the reflection Q-circle diameters [48], and therefore also has these values. The largest Q-circle diameter, 0.1 Units, is at the maximum of the adjustment range. The smallest Q-circle diameter, 0.01 Units, is about optimum for the transmission method, but is a stringent test for the reflection method.

S_{11} and S_{22} calibrations. Connection was via GPC-7/SMA adaptors to allow calibration using GPC-7 standards. A calibration on each port was carried out using match, short-circuit and open-circuit standards. The calibrations were performed with frequency span 25 MHz (centred on the resonance), which was broader than the swept range of any of the measurements. After optimisation of the sweep range to 70 % Q-circle (Figure 6b) “interpolated calibrations” (Section 3.2) were applied.

Reflection measurements on the SPDR. Calibrated and uncalibrated reflection measurements of Q-factor were made at both ports (Table 7). As noted in Section 3.3.2, vector measurements of Q-factor by reflection are very sensitive to the length of uncalibrated lines, so the results were obtained by fitting using NLQFIT7. Q_L data corrected for loading at the active VNA port are marked $Q_o^{(1)}$. These were obtained by using *Method 1*, which corrects for uncharacterised

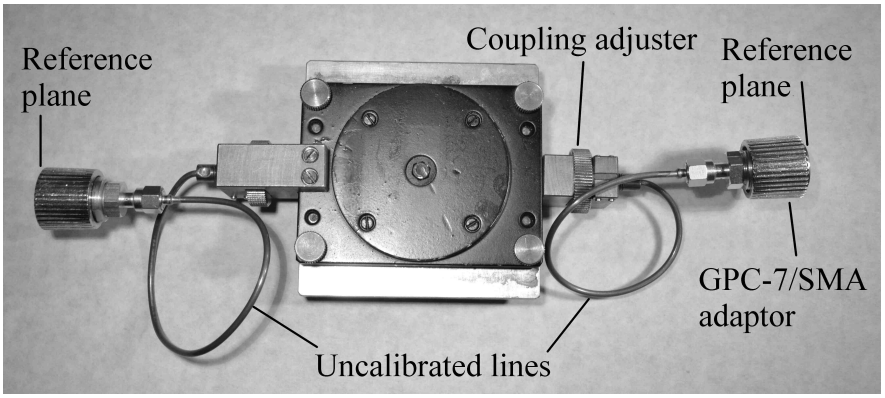

Figure 17: A Split-Post Dielectric Resonator [51] (SPDR). The quasi-TE01δ mode used for dielectric measurement is nominally at 4 GHz. Experiments described in Sections 2.6, 4.1 and 4.3 – 4.6 used this SPDR. A schematic diagram of an SPDR is shown in Fig. 29e.

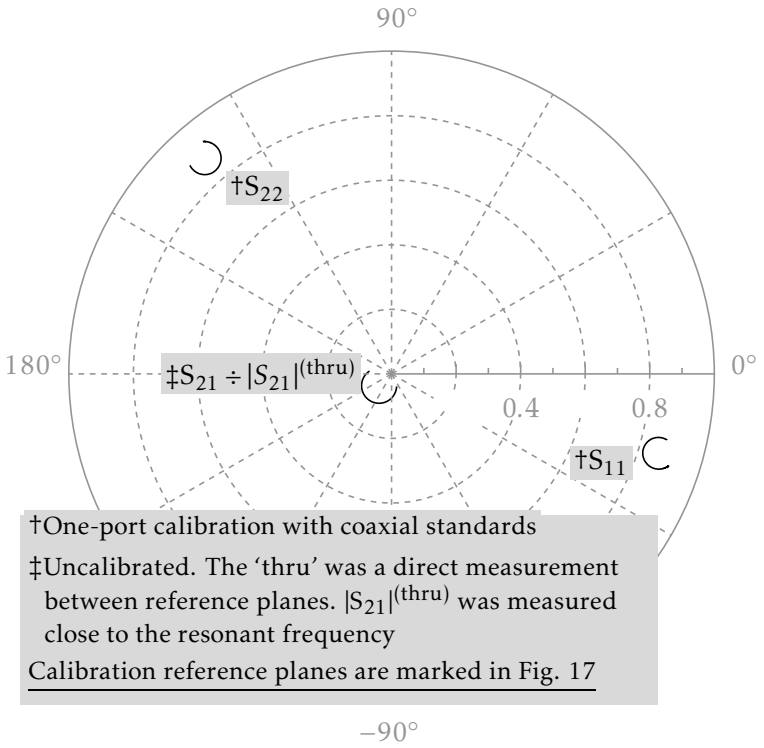

Figure 18: Measured complex S-parameters of a 4 GHz SPDR with couplings adjusted to set Q-circle diameters to 0.1 Units. S_{11} and S_{22} Q-circles were obtained with the VNA calibrated at each port independently for reflection measurement. The S_{21} Q-circle was obtained with the VNA uncalibrated. The S_{21} data is shown scaled by A_{21}, which was obtained from by measuring a "thru" connection between reference planes ($A_{21} = 1/|S_{21}|^{(\text{thru})}$). Attenuation in the uncalibrated lines causes the poles of S_{11} and S_{22} Q-circles to be inset from the edge of the polar chart, and the diameters of all three Q-circles to be reduced. This can be accounted for to improve the accuracy of calculations of Q_o for both transmission and reflection methods.

Table 7: Transmission and reflection measurements of the Q-factor of an SPDR resonant at approximately 4 GHz. Prior to measurements, couplings were adjusted to ensure that calibrated diameters of S_{11} and S_{22} Q-circles were approximately the same and as tabulated. Uncalibrated lines were de-embedded from uncalibrated S-parameter measurements using approximate lengths. Q-factors were then obtained by fitting to complex S_{21} data with NLQFIT6, and to complex S_{11} and S_{22} data with NLQFIT7. The sweep range was set to $f_L \pm f_L/Q_L$ (70% Q-circle) for every measurement. An Agilent 8753ES VNA was used as the measuring instrument. Settings: IFBW 10 Hz, averaging factor 1, number of points 101, power level 0 dBm. S_{11} and S_{22} calibrations were performed with GPC-7 coaxial standards prior to measurements. These calibrations were active only for the columns marked 'GPC-7 cal.'.

$Q_o^{(1)}$ is the unloaded Q-factor for measurement by reflection. It is calculated using *Method 1*, which corrects for uncharacterised attenuation (including that of uncalibrated lines). $Q_o^{(1)}$ does not account for loading by the inactive (but still connected) VNA port.

$Q_o^{(2)}$ is the Q-factor of the uncoupled resonator, i.e. unloaded by either VNA port. For the S_{21} measurement $Q_o^{(2)}$ was obtained using equations (31) and (38), where the attenuation of the uncalibrated lines is accounted for by using a modified expression for A_{21} (see text). The value of B (0.92) is calculated from the calibrated S_{11} and S_{22} measurements.

As the coupling factors at the ports were equal, estimates of $Q_o^{(2)}$ for reflection measurements can be obtained from the Q_L and $Q_o^{(1)}$ data given in the table. These values are shown in italics.

The results shown are averages of ten measurements ± standard deviations.

	Q	**S_{21}** ***uncal.***	**S_{11}** ***uncal.***	**S_{11}** ***GPC-7 cal.***	**S_{22}** ***uncal.***	**S_{22}** ***GPC-7 cal.***
Q-circle ⌀0.01 Units	Q_L	7470±1	6754±25	7477±35	6920±27	6983±37
	$Q_o^{(1)}$		6790±25	7516±35	6957±27	7017±37
	$Q_o^{(2)}$	7541±1	*6826*	*7555*	*6994*	*7051*
Q-circle ⌀0.05 Units	Q_L	7170.7±0.3	7145±5	7150±6	7145±8	7090±5
	$Q_o^{(1)}$		7320±6	7332±6	7330±8	7270±5
	$Q_o^{(2)}$	7523.2±0.4	*7499*	*7519*	*7519*	*7544*
Q-circle ⌀0.1 Units	Q_L	6789.0±0.3	6776±7	6749±2	6772±2	6730±2
	$Q_o^{(1)}$		7118±7	7103±3	7129±2	7084±3
	$Q_o^{(2)}$	7494.0±0.4	*7477*	*7476*	*7504*	*7456*

attenuation (including that of uncalibrated lines). Italicised $Q_o^{(2)}$ values are reflection measurements that have also been corrected for loading by the unused (but still connected) VNA port on the assumption that the port impedance does not depend on which port is powered.

The standard deviation of Q-factors fitted to Q-circles diameter 0.01 Units was $\sigma \approx 30$, which is significantly greater than for the larger Q-circles. Q-factors fitted to calibrated and uncalibrated data differ by $< 1\,\%$ in all cases except for the S_{11} measurement with Q-circle diameter 0.1 Units.

For Q-circle diameter 0.01 Units S_{11} and S_{22} Q-circles have poor shape. The likely reason for this is that mismatches associated with the SMA connectors are of comparable magnitude to the circle diameters (SMA are low-cost connectors that have larger mismatches than precision types of connector such as the GPC-7).

Transmission measurements on the SPDR. Transmission measurements of Q-factor were obtained by fitting to uncalibrated S_{21} data by using NLQFIT6 (Table 7). To enable unloaded Q-factors (denoted by $Q_o^{(2)}$) to be obtained, A_{21} was determined from a measurement on a "thru" at the resonant frequency.

Ideally the "thru" would have been semi-rigid cable of the same type and total length as the uncalibrated lines between the reference planes marked in Figure 17; however, such a cable was not available to hand so a direct connection was made. Calibrated S_{11} and S_{22} Q-circles (Figure 18) show that the uncalibrated lines cause significant attenuation which, if unaccounted for, causes unloaded Q-factors calculated using equations (31) and (38) to be under-estimated. The modified expression for $A_{21} = 1/(|S_{21}|^{(\mathrm{thru})} \times B)$ was used to correct for attenuation in the uncalibrated lines. The constant B is the geometric mean $|S_V|$ of calibrated S_{11} and S_{22} Q-circles, i.e. $B = \sqrt{|S_V|^{(S11)} \times |S_V|^{(S22)}}$. The two values of $|S_V|$ are by-products of calibrated measurements of Q-factor by reflection that are described above. For the resonant mode shown in Figure 18, it can be seen that $B \approx 0.9$; the calculated value was actually $B = 0.92$. The value of B obtained by this procedure can be recorded for future use as it is not likely to change. The error in $Q_o^{(2)}$ measured by transmission if attenuation in the semi-rigid cables is not accounted for (i.e. if B is assumed to be 1.0 instead of 0.92) can be calculated easily. For S_{21} Q-circle diameter 0.01 Units, the error in $Q_o^{(2)}$ is approximately $-0.1\,\%$ (which is barely significant). For S_{21} Q-circle diameter 0.1 Units, it is approximately $-1\,\%$.

Analysis. Measurements obtained by the transmission method (Table 7) had the smallest standard deviations. The range of adjustment for the couplers did not allow tests with stronger coupling, which would have improved the reproducibility of the reflection measurements. For Q-circle diameters 0.05 and 0.1 the $Q_o^{(2)}$ data for reflection and transmission methods is generally consistent to within 0.5 %. This is a good result for a resonator that was not designed for measurement by reflection.

4.4 On the effects of an imbalance between couplings

For lossless coupling, equation (42) may be used to calculate Q_o from d_1 and d_2, the fitted calibrated diameters of S_{11} and S_{22} Q-circles. If these are equal, that is $\beta_1 = \beta_2$, Q_o can be found more conveniently from the fitted calibrated diameter of the S_{21} Q-circle by using equation (38). The effect of a slight imbalance in the coupling factors on the value of Q_o calculated by using equation (38) is expected to be small when weak coupling is used. In this section, this assertion is tested in experiments with a 4 GHz SPDR that has mechanical adjusters that allow the coupling factor at each port to be set (Figure 17).

An 8753ES VNA was used for these tests. The IFBW was set to the lowest setting (10 Hz) to give the best measurement repeatability. The experimental procedure was as follows:

(i) Separate Port 1 and Port 2 reflection-mode VNA calibrations were performed at the measurement reference planes (Figure 17) by using GPC-7 coaxial standards.

(ii) $|S_{21}|^{(\mathrm{thru})}$ was measured using a direct "thru" connection at the resonant frequency (4 GHz). A_{21} was calculated accounting for attenuation in the uncalibrated lines as described in Section 4.3. The previously-measured value for B (=0.92) was assumed.

(iii) The SPDR was connected to the VNA.

(iv) NLQFIT7 was used to fit S_{11} and S_{22} Q-circles to swept measurements of the calibrated reflection coefficient at Port 1 and Port 2. The calibrated diameters of the fitted Q-circles (d_1 and d_2), corrected for attenuation in the uncalibrated lines, were obtained by using *Method 1*.

(v) NLQFIT6 was used to fit S_{21} Q-circles to swept measurements of uncalibrated transmission coefficient. The calibrated diameter of each fitted Q-circle (d_{21}), corrected for attenuation in uncalibrated lines, was calculated by using equation (31).

(vi) The couplings were adjusted so that $d_1 = d_2 = 0.01$ Units. It was observed that d_{21} was also 0.01 Units to within experimental error, which is expected as $d_{21} = \sqrt{d_1 d_2}$ for lossless coupling [48]. All measurements were performed with the VNA frequency span set to 70 % Q-circle. The value of Q_L fitted to the uncalibrated S_{21} data was recorded

(vii) Q_L, d_2 and d_{21} were re-measured at a number of settings of the coupling at Port 2 (with d_1 remaining constant at 0.01 Units).

Figure 19 shows Q_L as a function of d_2 (green line) measured by transmission. At each point Q_o is calculated with equation (38) (red line) and equation (42) (blue line). The measurements demonstrate that the simpler formula equation (38) enables Q_o to be calculated with sufficient accuracy for a weakly-coupled resonator even if there is a slight disparity between Q-circle diameters d_1 and d_2. Measurements by using a VNA that is uncalibrated or has a factory correction would in most cases be sufficient for setting the reflection Q-circle diameters; usually the easiest method is to adjust the depth of the S_{11} and S_{22} resonances on the "linear magnitude" display so that they are equal.

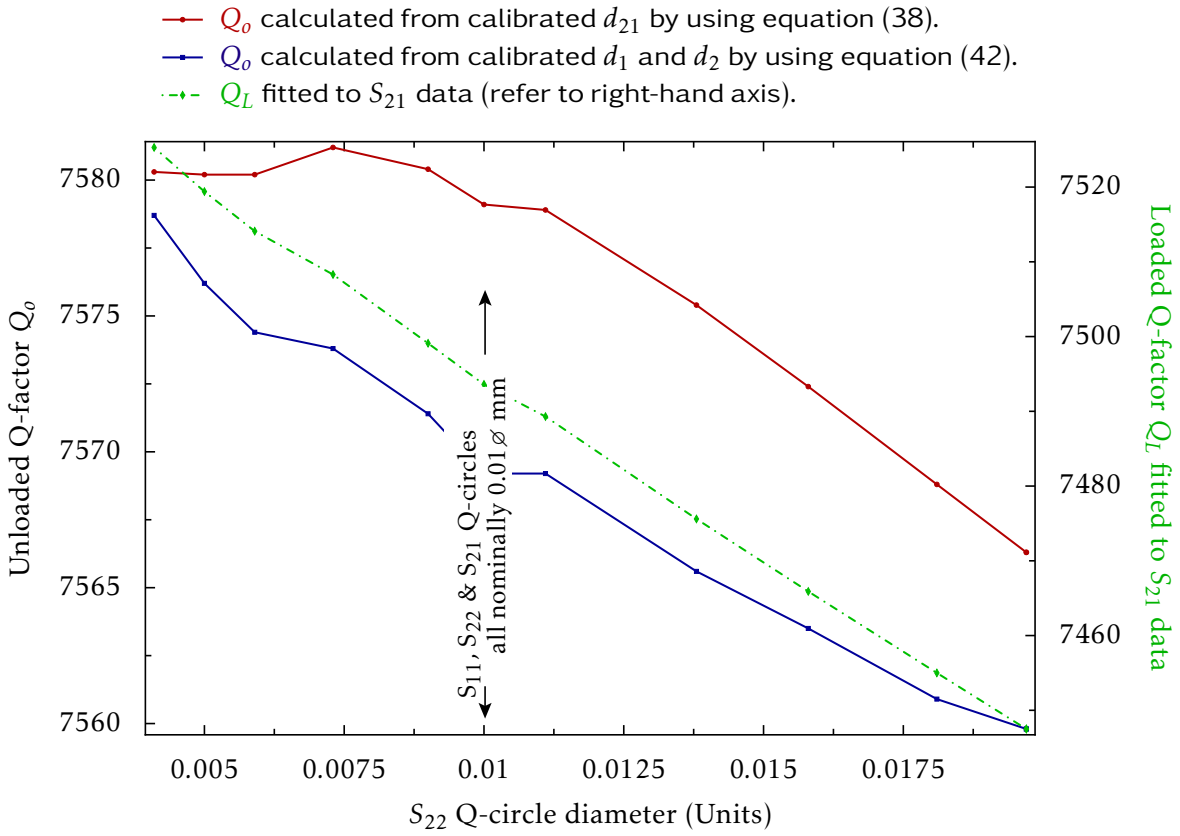

Figure 19: Measurements of Q-factor by transmission (S_{21}) as a function of the diameter of the S_{22} Q-circle (d_2) with the diameter of the S_{11} Q-circle (d_1) fixed at 0.01 Units. These measurements were made on a 4 GHz SPDR using a Rohde and Schwarz ZVB20 VNA. The VNA settings were: points 51, IFBW 10 Hz, averaging 1, power setting 10 dBm (S_{21}) and −5 dBm (S_{11} and S_{22}).

4.5 Transmission measurements on resonances of non-ideal shape

The shapes of the resonances of microwave resonators often deviate from the Q-circles in the complex plane that are predicted by RLC models. The effects of overlapping nearby resonances, for example, may be evident. It is often necessary to measure non-ideal resonances, so this section has been provided to suggest strategies that might be employed. NLQFIT can be used to estimate the Q-factors of resonances that have non-ideal shape, although for severely distorted resonances, convergence in Step (2) may be unobtainable.

It is important to note that there are two factors that affect the apparent shape of resonances that are accounted for by the measurement model, equation (7):

Leakage: The magnitude response of measurements by transmission has an asymmetric non-Lorentzian form (Figure 2) if there is leakage. This is not a cause of measurement error if Q-factor is fitted to complex data with an algorithm that accounts for the leakage, such as NLQFIT. Frequency-independent leakage has no effect on the circularity of Q-circles viewed on a polar display.

Uncalibrated lines: Frequency-dependent phase causes Q-circles measured by transmission to become distorted (Figure 9a) or, if there is no leakage, to adopt a cardioid shape (Figure 9b). Phase dependence has no effect on the magnitude response. When leakage and $\Delta\phi_w$ are low valued, as is typically the case for laboratory measurements, the effect on the shape of Q-circles is imperceptible. Where necessary, uncalibrated lines can be de-embedded to avoid error in the Q-factors fitted by NLQFIT6.

The 4 GHz SPDR (Figure 17) has many resonances over a wide band, as shown in Figure 20. The best resonances, such as the quasi-TE01δ mode (3.989 GHz) used for dielectric measurements [51], have Q-circles that are almost perfectly shaped (Figure 6b). The remaining resonances are observed to have varying degrees of non-circularity. The effect of uncalibrated lines on the shape of resonances is negligible as they are short and the leakage is low.

The resonance in Figure 20 at 9.746 GHz will be analysed in detail below. This is actually two superimposed resonances, as shown in Figure 21. The overlap will be a cause of systematic measurement error if the Q-factor of either resonance is obtained by fitting the single-resonance model, equation (21), to the data. The similarity of the response shown in Figure 21 to a Fano (coupled) resonance [39], might be noted, but in this analysis the measured S_{21} is assumed to result from the superposition of two resonances that are not coupled to each other. One method of improving the accuracy of Q-factor measurements is to fit to a dual-resonance model [67, 68]. Two simpler strategies that use the single-resonance model are considered here: (i) By fitting to only one half of the resonance of interest (on the opposite side to an interfering mode). (ii) By fitting a modified version of equation (21) to the data:

$$r_i = S_i - [m_1 + \mathrm{j}m_2 + (m_8 + \mathrm{j}m_9)t_i + (m_3 + \mathrm{j}m_4)y_i]. \tag{43}$$

The coefficients m_8 and m_9 represent "background" (or leakage) signal that is proportional to frequency [33]. It is a straightforward matter to modify the optimisation process described in Section 2.2 to fit equation (43) to the data. The modified algorithm has eight fitted coefficients in total, and is referred to as NLQFIT8.

When the data shown in Figure 21 is seen on a polar plot (Figure 22), it is evident that the weaker resonance (at 9.760 GHz) can be seen to be sitting on top of a tail of the stronger resonance. It is assumed that the weaker resonance can be represented approximately by equation (43). The sweep range was set to 70 % Q-circle ($f_L \pm f_L/Q_L$) prior to fitting Q-factors. The Q-circle fitted by NLQFIT8 is in better agreement with the measured data than the Q-circle fitted by NLQFIT6 (Figure 23), which is unsurprising because NLQFIT8 fits more coefficients. As an additional test, Q-factors fitted to "Lower 35 %" ($f_L - f_L/Q_L$ to f_L), "Upper 35 %" (f_L to $f_L + f_L/Q_L$) and 70 % Q-circles were compared (Table 8). The NLQFIT8 results have the best consistency, which suggests that it partially accounts for the overlapping stronger resonance. Some circumspection is due, however, as Table 8 shows significant discrepancies.

In a second experiment, Q-factor measurements on a number of resonances that had well-shaped Q-circles with no apparent interfering mode were made (Table 9). Q-factors were fitted by NLQFIT6 with the sweep range optimised (70 % Q-circle) as shown in Figure 6b. Results were also obtained with this sweep split into "Lower 35 %" ($f_L - f_L/Q_L$ to f_L) and "Upper 35 %" (f_L to $f_L + f_L/Q_L$) Q-circles. It can be seen that results at 3.989 GHz and 9.188 GHz for the three different sweep ranges in Table 9 show markedly more consistent results than those at other frequencies, indicating that these resonances have the best shape. These measurements demonstrate the value of performing measurements on each side of the peak to gain insight into how well the equivalent circuit, Figure 7, describes actual resonances.

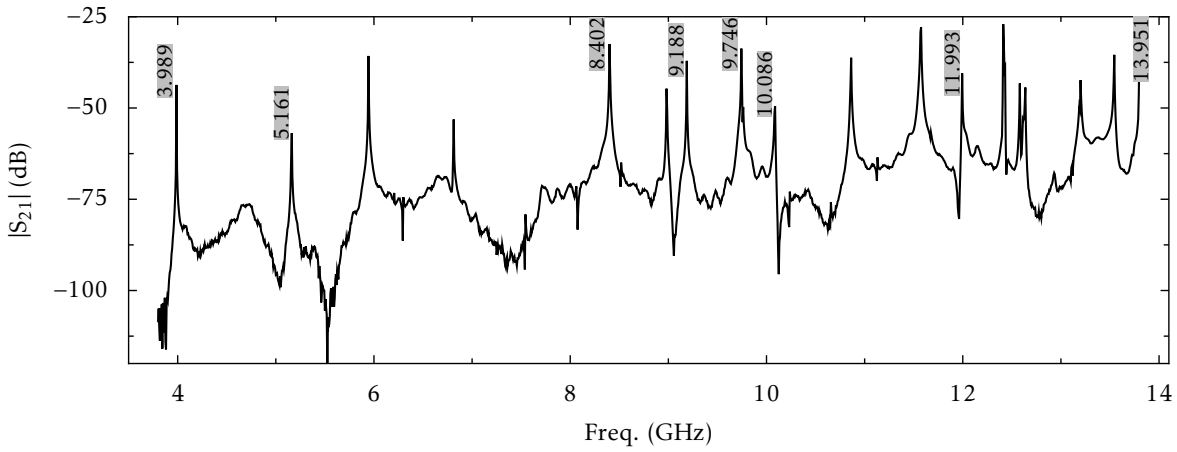

Figure 20: Spectrum of a 4 GHz SPDR [51] showing multiple resonances. The frequency of the quasi-TE01δ mode is 3.989 GHz.

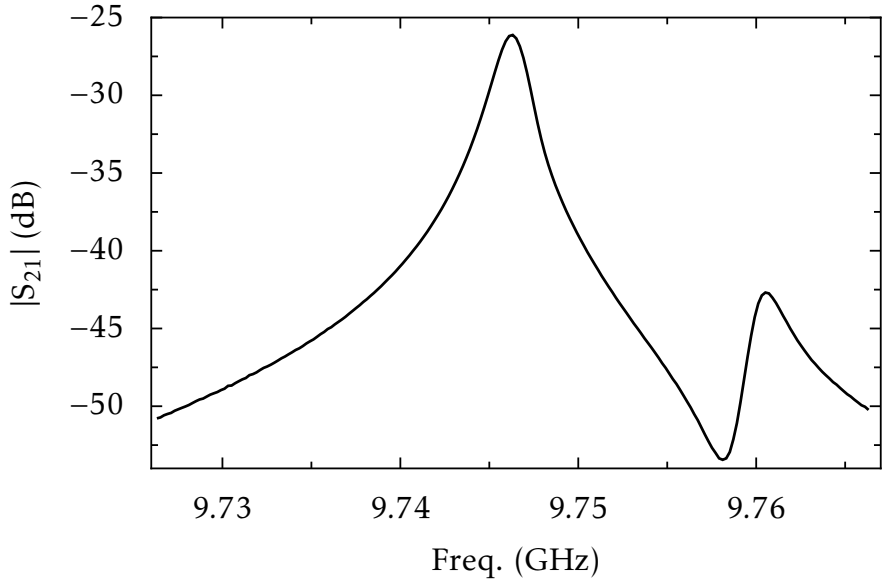

Figure 21: The resonance at 9.746 GHz shown in Figure 20 is seen to have two resonant peaks when viewed with the sweep span reduced.

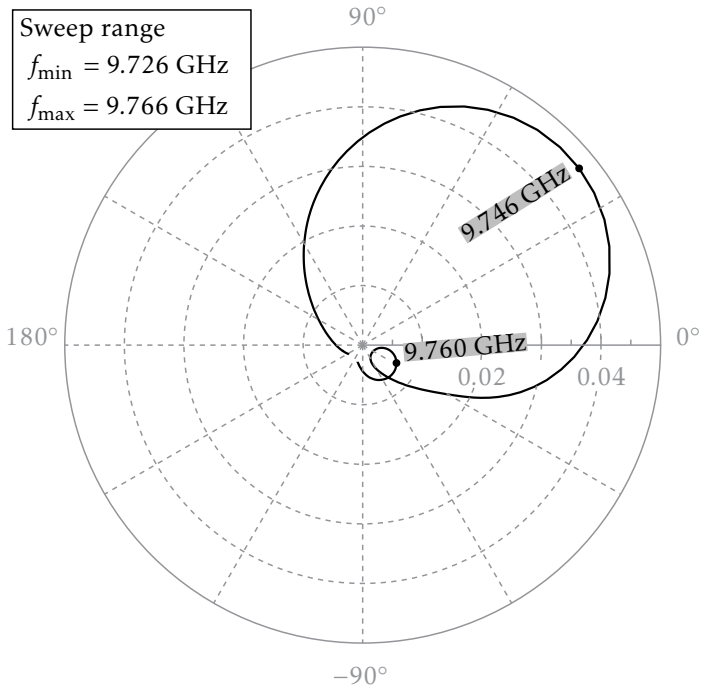

Figure 22: Measured S_{21} Q-circles of two overlapping resonances shown in Figure 21. Two Q-circles can be seen.

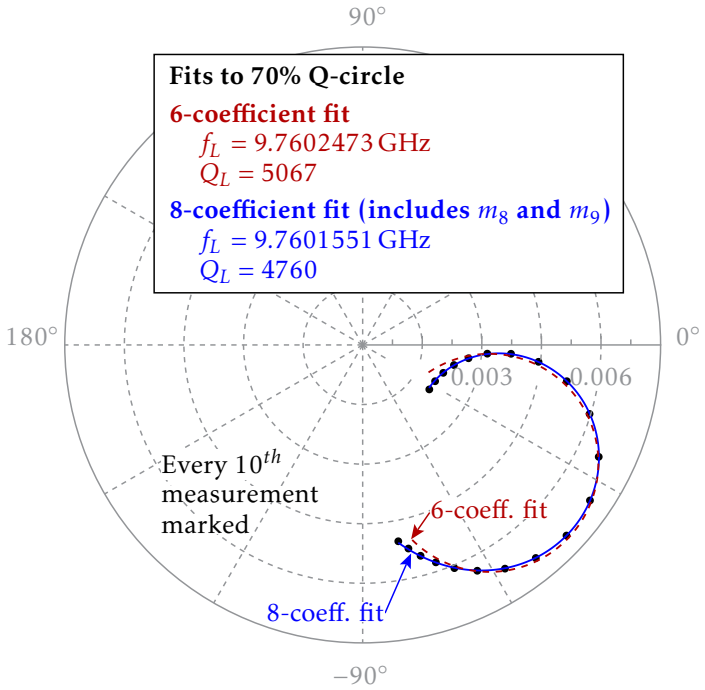

Figure 23: Complex transmission coefficients (S_{21}) of the 9.760 GHz resonance shown in Figures 21 and 22. Actual measurements are marked with dots. Dashed and solid lines show S_{21} data calculated from fitted 6-coefficient (NLQFIT6) and 8-coefficient (NLQFIT8) models respectively.

Table 8: Measurements of the Q-factor of one of the many resonances of the 4 GHz SPDR. This resonance (frequency 9.760 GHz) sits on the tail of a larger resonance – see Figure 21. These measurements were made in transmission with a Rohde and Schwarz ZVB20 VNA. The VNA was uncalibrated (factory correction only). The sweep had 201 points and the IFBW was set to 10 Hz. The S_{21} measurements are plotted in Figure 23. The Q_L values shown were obtained by fitting using NLQFIT6 and NLQFIT8 for varying swept-frequency ranges.

	Q_L					
	Fitted by NLQFIT6			**Fitted by NLQFIT8**		
Freq. GHz	**70% Q-circle**	**Lower 35% Q-circle**	**Upper 35% Q-circle**	**70% Q-circle**	**Lower 35% Q-circle**	**Upper 35% Q-circle**
9.760	5067	4843	4532	4760	4653	4715

Table 9: Measurements of the Q-factor of resonances of the 4 GHz SPDR. The resonances selected have well-shaped Q-circles. These measurements were made in transmission with a Rohde and Schwarz ZVB20 VNA. The VNA was uncalibrated (factory correction only). The sweep had 201 points and the IFBW was set to 10 Hz. With these settings, the short-term repeatability of measurements of Q_L was approximately ±2. The Q_L values shown were obtained by fitting using NLQFIT6 for varying swept-frequency ranges.

	Q_L fitted by NLQFIT6		
Freq. GHz	**70% Q-circle**	**Lower 35% Q-circle**	**Upper 35% Q-circle**
†3.989	7517	7518	7518
5.161	5244	5142	5461
8.402	4408	4333	4429
9.188	4141	4142	4144
10.086	2541	2575	2515
11.993	3928	3964	3915
13.951	3142	3073	3239

†SPDR quasi-TE01δ mode.

4.6 The effect of the VNA power settings

In this section, the linearity of the receivers of an Agilent 8753ES VNA is studied by measuring Q-factor as a function of the power-level set by using the VNA's built-in controls. To allow a broader range of adjustment, this model is also equipped with a stepped attenuator (settable at 10 dB steps). The power-level settings of the 8753ES (and the similar 8753E) are set during the manufacturer's factory calibration by means of a calibrated power meter that is connected to the front-panel ports. The stepped attenuator is also calibrated during the factory calibration. A traceable assessment of the linearity of measurements of Q-factor (i.e. the dependence of readings on the settings of the VNA power controls) can therefore be undertaken without additional equipment. The linearity of VNA receivers can also be evaluated with externally-connected calibrated attenuators (Section 3.2.1).

Figure 24 shows the architecture [11] of the 8753E/8753ES test-set in simplified form. The main components are a microwave source, a stepped attenuator, mixers, receivers and an RF switch. The stepped attenuator allows the signal levels at the receivers A and B to be set below that at the receiver R. S-parameters are given by ratios A/R and B/R (measurement of all four S-parameters requires readings at each position of the RF switch). It might be noted that changing the output power setting of the microwave source affects the signal at all of the receivers, so in a linear system it should not affect the measured S-parameter ratios. The VNA applies corrections (with data from the factory calibration provided by the manufacturer) so that S-parameter readings are nominally independent of the setting of the stepped attenuator. VNA calibration with impedance standards, if required, should nevertheless be performed at the same attenuator setting that is to be used for measurements to give the best accuracy.

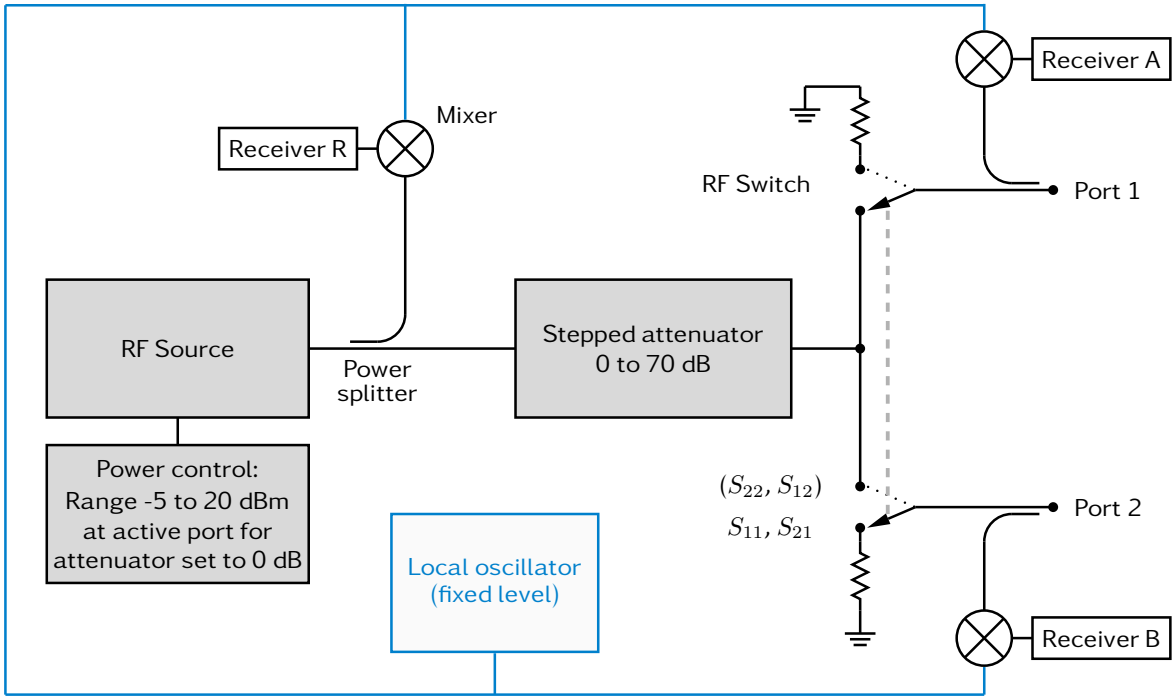

Figure 24: Simplified schematic of the source and test-set used by 8753E & 8753ES VNAs. Uncorrected S-parameters are obtained from measured ratios, e.g. S_{11} = A/R with the RF switch set as shown. The VNA software uses scaling factors to ensure that measured S-parameters do not depend on the setting of the stepped attenuator. The scaling factors are determined by the manufacturer's factory calibration.

Table 10: Average and standard deviations of 250 measurements of Q_L by transmission as a function of the power level at the VNA port. They were obtained by fitting with NLQFIT6. The tabulated power levels are the values that would be indicated by a power meter (impedance 50 Ω) attached to the active VNA port. The measurements were performed in a temperature-controlled laboratory using an Agilent 8753ES VNA. Settings: IFBW 100 Hz, averaging factor 1. There were 201 points in the sweep. The resonator was a 4 GHz SPDR (Figure 17) with couplings adjusted so that at resonance $|S_{21}| \approx -40$ dB. The 10 dBm and 20 dBm power settings are obtained with the stepped attenuator (Figure 24) set to 0 dB. For the measurements at −10 dBm to −40 dBm the source power is fixed at 0 dBm (so the power seen by the 'R' receiver is constant) and the stepped attenuator setting is varied.

Nominal power at VNA port (dBm)	**Uncalibrated VNA**	
	Average Q_L	**Standard deviation of Q_L data**
20 (first measurement)	7429.6	0.6
10	7430.1	1
0	7434	4
-10	7423	9
-20	7451	29
-30	7427	87
-40	7474	270
20 (final measurement)	7432	1

Measurements were made by transmission on the SPDR shown in Figure 17, and by reflection on the rectangular cavity shown in Figure 15. Modes that resonate at approximately 4 GHz were chosen. The averages and standard deviations of fitted Q-factors are shown in Tables 10 and 11. After the completion of each set of measurements, the first measurement (power-level setting 20 dBm) was repeated to allow the drift to be seen. The coupling of the reflection cavity was adjusted to that the Q-circle diameter was quite high (0.76 Units) to give optimum measurement repeatability. The SPDR measurements were made with the couplings adjusted for $|S_{21}| \approx -40$ dB at resonance.

No evidence of *compression* can be discerned for transmission measurements (Table 10) at 4 GHz, even at the highest power levels (the observed standard deviation of Q-factor measurements, ±4 at the 0 dBm setting, can be taken to be the upper limit to the effects of compression). If the insertion loss of the resonator were reduced by using stronger couplings, compression at the higher power settings would be expected. The standard deviation of the transmission Q_L data is observed to be approximately inversely proportional to the square root of the source power.

Uncalibrated reflection measurements (Table 11) show compression at power levels of approximately −10 dBm and above. Further tests (also shown in Table 11) showed that the same behaviour is obtained if the VNA is calibrated at each specified power level. The finding that the power level has to be reduced to approximately −10 dBm to avoid compression is consistent with a linearity check on this VNA made with a stepped attenuator by the method described in Section 3.2.1. Measurements by reflection have better repeatability (expressed as % of Q_L) at a given VNA power level than the transmission measurements shown in Table 10. This finding is consistent with a worse signal-to-noise ratio for measurement by transmission as a consequence of the use of weak coupling.

Table 11: Average and standard deviations of 250 measurements of Q_L by reflection as a function of the power level at the VNA port. They were obtained by fitting with NLQFIT7. The tabulated power levels are the values that would be indicated by a power meter (impedance 50 Ω) attached to the active VNA port. The resonator was the rectangular cavity shown in Figure 15. A TE mode resonant at 3.7 GHz was chosen. The measurements were performed in a temperature controlled laboratory using an Agilent 8753ES VNA. Results were obtained with the VNA uncalibrated and calibrated. A separate calibration was carried out at each specified power level. Settings: IFBW 100 Hz, averaging factor 1. There were 201 points in the sweep. The calibrated diameter of the Q circle was 0.76 Units. The 10 dBm and 20 dBm power settings are obtained with the stepped attenuator (Figure 24) set to 0 dB. For the measurements at −10 dBm to −60 dBm the source power is fixed at 0 dBm (so the power seen by the 'R' receiver is constant) and the stepped attenuator setting is varied.

Nominal power at VNA port (dBm)	**Uncalibrated VNA**		**Calibrated VNA**	
	Average Q_L	**Std. dev. of Q_L data**	**Average Q_L**	**Std. dev. of Q_L data**
20 (first measurement)	522.69	0.02	516.89	0.02
10	507.40	0.02	502.62	0.02
0	504.74	0.03	500.78	0.03
-10	502.13	0.05	501.26	0.07
-20	503.45	0.05		
-30	503.4	0.2		
-40	501.9	0.4		
-50	502	1		
-60	502	4		
20 (final measurement)	522.71	0.02		

Measurements such as those shown in Tables 10 and 11 can be used to determine an appropriate output power-level setting for a particular VNA. For the transmission measurements with the 8753ES a setting of 0 dBm gives more than adequate measurement repeatability for most applications, but there is some scope to use higher settings for both the power level and the IFBW to obtain the same repeatability with shorter measurement times without running into compression. For reflection measurements of Q-factor the power level must be set more cautiously; for many purposes a setting of 0 dBm (at which compression is slight) would be suitable for the instrument characterised in Table 11. The majority of the measurements presented in this report (both transmission and reflection) were made by using Agilent 8753-series instruments with the power level set to 0 dBm (source power 0 dBm, stepped attenuator set to 0 dB).

The effects of VNA non-linearity on the measurement of the Q-factor of a weakly-coupled parallel LC circuit that resonates at 33 MHz were also studied. The circuit in question was actually a Hartshorn and Ward experiment (see reference [69] and Figure 31) that is used for measurement of the loss angle of low loss materials such as polyethylene. To resolve small loss angles, small changes in the Q-factor (≈0.02) of a system that resonates with fairly low Q-factor (≈200) must be measured. This requires a balance to be found between instrument settings for averaging (to avoid drift caused by prolonged measurements) and power (to achieve low noise levels without compromising the linearity). Figure 25 shows measurements at 10 dBm, 3 dBm and 0 dBm source power settings using a Hewlett-Packard 8753E VNA. Readings at 0 dBm made with the VNA internal stepped attenuator set to 10 dB and 20 dB are also shown. The

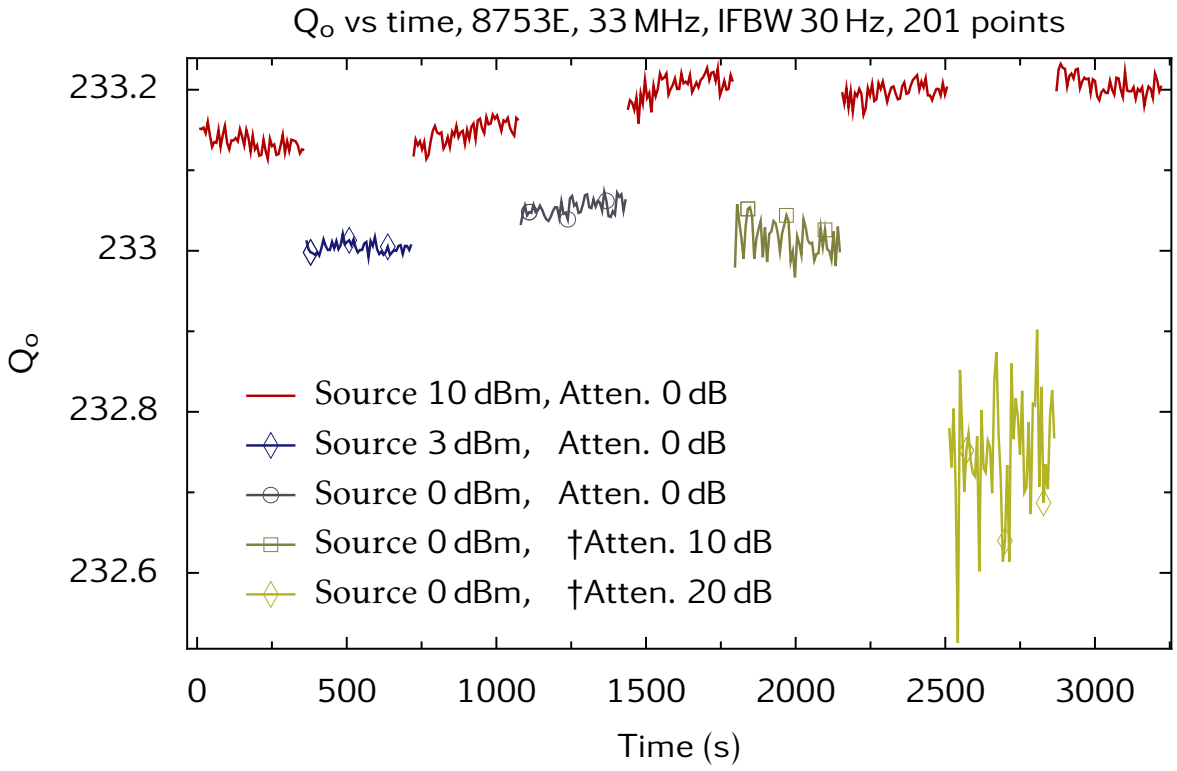

Figure 25: Measurements of the Q-factor of a parallel coil and capacitor resonant at 33 MHz as a function of the settings of the VNA source power and stepped attenuator controls as shown in Figure 24. NLQFIT6 was used to fit Q-factor to the data (201 trace points). The span width was optimised as described in Section 2.6. The measurements were made using weak coupling (transmission loss at resonance 30 dB). The measuring instrument was a Hewlett-Packard 8753E VNA. There are 50 measurements in each of the 9 sets of data plotted. Interleaved measurements of Q-factor at power 10 dBm (red traces) are shown so that the effects of drift in the laboratory temperature can be seen. The resonator couplings were adjusted to set the transmission loss of the resonator to 40 dB at resonance.

†VNA stepped attenuator as shown in Figure 24. B/R is corrected by using data in the VNA factory calibration.

measured ratio B/R is nominally unaffected by the attenuator setting as corrections stored in the VNA as part of its factory calibration are applied. The fractional reduction in measured Q-factor (which is evident in both Q_o and Q_L data) at the 20 dB setting is evidence of non-linearity. Measurements at 10 dBm are interleaved between measurements at other settings so thermal drift in the system is distinguishable from other trends in the data. For this instrument, the lowest noise level is obtained at a source power level of 3 dBm.

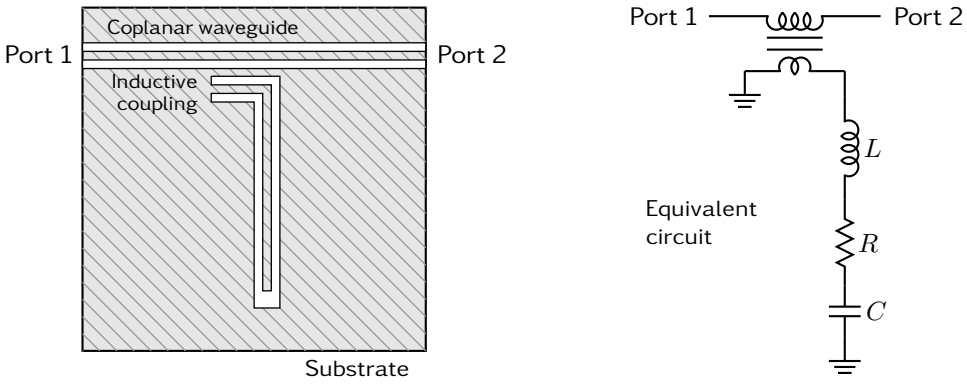

Figure 26: On-chip absorption or "notch" resonator based on a $\lambda/4$ coplanar waveguide.

4.7 Measurements on a two-port absorption resonator at cryogenic temperatures

Absorption resonators can be fabricated on a chip from microstrip [70, 71] or coplanar waveguide [29, 72]. At resonance a "notch" in the magnitude of S_{21} is observed as a result of coupling between the waveguide and the resonator. The coplanar waveguide resonator shown in Figure 26 can be used for the measuring the dielectric loss of thin films at low temperatures [73, 74]. Figure 27 shows a Q-circle measured in transmission by using a VNA. Very high Q-factors (over a million) can be obtained as a result of superconductivity.

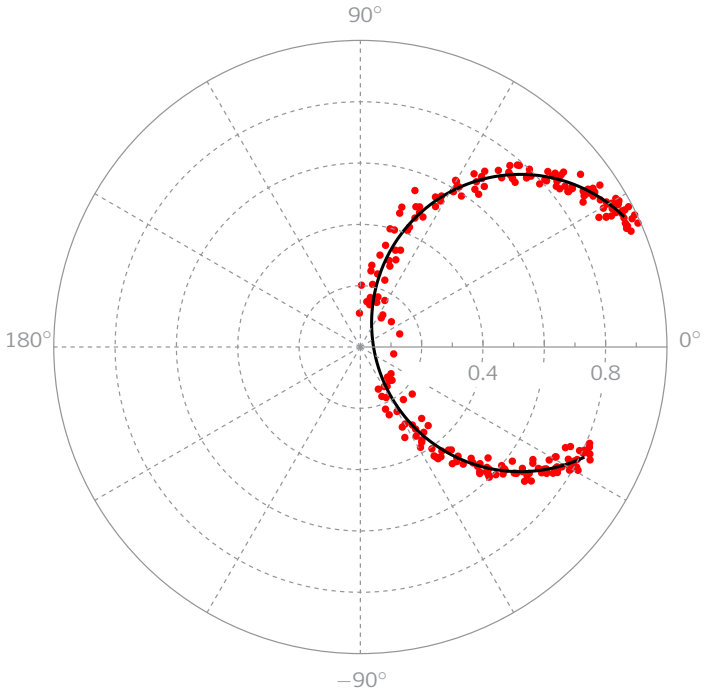

Figure 27: Measured S_{21} Q-circle of a superconducting two-port absorption resonator (Measurements by Z. Ali, NPL). The data has been normalised to the fitted off-resonance value of $|S_{21}|$. The solid line is the Q-circle fitted by NLQFIT6.

For the absorption resonator, the unloaded Q-factor Q_o is related to the loaded Q-factor Q_L by

$$Q_o = Q_L\left(1+\beta\right) \tag{44}$$

where

$$\beta = \frac{1}{\frac{1}{d}-1}. \tag{45}$$

The above expressions were obtained from the thesis by J. Gao [28] (equations 4.35 and 4.40). For this resonator configuration, critical coupling occurs when $d = 0.5$. Cryogenic measurement requires that the VNA is connected via transmission lines that pass through the wall of the cryostat. These cause significant attenuation, so low-level signals must be measured. If signal paths due to leakage can be neglected, the calibrated Q-circle diameter d can be obtained by using equations (31) and (34). Q_o can therefore be obtained without a requirement for VNA calibration.

Q-factors were fitted to the resonance shown in Figure 27 by using NLQFIT6 and by the circle-fitting method described by Probst [29, 75]. The estimated value of f_L that is required for fitting by using NLQFIT6 was taken to be the point in the frequency sweep at which the magnitude of the S_{21} data is smallest. The fitted resonant frequencies and loaded Q-factors (Table 12) are in good agreement. The measured device was significantly overcoupled to maximise the measured signal and enable more rapid readout of frequency shifts. The calculated unloaded Q-factor is therefore very sensitive to the fitted d as it is almost one. This is at least part of the explanation for the difference in the tabulated unloaded Q-factors.

Table 12: Comparison of resonant frequency and Q-factor fitted by NLQFIT6 and circle-fitting [29, 75] algorithms for a superconducting absorption resonator. The measured data is plotted in Figure 27. The circle-fit Q_o shown is the "diameter corrected" value outputted by Probst's software [75].

Algorithm	**Freq. GHz**	$\mathbf{Q}_L$	$\mathbf{Q}_o$
NLQFIT6	6.07225567	56020	1846803
Circle fit	6.07225577	55990	1514806

5 The Uncertainty of Measurements of Q-factor

The evaluation of uncertainty in general is a much studied topic on which there are numerous publications. The most prominent of these is the ISO Guide to Uncertainty in Measurement (GUM) [76], which defines methods for evaluating uncertainty that have been adopted internationally. There are not many publications that present evaluations of the uncertainty of measurements of Q-factor. References [18, 35, 48, 49] are among those that do.

Evaluation of uncertainty using the GUM requires that there is a *measurement model* [77] that defines a relationship between *input quantities* and the *measurand* (the output quantity from the model, e.g. Q-factor). For some disciplines, measurement models are defined empirically, but for most experiments they are equations. The uncertainty of the measurand can be

determined by using the *law of propagation of uncertainty*. This requires the size of the uncertainty associated with each input quantity to be evaluated, and the corresponding sensitivity coefficient to be calculated. The overall uncertainty can be calculated from a quadrature sum of the products of uncertainties and sensitivity coefficients assuming that there are no correlations between the contributions. This can be multiplied by a coverage factor (k) to give the expanded uncertainty [76], which is the number that is usually quoted. The coverage factor $k = 2$ is normally applied when it can be assumed that the measured value has been drawn from a normal distribution of possible values, as this gives a confidence level of 95% that the true value is within the specified uncertainty range.

In the GUM approach, a distinction between random uncertainties (which are designated as *Type A*) and all other types of uncertainty (which are designated as *Type B*) is made. Type B uncertainties include uncertainties associated with the calibration of instruments used to collect data. They also include *model uncertainties*, which occur if the measurement model used is not exact for the ranges of input quantities that are used. A supplement to the GUM [77] includes a discussion of methods for assessing the adequacy of measurement models.

This section considers the GUM approach to the evaluation of the uncertainty associated with the measurement of Q-factor. Model uncertainties are discussed in Section 5.1, and the Type A and Type B uncertainties associated with input quantities (measured S-parameters etc.) are discussed in Section 5.2. An evaluation of uncertainty is presented in Section 5.5.

5.1 Model uncertainties and the measurement of Q-factor

The measurement model describes how Q-factor is determined from S-parameters measured by a VNA that is connected to a resonator through uncalibrated lines. The model is based on approximations and limited knowledge. The resulting model uncertainties can be classified by:

- Uncertainties associated with the equivalent-circuit model used to represent the resonator and couplings as a whole.
- Uncertainties associated with the model representation of uncalibrated lines. In this report, it is assumed that the uncalibrated lines are coaxial cables that have the same characteristic impedance as the VNA (50 Ω).
- Uncertainties associated with model used for calculating Q_o. This assumes that external circuits (i.e. the VNA ports) can be represented by pure resistors, and that there is no coupling loss.

Equivalent circuits (Section 1.1) are usually good representations of tuned circuits that resonate at kHz/MHz frequencies. Distributed resistance, capacitance and inductance are not accounted for, but model uncertainties are usually low (< 1%). Equivalent circuits are often less successful at describing the resonances of microwave dielectric and cavity resonators, as these may exhibit complex behaviour that is governed by unknown parameters. Therefore, significant model uncertainties may arise. Many of the resonances shown in Figure 20, for example, do not have the Lorentzian form predicted by the measurement model.

Artefect Q-standards (Section 5.3) can be useful for assessing the model uncertainties associated with measurement of the Q-factor at kHz/MHz frequencies. Assessment of model uncertainty is more difficult as microwave Q-standards are not generally available. Studies of the consistency of the measurand (the Q-factor) under various conditions (Section 5.4) can be used to inform evaluations of model uncertainty. Some caution is needed, however, as the differences between such test results could be affected by unknown common factors relating e.g. to couplings. In other words, they are subject to unknown correlations and can under-represent the uncertainty.

5.2 Uncertainties associated with input quantities

By using the measurement model, the Q-factor (the measurand) can be calculated from input quantities. These are subject to uncertainty as follows:

- Type A uncertainty associated with measured S-parameters, such as random noise. It is usually preferable to evaluate the repeatability of fitted Q-factors (Figure 14), rather than the uncertainty associated with the S-parameter measurements.
- Type B uncertainties associated with the S-parameters measured by the VNA. These include contributions associated with mismatch effects (which will be increased if the VNA is uncalibrated) and receiver linearity.
- Uncertainty in the data that describe the uncalibrated lines: attenuation and $\Delta\phi_w$, where $\Delta\phi_w \equiv \Delta\phi_w\left(\bar{l}, \epsilon_r, f_L/Q_L\right)$ – see equation (9). There are some exceptions when this data is not needed: e.g. it is not necessary to make an independent measurement of the attenuation of uncalibrated lines when A is obtained by using equation (34). This applies to measurement by reflection when *Method 1* is used, and to the two-port absorption measurement described in Section 4.7. Otherwise, the attenuation (and its uncertainty) must be considered when an estimate for Q_o (and its uncertainty) are required. $\Delta\phi_w$ is not required for measurements of Q_L and Q_o if NLQFIT7 or a scalar technique is used.
- For transmission measurement, differences in the coupling factors at the two ports should be considered to be an uncertainty if equation (38) is used to determine Q_o. This contribution arises because the diameters of reflection Q-circles d_1 and d_2 are in practice not exactly equal.

5.3 Artefact Q-standards

At MHz frequencies and lower, it is possible to obtain impedance standards such as very low loss capacitors (air dielectric), and stable hermetically-sealed coil inductors. These can be characterised precisely by using calibrated LCR meters or impedance bridges [78–82]. Traceability of Q-factor measurements to impedance standards can therefore be established by combining capacitance and inductance standards [36, 78, 79].

At microwave frequencies satisfactory artefact Q-standards have not been established to the author's knowledge. The Q-factor of a metal-walled cavity can be calculated from the resonant mode, conductivity, dimensions and cavity shape [83]; indeed Pozar [1] and Moreno [84] provide approximate formulas for rectangular and cylindrical cavities. Unfortunately, the precision to which Q-factor can be calculated is limited by factors such as the effects of couplings, and losses at joints in the cavity walls. More fundamentally, the high-frequency conductivity of metals is not traceable to low-frequency measurements [85] because of effects such as surface roughness and oxidation [86–88].

5.4 Tests of consistency

Rigorous approaches [76] can be used to evaluate the uncertainties of input data, but this is not the case for model uncertainties. These are estimated on the basis of accumulated evidence. Measurements by different techniques can be used to gain confidence in measurements of Q-factor and evaluations of the associated uncertainty:

- Tests against Q-standards can be made. These are only available at kHz/MHz frequencies (Section 5.3).
- NLQFIT results can be compared to those obtained by other methods such as the Resonance Curve Area (RCA) method (Section 1.3.4). The RCA method is appropriate for transmission measurements when the leakage is low. The "rectangle rule" can be used to estimate the area beneath the resonance. For example, for the quasi-TE01δ mode of an SPDR (Figure 6b), the RCA method gave Q_L = 7458. This differs negligibly from the value fitted by NLQFIT6, Q_L = 7454. For an asymmetric mode at 8.4 GHz (as given in Table 9, but measured on a different occasion), the RCA method gave Q_L = 3617 and NLQFIT6 gave Q_L = 3848 – a 6 % difference.
- Measurements can be made with varying sweep ranges, as shown in Table 9.
- The consistency of resonator measurements of the dielectric loss (δ) of reproducible materials can be studied. Measurements of δ are subject to several sources of uncertainty and do not provide specific information on the uncertainty of Q-factor measurements.

5.5 Example – uncertainty of measurement of the Q-factor of an SPDR

A measurement of the Q-factor of the SPDR that is shown in Figure 17 is taken as an example. The 70 % Q-circle is plotted in Figure 6b. Q_o is calculated to be 7554 (Table 13) when the small correction for attenuation in uncalibrated lines is included.

Table 13: The data in Figure 6b revised with a correction to account for attenuation in the uncalibrated lines (the semi-rigid cables shown in Figure 17). All results are computed by NLQFIT6.

Description of correction	**Numerical value of correction**	**Q_o**
None (i.e. as Figure 6b)		7546
Re-calculate A_{21} to correct for loss of semi-rigid uncalibrated lines, which is characterised by B (see Section 4.3)	B=0.92	7554

The Type A uncertainty contribution is estimated from the standard deviation of repeated measurements (Figure 14). If the IFBW of the VNA is set to 100 Hz, it has the value of 0.05 % for this measurement. The full list of Type B uncertainty contributions is given in Table 14. A correction for attenuation in the uncalibrated-line sections between the connectors of the resonator (Figures 1 and 17) can be applied, but if the attenuation is low and the coupling weak, this is negligible (Table 13).

The measured Q-circle of the quasi-TE01δ mode resonance of an SPDR (Figure 6b) agrees very closely with the circular form that is expected when uncalibrated lines are short. No systematic trend in the magnitude of the residual error r of the fitted S_{21} (equation (21)) vs frequency can be seen (Figure 28). The consistency of measurements of Q_L was assessed by means of three experiments: see Table 2 (which shows calibrated and uncalibrated measurements),

Table 14: Type B uncertainty contributions associated with Q_o for an SPDR (Figure 17) measured by transmission at 4 GHz.
The SPDR was empty (i.e. there was no specimen to be measured). Q_L was fitted to the S_{21} Q-circle shown in Figure 6b by using NLQFIT6.
Q_o was calculated by using equations (31) and (38), incorporating a small correction for the attenuation in uncalibrated lines.
The Q_o result is 7554 (Table 13).

Source of uncertainty	**Value of uncertainty**	**Assumed probability distribution**	***Uncertainty component of fitted Q_o**
Effect of VNA non-linearity on Q_o (for VNA power level 0 dBm). Upper limit estimated from Table 10.	4/7430 × 100%	Rectangular (divisor $\sqrt{3}$)	$0.05\% \times Q_o$
Contribution estimated from checks on the consistency of measurements shown in Tables 2, 5 & 9.	9/7537 ×100%	Normal (divisor 1)	$0.1\% \times Q_o$
Uncertainty associated with phase delay $\Delta\phi_W$ of uncalibrated lines given by equation (9). The Q_L contribution is estimated from Figure 10 making allowance for the total length of cable (1.5 metres) and noting that $Q_o \approx Q_L$. Assumes reference planes for uncalibrated VNA in locality of the front panel.	$\Delta\phi_w$ is 0.5°	Normal (divisor 1)	$0.01\% \times Q_o$
Uncertainty associated with normalisation factor A_{21} that is obtained from a "thru" measurement. $A_{21} = \lvert S_{21}\rvert^{-1}B^{-1} = 1/(0.874 \times 0.92)$ =1.24.	$A_{21} \times 1\%$	Normal (divisor 1)	$0.01\% \times Q_o$
Unequal settings of Port 1 and Port 2 coupling factors (calculation of Q_o using equation (38) assumes they are equal – see Section 4.5). The associated uncertainty in Q_o is estimated from Figure 19.	⌀ of S_{11} and S_{22} Q-circles differs by 0.002 Units	Normal (divisor 1)	$0.05\% \times Q_o$
Model uncertainty (see Section 5.1).			$(0.5\% \times Q_o) + 1.0$
Combined standard uncertainty, u_B			$(0.52\% \times Q_o) + 1.0$

*Calculated from the previous two columns.

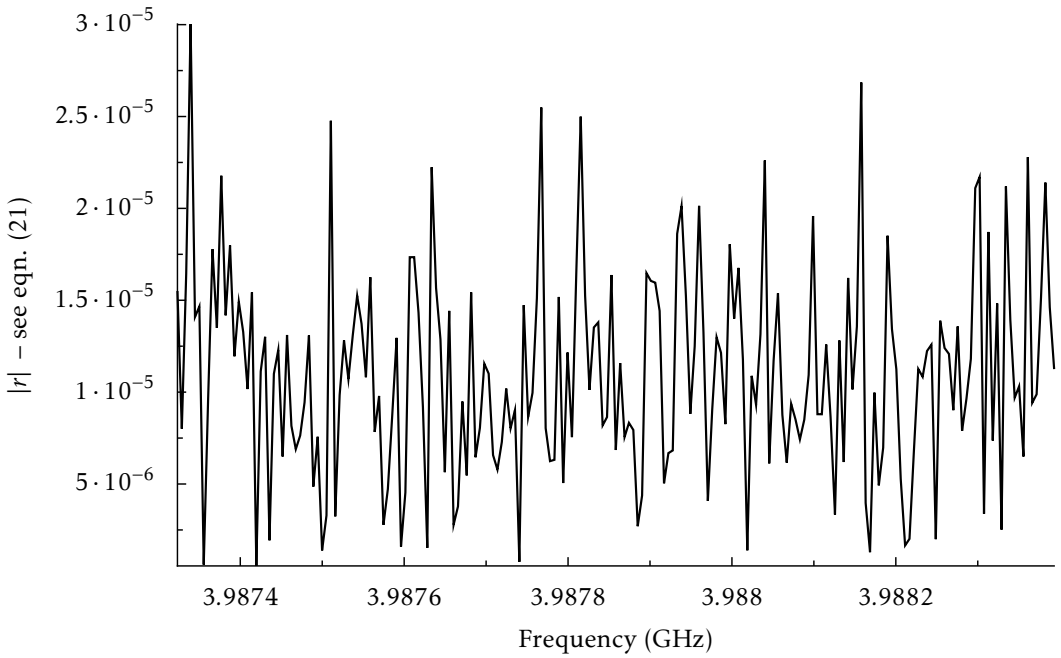

Figure 28: Magnitude of the residual error $|r|$ given by equation (21) plotted as a function of frequency for a fit to the SPDR measurement shown in Figure 6b. The data shows random noise but no systematic trend, which implies that Type B uncertainty associated with Q_L fitted to the frequency-domain model, equation (1), is low.

.

Table 5 (which shows measurements with three different VNAs), and Table 9 (which shows Q-factors fitted to Lower 35 % and Upper 35 % Q-circles). For the resonance shown in Figure 6b, the RLC model is a very good fit. Such tests, however, do not provide a complete view of the model uncertainty. The effect of mismatches associated with uncoupled lines, for example, is not necessarily evident in the shape of Q-circles (Figure 13). The three experiments suggest that the standard uncertainty associated with Q_L is 0.1 %, but this could be an underestimate. Determination of the Q_o requires a further calculation that is based on assumptions regarding the effect of impedances associated with uncalibrated lines and couplings.

There are too many unknowns to allow a mathematically rigorous evaluation of uncertainty, so an estimate has to be made. It is usually best to make such estimates conservatively, i.e. so that they are more likely to be too large than too small. For well-shaped resonances measured by transmission with weak coupling, the author normally evaluates the standard uncertainty of Q_o associated with the model as $(0.5\,\% \times Q_o) + 1.0$. The rationale for the added 1.0 is that the uncertainty when $Q_o \lesssim 300$ is proportionally greater because mismatches and leakage are less likely be constant over a broad resonance.

6 Measurement of Dielectric Loss Angle

Figure 29 shows cavities and dielectric resonators that are used for measuring the permittivity and loss angle[13] of solid disc- or rod-shaped specimens at microwave frequencies in the author's laboratory. Open resonators [30] are used in the range 10 GHz to above 300 GHz, and hybrid cavities [4] in the range 300 MHz to 3 GHz. The other resonators shown are used typically at frequencies in the range 1 GHz to 10 GHz. References [4, 89, 90] are among the many publications that describe resonance methods. Resonant techniques for measurement at elevated temperatures [91, 92] and cryogenic temperatures [73, 93] have been developed. Reference [4] considers metrological aspects of dielectric measurements; namely *traceability*, *uncertainty* and *confidence*. The Q-factor of cavities (if limited by *skin-effect* losses) increases with the square root of frequency (Section 6.1), so the resolution for δ measurements should improve as the frequency is increased. At low frequencies, however, signal-to-noise ratio and stability of VNA measurements are improved, so smaller Q-factor changes may be observable. There are high Q-factor millimetre-wave (open-resonator [30]) and low Q-factor MHz (Hartshorn and Ward [69]) methods that can resolve loss angles below 10 μrad.

The Hartshorn and Ward method can be used to measure the loss angle of sheets of low-loss material at frequencies between 1 MHz and 100 MHz [69, 80, 94, 95]. Specimens are placed in a dielectric "test-set" (essentially a parallel plate capacitor with a micrometer for precise adjustment). A high-stability shielded coil, such as the one shown in Figure 30, is used to make a resonant LC circuit. Historically, a Q-meter was used to measure Q-factor [80]. This uses a series resonant configuration, and a coupling transformer to give very low source impedance. If a parallel resonance configuration is adopted (Figure 31) then a modern VNA can be used for Q-factor measurement, which improves precision as well as being more convenient [69]. A resolution for δ of below 10 µrad is obtainable, which is a significant improvement on non-resonant admittance cell methods [4] (which are best suited to materials for which δ >100 µrad – see the discussion in reference [80]).

The loss angle δ can be determined from the measured the change in $1/Q_o$ caused by the specimen.[14] If it is assumed that losses due to the skin effect, radiation, etc. are not changed between the two measurements then

$$F_f \tan\delta = \frac{1}{Q_s} - \frac{1}{Q_e} \tag{46}$$

where

$$F_f \equiv F_f(x_1, x_2, \ldots).$$

In the above equation unloaded Q-factors are Q_s (specimen in resonator) and Q_e (resonator empty) and F_f is the *filling factor*. F_f is a function of data (x_1, x_2, …) such as the dimensions of the specimen and resonator. For a cavity, F_f would normally be calculated by using an electromagnetic model. For more discussion of filling factors, see reference [4].

[13] The dielectric loss of low loss materials may conveniently be expressed by the loss angle (δ) in units of micro-radians (μrad), which is related to loss tangent by $\delta \approx \tan\delta \times 10^6 \mu$rad.

[14] This does not apply to Hakki-Coleman or dielectric resonators as Q-factor can only be measured with the specimen *in situ*. The conductivity of the plates/cavity can be estimated from measurements on very low loss reference materials and then corrected for by incorporating it in the modal-analysis calculation.

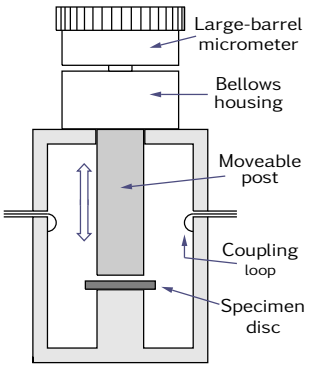

(a): Hybrid cavity

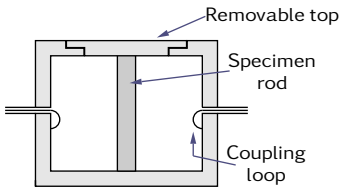

(b): TM-mode cavity

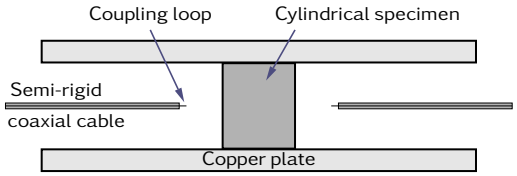

(c): Hakki-Coleman resonator

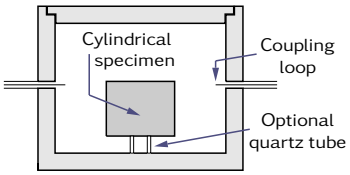

(d): Dielectric resonator

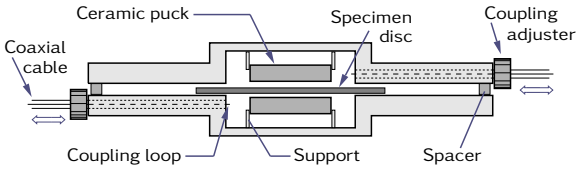

(e): Split-post dielectric resonator

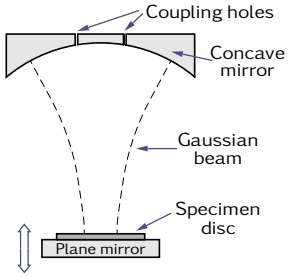

(f): Quasioptical plano-concave open resonator

Figure 29: Resonators for measuring ϵ' and δ. For the resonators shown in diagrams (c), (d) and (e), coupling loops are orientated perpendicular to the paper to excite TE modes.

Figure 30: Standard coil inductor.

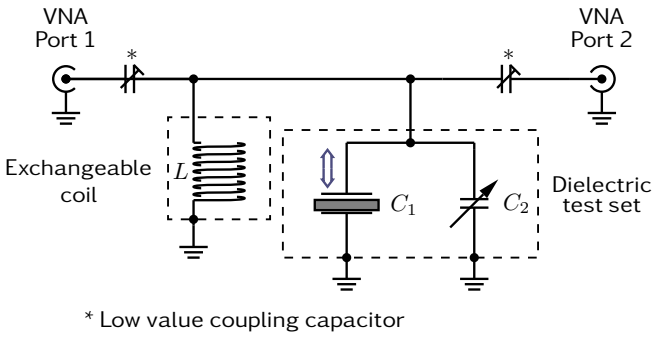

Figure 31: An LC resonator for measuring ϵ' and δ by using the Hartshorn and Ward method [69].

6.1 Skin effect losses

For cavities, it is found that Q_o is proportional to $\sqrt{f}$ if there are no other losses (see Figure 33 and reference [96]). A simple explanation of this can be obtained by making an analogy with a resonant circuit that has a lossy coil inductor (Figure 32). The cavity Q-factor is related to the *RF sheet resistance*[15] (R_s) of the cavity surface by $Q_o = 2\pi f L/R_s$ but, for a normal conductor, R_s is proportional to $\sqrt{f}$ on account of the skin effect [97]. Therefore, Q_o must be proportional to $\sqrt{f}$. Measurements of loss angle for low loss specimens in a cavity of fixed dimensions are subject to error because R_s becomes lower when a specimen is inserted as the resonant frequency is reduced. To improve accuracy, the measured Q_e can be corrected to account for the frequency change.

6.2 The equivalent-length method

The permittivity and loss angle of a laminar specimen can be measured by the equivalent-length method [4] if the resonator is tuned by adjusting its length with a micrometer. The method entails measuring the length-change required to restore a particular resonance after the specimen has been removed. Skin effect losses should change negligibly between the two measurements as the frequency is unchanged, which improves the resolution of measurements of δ. The equivalent-length method can be applied to open resonators to enable precise measurement of ϵ' and δ of very low loss materials [30]. For experiments that use a parallel-plate-electrode geometry (e.g. hybrid cavity and Hartshorn and Ward methods [69]), a technique that is often used is to measure specimens with a small air gap between them and the top electrode [4]. This technique, which has become known as the Lynch method [98], reduces uncertainty in measured ϵ' and δ that is associated with the specimen geometry (flatness & parallelism of faces) and the test-set mechanism (micrometer backlash, parallelism of electrodes). The equivalent-length method can also be applied in non-resonant admittance cell techniques [4] for measuring ϵ' and δ.

6.3 Evaluation of the uncertainty of measurements of loss angle

Evaluation of uncertainty associated with the loss angle δ requires evaluation of the following contributions:

- Type A uncertainty associated with measurements of Q_o. This can be evaluated as the standard deviation of repeated measurements (Figure 14).
- Type B uncertainty associated with measurements of Q_o. Table 14 shows that for a typical measurement the model uncertainty is the dominant term. Correlations between these contributions for measurements with and without the specimen must be considered.
- The resolution: There is a limit to ability to measure δ for very low loss materials because: (a) Inserting a specimen into a cavity may cause unaccounted-for changes to the loss in its walls as a result of the perturbation to the fields (e.g. if resonant current flows across oxidised contact planes). (b) If a modal field decomposition, finite difference or finite element method is used to model the fields in the resonator, the resolution will limited by the finite number of modes or discretised elements. (c) In methods that use electrodes, such as the Hartshorn and Ward method, sources of error such as the finite conductivity of electrodes may not be fully accounted for. (d) Skin depth losses in cavity

[15] Also known as the surface resistivity [97] R_s = (skin depth × conductivity)$^{-1}$

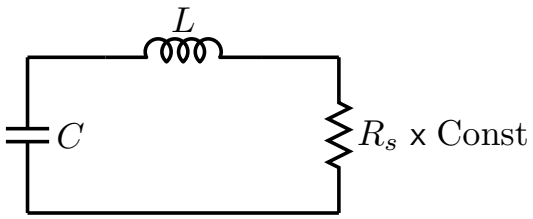

Figure 32: Equivalent circuit representation of a cavity. R_s represents the sheet resistance of the cavity walls. The constant of proportionality depends on the resonant mode and the cavity geometry.

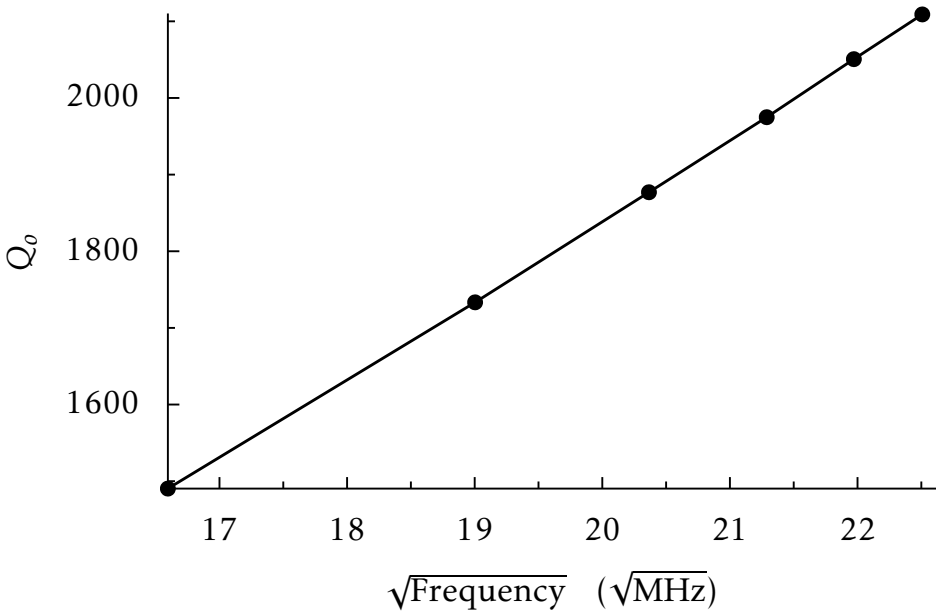

Figure 33: Measurements of Q-factor plotted against the square root of resonant frequency for an empty tuneable hybrid cavity (Measurements by G. J. Hill, NPL).

walls depend on frequency. (e) Open structures, such as Hakki-Coleman resonators and open resonators, may radiate causing power loss. (f) Uncertainties in data for resonator components, such as the ceramic pucks of an SPDR (Figure 29e) [51], cause uncertainty in measurements of both ϵ' and δ.

The resolution can be etimated from measurements on very low loss materials, such as (YAG ϵ'=10.6, δ ~10 µrad at frequency 10 GHz).

- Uncertainty contributions associated with dimensions of the specimen and resonator.

A comprehensive evaluation of the uncertainty of the loss angle would require the evaluation of the covariance matrix [76] of the type B uncertainties associated with the measurements of the unloaded Q-factors Q_s and Q_e. The methods described in Section 5 allow evaluation of the Type B uncertainties associated with the measured Q_s and Q_e on the assumption that they are independent quantities; however no information regarding the correlations [76] between them (i.e. the off-diagonal elements of the uncertainty covariance matrix) is obtained. It is almost certain that there are significant correlations between errors in measurements of Q_s and Q_e. Not accounting for these will lead to inaccurate evaluations of uncertainty. There is, however, one additional piece of information that can be used; whether the difference between Q_s and Q_e is large or small (which depends on the specimen loss). If the difference is large then it can be plausibly argued that the systematic errors in the measurements of Q_s and Q_e are practically independent, which gives a sensible upper limit to the uncertainty (the possibility that they are anti-correlated is not considered as this is unlikely). If it is small, the measurement errors of these two measurements are almost the same, and a lower limit can be evaluated. This would typically be used for the case that Q_s is only fractionally smaller than Q_e (by perhaps $\lesssim$10 %).

To make the evaluation of uncertainty easier to describe, equation (46) can be written as a function, $\mathcal{D}$, which is given by

$$\delta = \mathcal{D}(Q_s, Q_e, x_1, x_2, \ldots). \tag{47}$$

Evaluation of upper limit: assumes that errors in Q_s and Q_e measurements are uncorrelated

The combined standard uncertainty of a measurement of the loss angle (u_δ) is given by the quadrature sum:

$$u_\delta = \sqrt{\left(\frac{\partial \mathcal{D}}{\partial Q_s}\right)^2 \left(\boxed{u_A^2 + u_B^2}_{\mathrm{s}}\right) + \left(\frac{\partial \mathcal{D}}{\partial Q_e}\right)^2 \left(\boxed{u_A^2 + u_B^2}_{\mathrm{e}}\right) + {u_r}^2 + \sum_x \left(\frac{\partial \mathcal{D}}{\partial x} u_x\right)^2} \tag{48}$$

where u_A and u_B are Type A and Type B standard uncertainty contributions associated with the Q-factor measurements (see Table 14). Note that boxes are used in the above equation to show that these quantities are defined separately for the “specimen” (s) and “empty” (e) measurements. The u_r term represents the resolution for loss measurement, as discussed above. The u_x terms represent the uncertainty components associated with other required data (x_1, x_2, ...), such as the thickness of specimens.

Evaluation of lower limit: assumes that errors in Q_s and Q_e measurements are highly correlated

The Type B uncertainty components associated with Q_s and Q_e are similar if $Q_s \approx Q_e$. The uncertainty of the loss angle is therefore reduced. Suppose that the quantity q is used to represent an error that is identical for Q_s and Q_e measurements. If q is given the value of the Type B uncertainty of the Q-factor measurements, the corresponding standard uncertainty in δ can be evaluated by using a modified version of equation (48),

$$u_\delta = \sqrt{u_c^2 + \left(\frac{\partial \mathcal{D}}{\partial Q_s}\right)^2 \left(\boxed{u_A^2}_{\mathrm{s}}\right) + \left(\frac{\partial \mathcal{D}}{\partial Q_e}\right)^2 \left(\boxed{u_A^2}_{\mathrm{e}}\right) + {u_r}^2 + \sum_x \left(\frac{\partial \mathcal{D}}{\partial x} u_x\right)^2} \tag{49}$$

where

$$u_c = \left| \mathcal{D}(Q_s + q, Q_e + q, x_1, x_2, \ldots) \; - \; \mathcal{D}(Q_s, Q_e, x_1, x_2, \ldots) \right|. \tag{50}$$

The quantity u_c can also be written as

$$u_c = \frac{1}{F_f} \left| \left(\frac{1}{Q_s + q} - \frac{1}{Q_e + q} \right) - \left(\frac{1}{Q_s} - \frac{1}{Q_e} \right) \right|. \tag{51}$$

The value of q can be taken to be $\boxed{u_B}_{\mathrm{e}}$, i.e. the Type B standard uncertainty for Q_e.

Comparison of upper and lower limits

To gain an idea of how the upper and lower limits compare, suppose that:

$\boxed{u_B^2}_{\mathrm{s}} = \boxed{u_B^2}_{\mathrm{e}} = 10^2 = q^2$, $Q_e = 1000$ and $Q_s = 900$.

The loss angle is calculated as δ = 111 µrad by using equation (46) if F_f is unity. If only the Type B Q-factor uncertainty components are considered, equation (48) gives u_δ = 16 µrad, and equation (49) gives u_δ = 2 µrad. The lower limit gives a smaller and more realistic evaluation of uncertainty when Q_s is only fractionally lower than Q_e. This occurs when low loss materials are measured in a resonator that has low Q-factor [69].

6.4 Example – evaluation of the uncertainty of SPDR measurements on a rexolite disc

Table 15 presents measurements of resonant frequency, Q-factor of a disc of rexolite co-polymer that were obtained with the 4 GHz SPDR shown in Figure 17. The measured thickness T of the specimen and its uncertainty (obtained by using a micrometer) are also shown in Table 15. From this data, it is determined that ϵ'=2.54 and δ=1242 µrad by using software provided by the manufacturer of the SPDR. The manufacturer's software can be called from inside a Python function, here represented by SPDR4:

```
# Call function to calculate permittivity and loss angle
Eps, LossAng = SPDR4(F_Empty, Q0_Empty, F_Spec, Q0_Spec, T)
```

Evaluations of the uncertainty contributions associated with the measurements are also shown in Table 15. The Type A uncertainty contributions associated with Q-factor measurements are standard deviations of repeated measurements. Sensitivity coefficients [99] can be estimated

Table 15: List of uncertainty contributions for measurements of ϵ' and δ obtained by using a 4 GHz SPDR for a rexolite specimen. Q-factors and resonant frequencies were fitted to complex transmission coefficients by using NLQFIT6 (see Figure 6). Weak coupling was used. The VNA was an Agilent 8753ES with settings: 201 points, power 0 dBm, IFBW 100 Hz. The measured material properties are ϵ' = 2.54 and δ = 1242 µrad.

Measured quantity	**Value**	**Standard uncertainty associated with measured quantity**	
		Type A	**Type B**
Q_o(empty) [Q_e]	7593	2.0	†(0.5 % × Q_e) + 1.0
Q_o(specimen) [Q_s]	5541	2.0	†(0.5 % × Q_s) + 1.0
Specimen thickness [mm]	1.795	*0.005	‡0.00058
f_{spec} [GHz]	3.93727105	Type A and Type B uncertainties associated with measurement of frequency are negligible in this experiment	
f_{empty} [GHz]	3.98825300		
Resolution of measured δ associated with filling factor [51] calculated with computational model			♦20 µrad
Resolution of measured ϵ' associated with computational model (here calculated from dimensions of the ceramic pucks in the SPDR [51])			0.075% × ϵ'

† Combined Type B uncertainty components from Table 14.

* The thickness variation across the specimen, assumed to be the standard deviation σ_{N-1} of thickness measurements made with micrometer at 7 or more locations.

‡ Standard uncertainty ($0.001/\sqrt{3}$) estimated from the specification of the micrometer – see reference [99].

♦ Resolution of δ can be assessed either by modelling (as is the case here) or experimentally from measurements on very low loss materials such as single crystals.

numerically. This enables an evaluation of uncertainty to be performed by using either equation (48) or equation (49). If the standard uncertainty associated with the measured thickness is T_unc, the uncertainty component in δ associated with uncertainty in the measured thickness can be calculated with the following lines of Python computer code:

```
# Evaluation of uncertainty component associated with specimen
# thickness by first-order numerical differentiation
Eps2, LossAng2 = SPDR4(F_Empty, Q0_Empty, F_Spec, Q0_Spec, T+T_Step)
c = abs(LossAng2-LossAng)/T_Step # unsigned sensitivity coefficient
LossAng_unc_T = c*T_unc
```

where T_Step is an appropriate "step" used in a first-order estimation of the sensitivity coefficient. The same technique is also applied to obtain the uncertainties in ϵ'. As the relation between T and the calculated ϵ' and δ will not be linear, it is necessary to use a small value for T_Step. However, if T_Step is too small, computational uncertainty associated with the

function SPDR4 could cause significant loss of precision [99]. The approach usually adopted by the author is to use T_unc as the "step".

```
Eps2, LossAng2 = SPDR4(F_Empty, Q0_Empty, F_Spec, Q0_Spec, T+T_Unc)
LossAng_unc_T = abs(LossAng2-LossAng)
```

The standard uncertainty associated with the permittivity is found to be $u(\epsilon')$=0.01, based on the uncertainty of the thickness measurement and a minimum resolution associated with the computational model.

There are four Q-factor uncertainty contributions (Type A and Type B contributions for both "empty" and "specimen" measurements). Upper and lower limits of the combined standard uncertainty associated with δ are calculated as follows:

Upper limit of $u(\delta)$*:* The uncertainty upper limit can be calculated by using equation (48) as $u(\delta)$=34 µrad on the assumption that errors in the input quantities are uncorrelated. The uncertainty components are shown in Table 16a.

Lower limit of $u(\delta)$*:* In this scenario, the "empty" and "specimen" Q-factor measurements (Table 15) are assumed to have highly correlated systematic errors and uncorrelated random errors. Errors associated with other input quantities are assumed to be uncorrelated. The uncertainty lower limit is evaluated by using equation (49). The value of u_c can be calculated with a few lines of Python computer code:

```
Eps2, LossAng2 = SPDR4(F_Empty, Q0_Empty+Q0_Unc_TypeB, F_Spec,
                       Q0_Spec+Q0_Unc_TypeB, T)

LossAng_unc_Q_TypeB = abs(LossAng2-LossAng)
```

Q_Unc_TypeB (= 0.5x7593/100 + 1.0) is the larger of the "empty" and "specimen" Q-factor uncertainty components. LossAng_unc_Q_TypeB = u_c and Q0_Unc_TypeB = q in the nomenclature used in equations (49) and (51). It is found that the combined standard uncertainty is $u(\delta)$ = 25 µrad. The uncertainty components are shown in Table 16b.

For the measurement on rexolite, Q0_Spec (Q_s) and Q0_Empty (Q_e) differ significantly, so the upper-limit of uncertainty evaluated in Table 16a would normally be selected. The expanded combined uncertainty (Section 5) can then be calculated.

6.5 Testing evaluations of the uncertainty of the loss angle

Measurement comparisons [100] with different resonator geometries and with different specimen sizes are needed to gain understanding of Type B uncertainties and helps to improve confidence in measurements. A good example of a comparative test is provided by reference [51], in which measurements in an SPDR on a varying number of stacked specimens are compared. The uncertainty of the real part of permittivity in many experiments is determined largely by dimensional contributions which are easily assessed, so uncertainty evaluations are generally reliable. Experience has shown that the uncertainty associated with measurement of loss angle is easily under-estimated as contributions associated with computational assumptions (e.g. when using a perturbation or a substitution method) and Q-factor measurement are not easily assessed.

Table 16: Uncertainty components for a measurement of δ obtained by using a 4 GHz SPDR for a rexolite specimen (calculated from data given in Table 15).

(a) Upper limit obtained by using equation (48): It is assumed that there are no correlations associated with errors in the input quantities.

Components of $u(\delta)$ in µrad				**Combined standard uncertainty $u(\delta)$ in** µrad
Resolution u_r	Type B associated with Q_e $\left\lvert\frac{\partial \mathcal{D}}{\partial Q_e}\right\rvert \boxed{u_B}_{\mathrm{e}}$	Type B associated with Q_s $\left\lvert\frac{\partial \mathcal{D}}{\partial Q_s}\right\rvert \boxed{u_B}_{\mathrm{s}}$	All other components combined	
20	15	22	2	34

(b) Lower limit obtained by using equation (49): Q_s and Q_e are assumed to have highly correlated systematic errors and uncorrelated random errors. It is aasumed that there are no correlations associated with errors in other input quantities.

Components of $u(\delta)$ in µrad			**Combined standard uncertainty $u(\delta)$ in** µrad
Resolution u_r	Q-factor Type B component u_c	All other components combined	
20	14	2	25

7 Conclusion

Experimental procedures for obtaining Q-factor and resonant frequency from measurements of complex S-parameter data (transmission or reflection) acquired with a Vector Network Analyser (VNA) have been described and compared. The VNA cursor/marker facility can be used for manual measurement by using the traditional "3 dB point" method [4, 49] by transmission, or Kwok and Liang's method [61] by reflection. The main focus of this report, however, has been on techniques that numerically fit a mathematical model to swept-frequency complex S-parameter data, as they offer better precision and are more convenient to use in computer-controlled experiments.

Transmission and reflection methods have been compared (Section 3.4). It is found that the transmission method is usually the best option, provided that weak coupling is used (which minimises perturbation of the resonance). Moreover, the VNA can be used uncalibrated without significant loss of precision (Table 2). Vector algorithms that fit Q-factor to swept complex transmission coefficients generally provide better precision than scalar algorithms that fit to their magnitudes [23, 24]. In contrast, the reflection method requires that the VNA is calibrated to give the best accuracy – although at long wavelengths (frequency $\lesssim$100 MHz) uncalibrated measurements may suffice. Strong coupling is recommended for reflection methods (0.1 < Q-circle diameter < 1.0). The effect of uncalibrated lines on determinations of Q-factor from vector reflection data is very significant (much greater than for typical measurements by transmission), and so it is usually advisable to make the line length a fitted quantity. The scalar reflection technique brings some extra complexity as calculation of unloaded Q-factor requires a separate measurement to determine whether the resonator is undercoupled or overcoupled.

An original vector fitting algorithm (NLQFIT) has been discussed in detail, and code-listings and implementation details provided. NLQFIT uses a two-stage process that gives fast and reliable convergence on a solution and is therefore well suited to automated measurements. The length of uncalibrated lines can be included as a fitted quantity. Its application to measurement of Q-factor by transmission and by reflection is demonstrated in this report. Experiments have shown that convergence to a solution is often possible when the sweep span is much greater than the width of the resonance provided that the resonant peak is within the swept range. Measurements of resonant frequency and Q-factor obtained by fitting with NLQFIT have been demonstrated to have high repeatability, so it is possible to use it to observe small changes of resonant frequency and Q-factor. A typical application that would require such observations is measurement of complex permittivity by perturbation methods [4, 89, 90, 101]. These include microfluidic [63, 64] and capillary-tube systems [65] that can be used to measure polar liquids that have high loss in the microwave range, and resonant microwave microscopes [102–104] for dielectric imaging of solid materials. Q-factor changes as small as 1 part in 10^4 can be resolved for LC resonators that have low Q-factor (typically 200–300). This enables measurement of the loss angle of very low loss materials at MHz frequencies [69, 80, 94].

To demonstrate the reliability of the NLQFIT algorithm and the procedures described, a number of tests were performed. These included comparisons of simultaneous reflection and transmission measurements on a two-port resonator for a range of coupling factors. Q-factors fitted by NLQFIT and two programs written by D. Kajfez, QZERO (vector fitting) [19] and SCALARQ (scalar fitting) [34], were found to be in good agreement for a number of sets of data. The measurement models that are used by all of these algorithms are approximations based in lumped-component equivalent circuits. The shapes of resonant peaks and Q-circles often deviate from those predicted by these models, which is indicative of model uncertainty. Some possible strategies to inform evaluations of model uncertainty have been outlined. Evaluations of other uncertainty components are also presented. Most resonance methods for measuring the loss angle of low loss dielectric materials require measurements of Q-factor with and without specimens. A more rigorous evaluation of the uncertainty of measurements of loss angle would require covariances associated with the two Q-factor measurements to be considered. The methods available for obtaining estimates of model uncertainty provide no covariance data; nevertheless upper and lower limits of the uncertainty associated with measurements of loss angle can be evaluated.

8 Acknowledgements

The algorithms described in this report were developed over a number of years under projects funded by the UK Government's Department for Business, Energy and Industrial Strategy. Some aspects were further developed under the project "Electromagnetic Materials Measurements for Industrial Applications (EMINDA)". This was a 3 year project under the European Metrology Research Programme (EMRP) under Grant Agreement No. 217257. The EMRP is jointly funded by the EMRP participating countries within EURAMET and the European Union. The author would like to thank the following NPL colleagues: R. N. Clarke for his review of the manuscript. G. J. Hill, J. Howes and I. Instone for detailed discussions on various technical aspects. Z. Ali and T. Lindstrom for describing their cryogenic measurements and providing data. The author would also like to thank S. M. Hanham (University of Birmingham) for performing independent tests on the NLQFIT algorithm.

References

[1] D. M. Pozar. *Microwave engineering; 4th ed.* Hoboken, NJ: Wiley, 2012.

[2] M. Sucher and J. Fox. *Handbook of microwave measurements; Vol. 2, 3rd Ed.* New York: Polytechnic Press, 1963.

[3] E. L. Ginzton. *Microwave measurements*. International series in pure and applied physics. New York: McGraw-Hill, 1957.

[4] R. N. Clarke (Ed.) *Guide to the characterisation of dielectric materials at RF and microwave frequencies*. Tech. rep. The Institute of Measurement, Control, and The National Physical Laboratory, London, 2003. URL: http://eprintspublications.npl.co.uk/id/eprint/2905/.

[5] *S-parameter design, Application Note (Keysight 5952-1087 or Agilent AN-154)*.

[6] I. J. Bahl. *Lumped elements for RF and microwave circuits*. Artech House microwave library. Artech House, 2003. ISBN: 9781580536615.

[7] C. Massin et al. "High-Q factor RF planar microcoils for micro-scale NMR spectroscopy". In: *Sensors and Actuators A: Physical* 97–98 (Apr. 2002), pp. 280–288. URL: https://doi.org/10.1016/s0924-4247(01)00847-0.

[8] R. R. A. Syms et al. "MEMS Helmholtz coils for magnetic resonance imaging". In: *Journal of Micromechanics and Microengineering* 15.7 (June 2005), S1–S9. URL: https://doi.org/10.1088/0960-1317/15/7/001.

[9] A. Kurs et al. "Wireless power transfer via strongly coupled magnetic resonances". In: *Science* 317.5834 (July 2007), pp. 83–86. URL: https://doi.org/10.1126/science.1143254.

[10] M. Pinuela et al. "Maximizing DC-to-load efficiency for inductive power transfer". In: *IEEE Transactions on Power Electronics* 28.5 (May 2013), pp. 2437–2447. URL: https://doi.org/10.1109/tpel.2012.2215887.

[11] *"Exploring the architectures of network analzers", Application Note (Keysight 5965-7708 or Agilent AN-1287-2)*.

[12] J. Tatum. *Combination of profiles [Internet]. University of Victoria; 2020 [cited 2021 Jan 1].* URL: https://phys.libretexts.org/Bookshelves/Astronomy__Cosmology/Book%3A_Stellar_Atmospheres_(Tatum)/10%3A_Line_Profiles/10.04%3A_Combination_of_Profiles.

[13] N. S. Azaryan et al. "Measurement of high values of Q-factor of 1.3 GHz superconducting cavity of TESLA-type". In: *Universal Journal of Materials Science* 6.1 (Jan. 2018), pp. 1–7. URL: https://doi.org/10.13189/ujms.2018.060101.

[14] Y. Komachi and S. Tanaka. "An automatic Q-meter using the damped oscillation of a resonant circuit excited by a keyed signal". In: *Journal of Physics E: Scientific Instruments* 7.11 (Nov. 1974), pp. 905–909. URL: https://doi.org/10.1088/0022-3735/7/11/014.

[15] B. Gyüre et al. “A time domain based method for the accurate measurement of Q-factor and resonance frequency of microwave resonators”. In: *Review of Scientific Instruments* 86.9 (Sept. 2015), p. 094702. URL: https://doi.org/10.1063/1.4929865.

[16] M. Rodahl et al. “Quartz crystal microbalance setup for frequency and Q-factor measurements in gaseous and liquid environments”. In: *Review of Scientific Instruments* 66.7 (July 1995), pp. 3924–3930. URL: https://doi.org/10.1063/1.1145396.

[17] K. J. Coakley et al. “Estimation of Q-factors and resonant frequencies”. In: *IEEE Transactions on Microwave Theory and Techniques* 51.3 (Mar. 2003), pp. 862–868. URL: https://doi.org/10.1109/tmtt.2003.808578.

[18] D. Kajfez. *Q-factor*. Oxford MS.: Vector Fields, 1994.

[19] D. Kajfez. “Linear fractional curve fitting for measurement of high Q factors”. In: *IEEE Transactions on Microwave Theory and Techniques* 42.7 (July 1994), pp. 1149–1153. URL: https://doi.org/10.1109/22.299749.

[20] J. W. Brown and R. V. Churchill. *Complex variables and applications*. Churchill-Brown series. McGraw-Hill, 1996. ISBN: 9780071140652. URL: https://books.google.co.uk/books?id=DzePPwAACAAJ.

[21] D. Kajfez and E. J. Hwan. “Q-Factor measurement with network analyzer”. In: *IEEE Transactions on Microwave Theory and Techniques* 32.7 (July 1984), pp. 666–670. URL: https://doi.org/10.1109/tmtt.1984.1132751.

[22] D. W. P. Thomas et al. “Practical measure of cable coupling”. In: *2009 International Conference on Electromagnetics in Advanced Applications*. IEEE, Sept. 2009. URL: https://doi.org/10.1109/iceaa.2009.5297315.

[23] P. G. Bartley and S. B. Begley. “Quality factor determination of resonant structures”. In: *2006 IEEE Instrumentation and Measurement Technology Conference Proceedings*. IEEE, Apr. 2006. URL: https://doi.org/10.1109/imtc.2006.328435.

[24] P. J. Petersan and S. M. Anlage. “Measurement of resonant frequency and quality factor of microwave resonators: Comparison of methods”. In: *Journal of Applied Physics* 84.6 (Sept. 1998), pp. 3392–3402. URL: https://doi.org/10.1063/1.368498.

[25] M. G. Cox and H. M. Jones. *A nonlinear least-squares data fitting problem arising in microwave measurement.* Algorithms for Approximation II. London: Chapman and Hall, 1990, pp. 458–465.

[26] G. Faby and K. Schunemann. “Q-factor measurements of open resonators in the millimeter-wave range including coupling losses”. In: *IEEE Transactions on Instrumentation and Measurement* 48.3 (June 1999), pp. 688–692. URL: https://doi.org/10.1109/19.772197.

[27] R. Inoue et al. “Highly accurate and real-time determination of resonant characteristics: complex linear regression of the transmission coefficient”. In: *IEEE Transactions on Microwave Theory and Techniques* 52.9 (Sept. 2004), pp. 2163–2168. URL: https://doi.org/10.1109/tmtt.2004.834183.

[28] J. Gao. “The physics of superconducting microwave resonators”. PhD thesis. California Institute of Technology, 2008. URL: https://resolver.caltech.edu/CaltechETD:etd-06092008-235549.

[29] S. Probst et al. “Efficient and robust analysis of complex scattering data under noise in microwave resonators”. In: *Review of Scientific Instruments* 86.2 (Feb. 2015), p. 024706. URL: https://doi.org/10.1063/1.4907935.

[30] J. R. Birch and R. N. Clarke. “Dielectric and optical measurements from 30 to 1000 GHz”. In: *Radio and Electronic Engineer* 52.11-12 (1982), p. 565. URL: https://doi.org/10.1049/ree.1982.0082.

[31] K. Naeli and O. Brand. “An iterative curve fitting method for accurate calculation of quality factors in resonators”. In: *Review of Scientific Instruments* 80.4 (Apr. 2009), p. 045105. URL: https://doi.org/10.1063/1.3115209.

[32] M. P. Robinson and J. Clegg. “Improved determination of Q-factor and resonant frequency by a quadratic curve-fitting method”. In: *IEEE Transactions on Electromagnetic Compatibility* 47.2 (May 2005), pp. 399–402. URL: https://doi.org/10.1109/temc.2005.847411.

[33] A. O. Niedermayer et al. “Methods for the robust measurement of the resonant frequency and quality factor of significantly damped resonating devices”. In: *Measurement Science and Technology* 23.8 (July 2012), p. 085107. URL: https://doi.org/10.1088/0957-0233/23/8/085107.

[34] D. Kajfez. “Q-factor measurement with a scalar network analyser”. In: *IEE Proceedings - Microwaves, Antennas and Propagation* 142.5 (1995), p. 369. URL: https://doi.org/10.1049/ip-map:19952142.

[35] Y. Kato and M. Horibe. “Comparison of calculation techniques for Q-factor determination of resonant structures based on influence of VNA measurement Uncertainty”. In: *IEICE Transactions on Electronics* E97.C.6 (2014), pp. 575–582. URL: https://doi.org/10.1587/transele.e97.c.575.

[36] T. Miura. “A proposal for standard to compare Q-factor evaluation accuracy of microwave resonator”. In: *2006 IEEE MTT-S International Microwave Symposium Digest*. IEEE, 2006. URL: https://doi.org/10.1109/mwsym.2006.249819.

[37] E. Kamenetskii, A. Sadreev, and A. Miroshnichenko, eds. *Fano Resonances in Optics and Microwaves*. Springer International Publishing, 2018. URL: https://doi.org/10.1007/978-3-319-99731-5.

[38] Y. S. Joe, A. M. Satanin, and C. S. Kim. “Classical analogy of Fano resonances”. In: *Physica Scripta* 74.2 (July 2006), pp. 259–266. URL: https://doi.org/10.1088/0031-8949/74/2/020.

[39] S. Satpathy, A. Roy, and A. Mohapatra. “Fano interference in classical oscillators”. In: *European Journal of Physics* 33.4 (May 2012), pp. 863–871. URL: https://doi.org/10.1088/0143-0807/33/4/863.

[40] B. Lv et al. “Analysis and modeling of Fano resonances using equivalent circuit elements”. In: *Scientific Reports* 6.1 (Aug. 2016). URL: https://doi.org/10.1038/srep31884.

[41] E. Lee et al. “Theoretical investigations on microwave Fano resonances in 3D-printable hollow dielectric resonators”. In: *Scientific Reports* 7.1 (Nov. 2017). URL: https://doi.org/10.1038/s41598-017-16501-3.

[42] J. W. Yoon and R. Magnusson. “Fano resonance formula for lossy two-port systems”. In: *Optics Express* 21.15 (July 2013), p. 17751. URL: https://doi.org/10.1364/oe.21.017751.

[43] E. Semouchkina et al. “Sensing based on fano-type resonance response of all-dielectric metamaterials”. In: *Sensors* 15.4 (Apr. 2015), pp. 9344–9359. URL: https://doi.org/10.3390/s150409344.

[44] S. Stassi et al. “Experimental evidence of Fano resonances in nanomechanical resonators”. In: *Scientific Reports* 7.1 (Apr. 2017). URL: https://doi.org/10.1038/s41598-017-01147-y.

[45] T. Nakanishi and M. Kitano. “Storage and retrieval of electromagnetic waves in metamaterials by dynamical control of EIT-like effect”. In: *Fano Resonances in Optics and Microwaves*. Ed. by E. Kamenetskii, A. Sadreev, and A. Miroshnichenko. Springer International Publishing, 2018. Chap. 6, pp. 137–156.

[46] R. Singh et al. “The Fano resonance in symmetry broken terahertz metamaterials”. In: *IEEE Transactions on Terahertz Science and Technology* 3.6 (Nov. 2013), pp. 820–826. URL: https://doi.org/10.1109/tthz.2013.2285498.

[47] C. Meyer. *Matrix Analysis and Applied Linear Algebra*. SIAM, Jan. 2000. URL: https://doi.org/10.1137/1.9780898719512.

[48] K. Leong and J. Mazierska. “Precise measurements of the Q factor of dielectric resonators in the transmission mode-accounting for noise, crosstalk, delay of uncalibrated lines, coupling loss, and coupling reactance”. In: *IEEE Transactions on Microwave Theory and Techniques* 50.9 (Sept. 2002), pp. 2115–2127. URL: https://doi.org/10.1109/tmtt.2002.802324.

[49] D. Kajfez et al. “Uncertainty analysis of the transmission-type measurement of Q-factor”. In: *IEEE Transactions on Microwave Theory and Techniques* 47.3 (Mar. 1999), pp. 367–371. URL: https://doi.org/10.1109/22.750244.

[50] K. Leong et al. “Comparing unloaded Q-factor of a high-Q dielectric resonator measured using the transmission mode and reflection mode methods involving S-parameter circle fitting”. In: *2002 IEEE MTT-S International Microwave Symposium Digest (Cat. No.02CH37278)*. IEEE. URL: https://doi.org/10.1109/mwsym.2002.1012178.

[51] J. Krupka et al. “Uncertainty of complex permittivity measurements by split-post dielectric resonator technique”. In: *Journal of the European Ceramic Society* 21.15 (Jan. 2001), pp. 2673–2676. URL: https://doi.org/10.1016/s0955-2219(01)00343-0.

[52] E. N. Shaforost et al. “High sensitivity microwave characterization of organic molecule solutions of nanoliter volume”. In: *Applied Physics Letters* 94.11 (Mar. 2009), p. 112901. URL: https://doi.org/10.1063/1.3097015.

[53] B. W. Hakki and P. D. Coleman. “A dielectric resonator method of measuring inductive capacities in the millimeter range”. In: *IEEE Transactions on Microwave Theory and Techniques* 8.4 (July 1960), pp. 402–410. URL: https://doi.org/10.1109/tmtt.1960.1124749.

[54] D. Kajfez. “Random and systematic uncertainties of reflection-type Q-factor measurement with network analyzer”. In: *IEEE Transactions on Microwave Theory and Tech-*

niques 51.2 (Feb. 2003), pp. 512–519. URL: https://doi.org/10.1109/tmtt.2002.807831.

[55] P. Wang, L. H. Chua, and D. Mirshekar-Syahkal. "Accurate characterization of low-Q microwave resonator using critical-points method". In: *IEEE Transactions on Microwave Theory and Techniques* 53.1 (Jan. 2005), pp. 349–353. URL: https://doi.org/10.1109/tmtt.2004.839931.

[56] E.-Y. Sun and S.-H. Chao. "Unloaded Q measurement-the critical points method". In: *IEEE Transactions on Microwave Theory and Techniques* 43.8 (1995), pp. 1983–1986. URL: https://doi.org/10.1109/22.402290.

[57] A. Rumiantsev and N. Ridler. "VNA calibration". In: *IEEE Microwave Magazine* 9.3 (June 2008), pp. 86–99. URL: https://doi.org/10.1109/mmm.2008.919925.

[58] J. A. Chodora. *"Automatic calibration of a network analyzer, US Patent 6,147,501,"*. Nov. 2000.

[59] K. Holland and J. Howes. "Improvements to the microwave mixer and power sensor linearity measurement capability at the National Physical Laboratory". In: *IEE Proceedings - Science, Measurement and Technology* 149.6 (Nov. 2002), pp. 329–332. URL: https://doi.org/10.1049/ip-smt:20020639.

[60] J. R. Bray and L. Roy. "Measuring the unloaded, loaded, and external quality factors of one- and two-port resonators using scattering-parameter magnitudes at fractional power levels". In: *IEE Proceedings - Microwaves, Antennas and Propagation* 151.4 (2004), p. 345. URL: https://doi.org/10.1049/ip-map:20040521.

[61] R. S. Kwok and J.-F. Liang. "Characterization of high-Q resonators for microwave filter applications". In: *IEEE Transactions on Microwave Theory and Techniques* 47.1 (1999), pp. 111–114. URL: https://doi.org/10.1109/22.740093.

[62] A. J. Canos Marin et al. "Improvement in the accuracy of dielectric measurement of open-ended coaxial resonators by an enhanced de-embedding of the coupling network". In: *IEEE Transactions on Microwave Theory and Techniques* 61.12 (Dec. 2013), pp. 4636–4645. URL: https://doi.org/10.1109/tmtt.2013.2285359.

[63] T. H. Basey-Fisher et al. "Microwaving blood as a non-destructive technique for haemoglobin measurements on microlitre samples". In: *Advanced Healthcare Materials* 3.4 (Sept. 2013), pp. 536–542. URL: https://doi.org/10.1002/adhm.201300169.

[64] D. J. Rowe et al. "Microfluidic microwave sensor for simultaneous dielectric and magnetic characterization". In: *IEEE Transactions on Microwave Theory and Techniques* 61.1 (Jan. 2013), pp. 234–243. URL: https://doi.org/10.1109/tmtt.2012.2222909.

[65] R. Lang et al. "Accurate measurements of the dielectric constant of seawater at L band". In: *Radio Science* 51.1 (Jan. 2016), pp. 2–24. URL: https://doi.org/10.1002/2015rs005776.

[66] S. Lal and K. K. Pant. "Study of the effect of loop inductance on the RF transmission line to cavity coupling coefficient". In: *Review of Scientific Instruments* 87.8 (Aug. 2016), p. 083308. URL: https://doi.org/10.1063/1.4961578.

[67] W. Xu et al. *Improvement of the Q-factor measurement in RF cavities*. Tech. rep. BNL-98926-2012-TECH. Brookhaven National Laboratory, 2012. URL: https://technotes.bnl.gov/PDF?publicationId=32605.

[68] W. P. Wheless and D. Kajfez. "Experimental characterization of multimode microwave resonators using automated network analyzer". In: *IEEE Transactions on Microwave Theory and Techniques* 35.12 (Dec. 1987), pp. 1263–1270. URL: https://doi.org/10.1109/tmtt.1987.1133846.

[69] A. P. Gregory, G. J. Hill, and M. A. Barnett. "Low loss dielectric measurements in the frequency range 1 to 70 MHz by using a Vector Network Analyser". In: *Meas. Sci. Tech.* (2021). URL: https://doi.org/10.1088/1361-6501/abfd68.

[70] A. Khanna and Y. Garault. "Determination of loaded, unloaded, and external quality factors of a dielectric resonator coupled to a microstrip line". In: *IEEE Transactions on Microwave Theory and Techniques* 31.3 (1983), pp. 261–264. URL: https://doi.org/10.1109/tmtt.1983.1131473.

[71] R. E. Collin. *Foundations for microwave engineering*. McGraw-Hill series in electrical engineering. New York: McGraw-Hill, 2001.

[72] I. Besedin and A. P. Menushenkov. "Quality factor of a transmission line coupled coplanar waveguide resonator". In: *EPJ Quantum Technology* 5.1 (Jan. 2018). URL: https://doi.org/10.1140/epjqt/s40507-018-0066-3.

[73] C. R. H. McRae et al. "Materials loss measurements using superconducting microwave resonators". In: *Review of Scientific Instruments* 91.9 (Sept. 2020), p. 091101. URL: https://doi.org/10.1063/5.0017378.

[74] N. G. Ebensperger et al. "Characterizing dielectric properties of ultra-thin films using superconducting coplanar microwave resonators". In: *Review of Scientific Instruments* 90.11 (Nov. 2019), p. 114701. URL: https://doi.org/10.1063/1.5116904.

[75] S. Probst. *Resonator tools [Internet, cited 2021 Mar 25]*. URL: https://github.com/sebastianprobst/resonator_tools.

[76] *Evaluation of measurement data — Guide to the expression of uncertainty in measurement, JCGM 100:2008*. 2008. URL: https://www.bipm.org/utils/common/documents/jcgm/JCGM_100_2008_E.pdf.

[77] *Guide to the expression of uncertainty in measurement – Part 6: Developing and using measurement models, JCGM GUM6:2020*. 2020. URL: https://www.bipm.org/utils/common/documents/jcgm/JCGM_GUM_6_2020.pdf.

[78] U. Stumper. "Parameter evaluation of adapter from banana plugs to coaxial connector at MHz frequencies". In: *Electronics Letters* 25.17 (1989), p. 1174. URL: https://doi.org/10.1049/el:19890787.

[79] B. Williams. "Using the twin-T bridge to establish standards for Q and inductance at radio frequencies". In: *Proceedings of the British Electromagnetic Measurements Conference (NPL Teddington, UK), p23/1-4, 1987*.

[80] G. J. Hill. "Traceable dielectric measurements by resonance methods in the frequency range 1–30 MHz". In: *IEE Proceedings A Science, Measurement and Technology* 140.5 (1993), p. 382. URL: https://doi.org/10.1049/ip-a-3.1993.0059.

[81] Satish et al. “Evaluation of four-terminal-pair capacitance standards using electrical equivalent circuit model”. In: *Measurement* 73 (Sept. 2015), pp. 121–126. URL: https://doi.org/10.1016/j.measurement.2015.05.003.

[82] B. P. Kibble, J. M. Williams and L. C. A. Henderson (Eds.) *A guide to measuring resistance and impedance below 1MHz*. Tech. rep. The Institute of Measurement, Control, and The National Physical Laboratory, London, 1999. URL: https://eprintspublications.npl.co.uk/5450/.

[83] L. R. Arnaut and G. Gradoni. “Probability distribution of the quality factor of a mode-stirred reverberation chamber”. In: *IEEE Transactions on Electromagnetic Compatibility* 55.1 (Feb. 2013), pp. 35–44. URL: https://doi.org/10.1109/temc.2012.2213257.

[84] T. Moreno. *Microwave Transmission Design Data, 1st Ed.* Radio Communication Series. McGraw Hill, 1948.

[85] N. Bowler and Y. Huang. “Electrical conductivity measurement of metal plates using broadband eddy-current and four-point methods”. In: *Measurement Science and Technology* 16.11 (Sept. 2005), pp. 2193–2200. URL: https://doi.org/10.1088/0957-0233/16/11/009.

[86] D. Woods. “Immittance transformation using precision air-dielectric coaxial lines and connectors”. In: *Proceedings of the Institution of Electrical Engineers* 118.11 (1971), p. 1667. URL: https://doi.org/10.1049/piee.1971.0307.

[87] F. J. Tischer. “Excess surface resistance due to surface roughness at 35 GHz”. In: *IEEE Transactions on Microwave Theory and Techniques* 22.5 (May 1974), pp. 566–569. URL: https://doi.org/10.1109/tmtt.1974.1128285.

[88] G. Gold and K. Helmreich. “A physical surface roughness model and its applications”. In: *IEEE Transactions on Microwave Theory and Techniques* 65.10 (Oct. 2017), pp. 3720–3732. URL: https://doi.org/10.1109/tmtt.2017.2695192.

[89] J. Sheen. “Comparisons of microwave dielectric property measurements by transmission/reflection techniques and resonance techniques”. In: *Measurement Science and Technology* 20.4 (Jan. 2009), p. 042001. URL: https://doi.org/10.1088/0957-0233/20/4/042001.

[90] J. Sheen. “Amendment of cavity perturbation technique for loss tangent measurement at microwave frequencies”. In: *Journal of Applied Physics* 102.1 (July 2007), p. 014102. URL: https://doi.org/10.1063/1.2751484.

[91] M. Arai, J. G. P. Binner, and T. E. Cross. “Comparison of techniques for measuring high-temperature microwave complex permittivity: measurements on an alumina/zircona system”. In: *Journal of Microwave Power and Electromagnetic Energy* 31.1 (Jan. 1996), pp. 12–18. URL: https://doi.org/10.1080/08327823.1996.11688287.

[92] J. Krupka et al. “A dielectric resonator for measurements of complex permittivity of low loss dielectric materials as a function of temperature”. In: *Measurement Science and Technology* 9.10 (Oct. 1998), pp. 1751–1756. URL: https://doi.org/10.1088/0957-0233/9/10/015.

[93] J. Krupka et al. “Complex permittivity of some ultralow loss dielectric crystals at cryogenic temperatures”. In: *Measurement Science and Technology* 10.5 (Jan. 1999), pp. 387–392. URL: https://doi.org/10.1088/0957-0233/10/5/308.

[94] L. Hartshorn and W. H. Ward. “The measurement of the permittivity and power factor of dielectrics at frequencies from 10^4 to 10^8 cycles per second”. In: *Journal of the Institution of Electrical Engineers* 79.479 (Nov. 1936), pp. 597–609. URL: https://doi.org/10.1049/jiee-1.1936.0200.

[95] A. Kakimoto, I. Ogawa, and T. Matsushita. “Improvements on the measurements of dielectric constant and dissipation factor in a wide frequency range”. In: *Review of Scientific Instruments* 48.12 (Dec. 1977), pp. 1570–1575. URL: https://doi.org/10.1063/1.1134946.

[96] A. Sihvola. “Note on frequency dependence of quality factor of cavity resonators”. In: *Electronics Letters* 21.17 (1985), p. 736. URL: https://doi.org/10.1049/el:19850519.

[97] S. Ramo, J. R. Whinnery, and T. Van Duzer. *Fields and waves in communication electronics*. Radio Communication Series. Wiley, 1965.

[98] *BS Standard 4542:1970, Method for determination of loss tangent and permittivity of electrical insulating materials in sheet form (Lynch method)*. URL: https://www.en-standard.eu/bs-4542-1970-method-for-determination-of-loss-tangent-and-permittivity-of-electrical-insulating-materials-in-sheet-form-lynch-method/.

[99] *The expression of uncertainty and confidence in measurement (M3003)*. 2019. URL: https://www.ukas.com/wp-content/uploads/schedule_uploads/759162/M3003-The-Expression-of-Uncertainty-and-Confidence-in-Measurement.pdf.

[100] J. Baker-Jarvis et al. “Dielectric characterization of low-loss materials a comparison of techniques”. In: *IEEE Transactions on Dielectrics and Electrical Insulation* 5.4 (1998), pp. 571–577. URL: https://doi.org/10.1109/94.708274.

[101] J. Krupka. “Frequency domain complex permittivity measurements at microwave frequencies”. In: *Measurement Science and Technology* 17.6 (Apr. 2006), R55–R70. URL: https://doi.org/10.1088/0957-0233/17/6/r01.

[102] A. Imtiaz, T. M. Wallis, and P. Kabos. “Near-field scanning microwave microscopy: an emerging research tool for nanoscale metrology”. In: *IEEE Microwave Magazine* 15.1 (Jan. 2014), pp. 52–64. URL: https://doi.org/10.1109/mmm.2013.2288711.

[103] A. P. Gregory et al. “Measurement of the permittivity and loss of high-loss materials using a Near-Field Scanning Microwave Microscope”. In: *Ultramicroscopy* 161 (Feb. 2016), pp. 137–145. URL: https://doi.org/10.1016/j.ultramic.2015.11.015.

[104] A. P. Gregory et al. “Traceable measurement and imaging of the complex permittivity of a multiphase mineral specimen at micron scales using a microwave microscope”. In: *Ultramicroscopy* 172 (Jan. 2017), pp. 65–74. URL: https://doi.org/10.1016/j.ultramic.2016.11.001.

A Code Listings

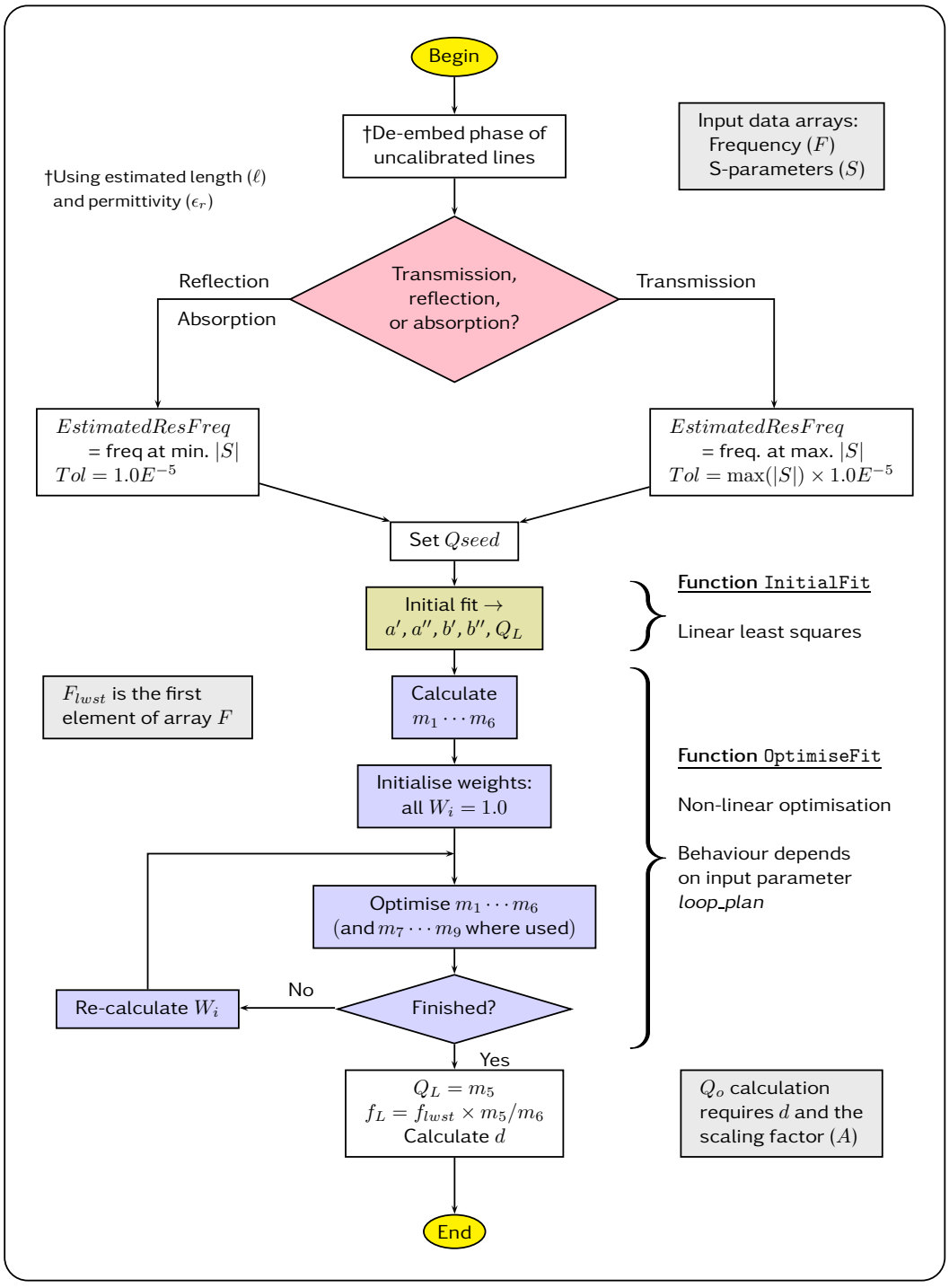

Figure 34: Flowchart of NLQFIT software for Q-factor fitting. Example Matlab computer code listings (compatible also with GNU Octave) that implement the bracketed sections of the flowchart are given below. NLQFIT6, NLQFIT7 and NLQFIT8 use different versions of the OptimiseFit function. Typically, NLQFIT6 is used for measurement by transmission, and NLQFIT7 for measurement by reflection. Python code listings that implement NLQFIT6 are also provided. It is recommended that the estimated value of loaded Q-factor (*Qseed*) should be within an order of magnitude of the actual value.

Listing 1: InitialFit function (Matlab/ GNU Octave)

```
%
% NLQFIT6, NLQFIT7 and NLQFIT8 Step (1).
% Linear least squares Q-factor fit.
% A reasonable estimate for the resonant frequency must be
% supplied. As this is not optimised in this function, the
% solution will only be approximate.
%
% This code listing is from:
%   "Q-factor Measurement by using a Vector Network Analyser",
%   A. P. Gregory, National Physical Laboratory Report MAT 58 (2021)
%
% Input data:
%    F                - Frequency array.
%    S                - Complex S-parameter data array.
%    N                - Number of points.
%    EstimatedResFreq - Estimate for resonant frequency.
%    Qseed            - Estimate for Q-factor QL.
%
% Output data:
%    sv = [a', a'', b', b'', QL]
%

N2 = 2*N;
X = zeros(5, N2);   % X is the transpose of M
G = ([1; N2]);

for i = 1:N
  i2 = i+N;
  t = 2.0*(F(i)/EstimatedResFreq - 1.0);
  y = 1.0/(1.0 + 1j*Qseed*t);
  v = t*y;
  X(1,i) = real(v);  X(1,i2) = imag(v);
  X(2,i) = -imag(v); X(2,i2) = real(v);
  X(3,i) = real(y);  X(3,i2) = imag(y);
  X(4,i) = -imag(y); X(4,i2) = real(y);
  v = t*y*S(i);
  X(5,i) = imag(v);  X(5,i2) = -real(v);
  v = y*S(i);
  G(i) = real(v);    G(i2) = imag(v);
end

M = X.';  % unweighted
C = X*M;
q = X*G;
sv = C\ q;
```

Source code is downloadable from https://doi.org/10.47120/npl.MAT58

An alternative Python implementation is available in the scikit-rf open-source library (implemented June 2022).

Listing 2: OptimiseFit6 function (Matlab/ GNU Octave)

```
function mv = OptimiseFit6(F, S, N, EstimatedResFreq, sv, ...
loop_plan, Tol, quiet)
%
% NLQFIT6 Step (2)
%   Optimised fit of Q-factor (QL) and resonant frequency (FL)
%   by the gradient-descent method.
%
% This code listing is from:
%          "Q-factor Measurement by using a Vector Network Analyser",
%          A. P. Gregory, National Physical Laboratory Report MAT 58 (2021)
%
% Input data:
%    F                - Frequency array.
%    S                - Complex S-parameter data array.
%    N                - Number of points.
%    EstimatedResFreq - Estimate for resonant frequency.
%    sv               - Solution vector found by initial linear fit.
%    loop_plan        - String of characters which defines order of
%                       steps used by the fitting process.
%                       E.g. 'fwfwc'.
%                       f - fit once without testing for convergence.
%                       c - repeated fit, iterating until convergence is
%                           obtained.
%                       w - re-calculate weighting factors on basis of
%                           previous fit.
%    Tol              - Criterion for the convergence test.
%                       Recommend using 1.0E-5 for reflection
%                       or max(abs(S))*1.0E-5 for transmission.
%    quiet            - Boolean flag controlling output of information to
%                       the console.
%
% Output data:
%    mv = [m1, m2, m4, m4, QL, FL]
%
N2 = N*2;
G = ([1; N2]);
PV = ones(N,1);
P = eye(N2);
m1 = sv(2)/sv(5);
m2 = -sv(1)/sv(5);
m3 = sv(3)-m1;
m4 = sv(4)-m2;
m5 = sv(5);
Flwst = F(1);   % lowest freq. is a convenient normalisation factor.
m6 = Flwst*m5/EstimatedResFreq;

for k = 1:length(loop_plan)

  op = loop_plan(k);
  if (op == 'w')       % Fr,        QL
    PV = AngularWts(F, Flwst*m5/m6, m5);
    PA = vertcat(PV,PV); % column vector
    P = diag(PA);
    if (~quiet)
```

```
      fprintf('Op␣w,␣␣Calculating␣weighting␣factors\n')
    end
    continue

  elseif (op == 'c')
    seek_convergence = 1;
  elseif (op == 'f')
    seek_convergence = 0;
  else
    disp('Unexpected␣character␣in␣loop_plan')
  end

  TerminationConditionMet = 0;
  Valid_RMS_Error = 0;
  Valid_Last_RMS_Error = 0;
  while (~TerminationConditionMet)
    X = zeros(6, N2); % X is transpose of matrix M
    for i = 1:N
      i2 = i+N;
      y = 1.0/(1.0 + 2j*(m6*F(i)/Flwst-m5));
      X(1,i) = 1.0;       X(1,i2) = 0.0;
      X(2,i) = 0.0;       X(2,i2) = 1.0;
      X(3,i) = real(y);   X(3,i2) = imag(y);
      X(4,i) = -imag(y);  X(4,i2) = real(y);
      u = (1j*m3-m4)*y*y*2;
      X(5,i) = real(u);   X(5,i2) = imag(u);
      u = -u*F(i)/Flwst;
      X(6,i) = real(u);   X(6,i2) = imag(u);
      v = m1+1j*m2 + (m3+1j*m4)*y;
      r = S(i) - v;                % residual
      G(i) = real(r);     G(i2) = imag(r);
    end
    M = X.';
    T = X*P;
    C = T*M;
    q = T*G;
    dm = C\q;          % solve for changes in m1..m6
    m1 = m1+dm(1);
    m2 = m2+dm(2);
    m3 = m3+dm(3);
    m4 = m4+dm(4);
    m5 = m5+dm(5);
    m6 = m6+dm(6);

    if (Valid_RMS_Error)
      Last_RMS_Error = RMS_Error;
      Valid_Last_RMS_Error = 1;
    end

    SumNum = 0.0;
    SumDen = 0.0;

    for i=1:N
      den = (1.0 + 2j*(m6*F(i)/Flwst-m5));
        E = S(i) - (m1+1j*m2) - (m3+1j*m4)/den;
        ip = PV(i);
```

```
        SumNum = SumNum + ip*(real(E)*real(E) + imag(E)*imag(E));
        SumDen = SumDen + ip;
      end
      RMS_Error = sqrt(SumNum/SumDen);
      Valid_RMS_Error = 1;

      if (~quiet)
        fprintunction: f('RMS␣Error␣%8.6f,␣QL␣%5.2f,␣FL␣%9.6f\n', ...
        RMS_Error,m5,Flwst*m5/m6)
      end

      if (seek_convergence)
        if (Valid_Last_RMS_Error)
          delta_S = abs(RMS_Error-Last_RMS_Error);
          TerminationConditionMet = (delta_S < Tol);
        end
      else
        TerminationConditionMet = 1;
      end


  end  % while loop
end  % for k loop

% Solution vector.
QL = m5;
FL = m5*Flwst/m6;
mv = [m1, m2, m3, m4, QL, FL];
```

Listing 3: AngularWts function (Matlab/ GNU Octave)

```
function PV = AngularWts(F, Fr, QL)

% The weights are needed when F consists of equally-spaced
% frequency points (rather than points equally spaced around
% the Q-circle). MAT 58  equation (28).

ptmp = 2.0*QL*(F-Fr)/Fr;
PV = 1./(ptmp.^2 + 1.0);
```

Listing 4: QCircleDiam function (Matlab/ GNU Octave)

```
function d = QCircleDiam(A, m1, m2, m3, m4)

% Return the diameter of the Q-circle
% MAT 58  equation (31).

aqratio = m1 + 1j*m2;
b = m1+m3 + 1j*(m2+m4);
d = abs(b - aqratio)*A;
```

Listing 5: OptimiseFit7 function (Matlab/ GNU Octave)

```
function mv = OptimiseFit7(F, S, N, EstimatedResFreq, sv, ...
loop_plan, Tol, quiet)
%
% NLQFIT7 Step (2)
%   Optimised fit of Q-factor (QL), resonant frequency (FL)
%   and a phase term related to the length of uncalibrated line.
%   Uses the gradient-descent method.
%
% This code listing is from:
%   "Q-factor Measurement by using a Vector Network Analyser",
%   A. P. Gregory, National Physical Laboratory Report MAT 58 (2021)
%
% Input data:
%    F                - Frequency array.
%    S                - Complex S-parameter data array.
%    N                - Number of points.
%    EstimatedResFreq - Estimate for resonant frequency.
%    sv               - Solution vector found by initial linear fit.
%    loop_plan        - String of characters which defines order of
%                       steps used by the fitting process.
%                       E.g. 'fwfwc'.
%                       f - fit once without testing for convergence.
%                       c - repeated fit, iterating until convergence is
%                           obtained.
%                       w - re-calculate weighting factors on basis of
%                           previous fit.
%    Tol              - Criterion for the convergence test.
%                       Recommend using 1.0E-5 for reflection
%                       or max(abs(S))*1.0E-5 for transmission.
%    quiet            - Boolean flag controlling output of information to
%                       the console.
%
% Output data:
%    mv = [m1, m2, m4, m4, QL, FL, m7/Flwst]
%
N2 = N*2;
G = ([1; N2]);
PV = ones(N,1);
P = eye(N2);
m1 = sv(2)/sv(5);
m2 = -sv(1)/sv(5);
m3 = sv(3)-m1;
m4 = sv(4)-m2;
m5 = sv(5);
Flwst = F(1);   % lowest freq. is a convenient normalisation factor.
m6 = Flwst*m5/EstimatedResFreq;
m7 = 0.0;

for k = 1:length(loop_plan)

  op = loop_plan(k);
  if (op == 'w')       % Fr,        QL
    PV = AngularWts(F, Flwst*m5/m6, m5);
    PA = vertcat(PV,PV); % column vector
```

```
  P = diag(PA);
  if (~quiet)
    fprintf('Op␣w,␣␣␣Calculating␣weighting␣factors\n')
  end
  continue
elseif (op == 'c')
  seek_convergence = 1;
elseif (op == 'f')
  seek_convergence = 0;
else
  disp('Unexpected␣character␣in␣loop_plan')
end

TerminationConditionMet = 0;
Valid_RMS_Error = 0;
Valid_Last_RMS_Error = 0;

while (~TerminationConditionMet)
  X = zeros(7, N2);   % X is transpose of matrix M
  for i = 1:N
    i2 = i+N;
    y = 1.0/(1.0 + 2j*(m6*F(i)/Flwst-m5));
    fdn = F(i)/Flwst - m5/m6;
    pj = 1j*m7*fdn;
    expm7 = exp(pj);
    ym = y*expm7;
    X(1,i) = real(expm7);      X(1,i2) = imag(expm7);
    X(2,i) = -imag(expm7);     X(2,i2) = real(expm7);
    X(3,i) = real(ym);         X(3,i2) = imag(ym);
    X(4,i) = -imag(ym);        X(4,i2) = real(ym);
    u = (1j*m3-m4)*y*ym*2;
    X(5,i) = real(u);          X(5,i2) = imag(u);
    u = -u*F(i)/Flwst;
    X(6,i) = real(u);          X(6,i2) = imag(u);
    fL = Flwst*m5/m6;
    v = ((m1+1j*m2) + (m3+1j*m4)*y)* expm7;
    u = v*fdn;
    X(7,i)=-imag(u);           X(7,i2)=real(u);
    r = S(i) - v; % residual
    G(i) = real(r); G(i2) = imag(r);
  end
  M = X.';
  T = X*P;
  C = T*M;
  q = T*G;
  dm = C\q;          % solve for changes in m1..m7
  m1 = m1+dm(1);
  m2 = m2+dm(2);
  m3 = m3+dm(3);
  m4 = m4+dm(4);
  m5 = m5+dm(5);
  m6 = m6+dm(6);
  m7 = m7+dm(7);

  if (Valid_RMS_Error)
    Last_RMS_Error = RMS_Error;
```

```
      Valid_Last_RMS_Error = 1;
    end

    SumNum = 0.0;
    SumDen = 0.0;

    for i=1:N
      fdn = F(i)/Flwst - m5/m6;
      den = 1.0 + 2j*(m6*F(i)/Flwst-m5);
      pj = 1j*m7*fdn;
      E = S(i) - ((m1+1j*m2) + (m3+1j*m4)/den)*exp(pj);
      ip = PV(i);
      SumNum = SumNum + ip*(real(E)*real(E) + imag(E)*imag(E));
      SumDen = SumDen + ip;
    end
    RMS_Error = sqrt(SumNum/SumDen);
    Valid_RMS_Error = 1;

    if (~quiet)
      fprintf('RMS Error %8.6f, QL %5.2f, FL %9.6f\n', ...
      RMS_Error,m5,Flwst*m5/m6)
    end

    if (seek_convergence)
      if (Valid_Last_RMS_Error)
        delta_S = abs(RMS_Error-Last_RMS_Error);
        TerminationConditionMet = (delta_S < Tol);
     end
     else
       TerminationConditionMet = 1;
     end

  end  % while loop
end  % for k loop

% Solution vector.
QL = m5;
FL = m5*Flwst/m6;
mv = [m1, m2, m3, m4, QL, FL, m7/Flwst];
```

Listing 6: InitialFit function (Python)

```
import numpy as np

def initialfit(F, S, N, Fres, Qseed):
    """
      Initial linear fit, step (1)
      ----------------------------

        NLQFIT6, NLQFIT7 and NLQFIT8 Step (1).

          Linear least squares Q-factor fit.
          A reasonable estimate for the resonant frequency must be
          supplied. As this is not optimised in this function, the
          solution will only be approximate.

        This code listing is from:
          "Q-factor Measurement by using a Vector Network Analyser",
          A. P. Gregory, National Physical Laboratory Report MAT 58 (2021)

        Input parameters:
          F     - List of frequencies.
          S     - List of complex S-parameter data to be fitted.
          N     - Number of points.
          Fres  - Estimated resonant frequency (not fitted).
          Qseed - Estimated QL (will be improved by fitting).

        Output data:
          sv = [a', a'', b', b'', QL]
    """

    N2 = 2*N;
    M = np.zeros([N2, 5])
    G = np.zeros(N2)[:, np.newaxis]

    for i in range(N):
        i2 = i+N
        t = 2.0*(F[i]/Fres - 1.0)
        y = 1.0/complex(1.0, Qseed*t)
        v = t*y
        v1 = y*S[i]
        G[i] = v1.real;    G[i2] = v1.imag
        v2 = v1*t
        M[i,:] = v.real, -v.imag, y.real, -y.imag, v2.imag
        M[i2,:] = v.imag, v.real, y.imag, y.real, -v2.real

    T = M.transpose() # unweighted
    C = np.dot(T,M)
    q = np.dot(T,G)
    sv = np.linalg.solve(C,q)
    return sv
```

Listing 7: OptimiseFit6 function (Python)

```
def optimisefit6(F, S, N, Fseed, sv, loop_plan, Tol, quiet):
    """
        Iterative non-linear fit, step, (2)
        -----------------------------------

        NLQFIT6 Step (2).
        Optimised fit of Q-factor (QL) and resonant frequency (FL)
        by the gradient-descent method.

        This code listing is from:
        "Q-factor Measurement by using a Vector Network Analyser",
        A. P. Gregory, National Physical Laboratory Report MAT 58 (2021)

        Uses the results of the initial fit (sv) as the starting
        values for the iteration.

        Input parameters:
          F     - List of frequencies.
          S     - List of complex data S-parameter to be fitted.
          N     - Number of points.
          Fseed - Estimated resonant frequency.
          sv    - Initial solution (numpy vector or a list) found
                  with InitialFit.

          loop_plan - String of characters which defines order of steps used
             by the fitting process e.g. 'fwfwc':
            f - fit once without testing for convergence.
            c - repeated fit, iterating until convergence is obtained.
            w - re-calculate weighting factors on basis of previous fit.

          Tol   - Criterion for the convergence test.
                  Recommend using 1.0E-5 for reflection
                  or max(abs(S))*1.0E-5 for transmission.

          quiet - Boolean flag controlling output of information to the
             console.

         Output (list of fitted parameters): [m1, m2, m3, m4, QL, FL].
    """

    if loop_plan[-1] == 'w': assert 0, 'Last item in loop_plan must not be w (
       weight calculation)'
    if loop_plan[0]  == 'w': assert 0, 'First item in loop_plan must not be w
       (weight calculation)'
    if loop_plan[-1] != 'c': print('Warning: Last item in loop_plan is not c
       so convergence not tested!')

    N2 = N*2;
    iterations = 0
    PV = np.ones(N)      # default weights vector
    PV2 = np.ones(N2)

    m1 = sv[1]/sv[4]  # a''/QL
    m2 = -sv[0]/sv[4]
```

```
m3 = sv[2]-m1
m4 = sv[3]-m2
m5 = sv[4]
Flwst = F[0]   # lowest freq. is a convenient normalisation factor.
m6 = Flwst*m5/Fseed
last_op = 'n'
del sv
weighting_ratio = None
number_iterations = 0

## Loop through all of the operations specified in loop_plan
for op in loop_plan:

    if op == 'w':           # Fr                          QL
        PV = angularwts(F, Flwst*float(m5)/float(m6), float(m5))
        weighting_ratio = max(PV)/min(PV)
        PV2 = np.concatenate((PV, PV))
        if not quiet: print('Op␣w,␣Calculate␣weights')
        last_op = 'n'
        continue

    if op == 'c': seek_convergence = True
    elif op == 'f': seek_convergence = False
    else: assert 0,'Unexpected␣character␣in␣loop_plan'

    TerminationConditionMet = False
    RMS_Error = None
    while not (TerminationConditionMet):
        number_iterations += 1
        M = np.zeros([N2, 6])   # X is the transpose of M
        G = np.zeros(N2)[:, np.newaxis]
        c1 = complex(-m4,m3); c2 = complex(m1,m2); c3 = complex(m3,m4)
        for i in range(N):
            i2 = i+N
            y = 1.0/complex(1.0,2*(m6*F[i]/Flwst-m5))
            u = c1*y*y*2
            u2 = -u*F[i]/Flwst
            M[i,:] = 1.0, 0.0, y.real, -y.imag, u.real, u2.real
            M[i2,:] = 0.0, 1.0, y.imag, y.real, u.imag, u2.imag
            v = c2 + c3*y
            r = S[i] - v  # residual
            G[i] = r.real; G[i2] = r.imag

        X = M.transpose()
        T = np.multiply(X, PV2)
        C = np.dot(T,M)
        q = np.dot(T,G)
        dm = np.linalg.solve(C,q)
        m1 += dm[0]; m2 += dm[1]; m3 += dm[2]
        m4 += dm[3]; m5 += dm[4]; m6 += dm[5]
        del G, X, T, C, dm
        iterations = iterations + 1
        if RMS_Error is not None: Last_RMS_Error = RMS_Error
        else: Last_RMS_Error = None

        SumNum = 0.0
```

```
            SumDen = 0.0
            for i in range(N):
                den = complex(1.0,2*(m6*F[i]/Flwst-m5));
                ip = PV[i]
                E = S[i] - complex(m1,m2) - complex(m3,m4)/den
                SumNum = SumNum + ip*(E.real*E.real + E.imag*E.imag)
                SumDen = SumDen + ip

            RMS_Error = math.sqrt(SumNum/SumDen);
            if not quiet:
                if last_op =='c':
                    print('␣␣␣␣␣␣␣Iteration␣%i,␣RMS_Error␣%10.8f' % (iterations
                        , RMS_Error))
                else:
                    print('Op␣%c,␣Iteration␣%i,␣RMS_Error␣%10.8f' % (op,
                        iterations, RMS_Error))
            last_op = op

            if seek_convergence:
                if Last_RMS_Error is not None:
                    delta_S = abs(RMS_Error-Last_RMS_Error)
                    TerminationConditionMet = delta_S < Tol
            else:
                TerminationConditionMet = True

        # After last operation, we end up here ...
        if not quiet: print()

    return [m1,m2,m3,m4,m5,m5*Flwst/m6], weighting_ratio,
           number_iterations, RMS_Error
```

Listing 8: AngularWts function (Python)

```
def angularwts(F, Fres, QL):
    """
        Calculate diagonal elements of weights matrix.
        -----------------------------------------------

          The weights are needed when F consists of equally-spaced
          frequency points (rather than points equally spaced around
          the Q-circle). MAT 58  equation (28).
    """

    F2 = np.array(F)
    ptmp = 2.0*QL*(F2-Fres)/Fres
    PV = 1.0/(ptmp**2 + 1.0);
    return PV
```

Listing 9: OptimiseFit7 function (Python)

```
def optimisefit7(F, S, N, Fseed, sv, loop_plan, Tol, quiet):
    """
        Iterative non-linear fit, step, (2)
        -----------------------------------

        NLQFIT7 Step (2).
        Optimised fit of Q-factor (QL), resonant frequency (FL)
        and a phase term related to the length of uncalibrated line.
        Uses the gradient-descent method.

        This code listing is from:
        "Q-factor Measurement by using a Vector Network Analyser",
        A. P. Gregory, National Physical Laboratory Report MAT 58 (2021)

        Uses the results of the initial fit (sv) as the starting
        values for the iteration.

        Input parameters:
          F     - List of frequencies.
          S     - List of complex data S-parameter to be fitted.
          N     - Number of points.
          Fseed - Estimated resonant frequency.
          sv    - Initial solution (numpy vector or a list) found
                  with InitialFit.

          loop_plan - String of characters which defines order of steps used
             by the fitting process e.g. 'fwfwc':
            f - fit once without testing for convergence.
            c - repeated fit, iterating until convergence is obtained.
            w - re-calculate weighting factors on basis of previous fit.

          Tol   - Criterion for the convergence test.
                  Recommend using 1.0E-5 for reflection
                  or max(abs(S))*1.0E-5 for transmission.

          quiet - Boolean flag controlling output of information to the
             console.

        Output (list of fitted parameters): [m1, m2, m3, m4, QL, FL,
                                             m7/Flwst].
"""

    if loop_plan[-1] == 'w': assert 0, 'Last item in loop_plan must not be w (
       weight calculation)'
    if loop_plan[0]  == 'w': assert 0, 'First item in loop_plan must not be w
       (weight calculation)'
    if loop_plan[-1] != 'c': print('Warning: Last item in loop_plan is not c
       so convergence not tested!')

    N2 = N*2;
    iterations = 0
    PV = np.ones(N)     # default weights vector
    PV2 = np.ones(N2)
```

```
m1 = sv[1]/sv[4]  # a''/QL
m2 = -sv[0]/sv[4]
m3 = sv[2]-m1
m4 = sv[3]-m2
m5 = sv[4]
Flwst = F[0]   # lowest freq. is a convenient normalisation factor.
m6 = Flwst*m5/Fseed
m7 = 0.0
last_op = 'n'
del sv
weighting_ratio = None
number_iterations = 0

## Loop through all of the operations specified in loop_plan
for op in loop_plan:

    if op == 'w':           # Fr                        QL
        PV = angularwts(F, Flwst*float(m5)/float(m6), float(m5))
        weighting_ratio = max(PV)/min(PV)
        PV2 = np.concatenate((PV, PV))
        if not quiet: print('Op␣w,␣Calculate␣weights')
        last_op = 'n'
        continue

    if op == 'c': seek_convergence = True
    elif op == 'f': seek_convergence = False
    else: assert 0,'Unexpected␣character␣in␣loop_plan'

    TerminationConditionMet = False
    RMS_Error = None
    while not (TerminationConditionMet):
        number_iterations += 1
        M = np.zeros([N2,7])
        G = np.zeros(N2)[:, np.newaxis]
        c1 = complex(-m4,m3); c2 = complex(m1,m2); c3 = complex(m3,m4)
        for i in range(N):
            i2 = i+N
            y = 1.0/complex(1.0,2*(m6*F[i]/Flwst-m5))
            fdn = F[i]/Flwst - m5/m6
            pj = complex(0.0, m7*fdn)
            expm7 = cmath.exp(pj)
            ym = y*expm7
            u = c1*y*ym*2
            u2 = -u*F[i]/Flwst
            v = (c2 + y*c3)* expm7;
            u3 = v*fdn;
            M[i,:] = expm7.real, -expm7.imag, ym.real, -ym.imag, u.real,
                u2.real, -u3.imag
            M[i2,:] = expm7.imag, expm7.real, ym.imag, ym.real, u.imag, u2
                .imag, u3.real
            r = S[i] - v  # residual
            G[i] = r.real; G[i2] = r.imag

        X = M.transpose()
        T = np.multiply(X, PV2)
        C = np.dot(T,M)
```

```
            q = np.dot(T,G)
            dm = np.linalg.solve(C,q)
            m1 += dm[0]; m2 += dm[1]; m3 += dm[2]
            m4 += dm[3]; m5 += dm[4]; m6 += dm[5]
            m7 += dm[6]
            del G, X, T, C, dm
            iterations = iterations + 1
            if RMS_Error is not None: Last_RMS_Error = RMS_Error
            else: Last_RMS_Error = None

            SumNum = 0.0
            SumDen = 0.0
            for i in range(N):
                fdn = F[i]/Flwst - m5/m6;
                den = complex(1.0, 2*(m6*F[i]/Flwst-m5))
                pj = complex(0.0,m7*fdn)
                E = S[i] - (c2 + c3/den)*cmath.exp(pj)
                ip = PV[i]
                SumNum = SumNum + ip*(E.real*E.real + E.imag*E.imag)
                SumDen = SumDen + ip

            RMS_Error = math.sqrt(SumNum/SumDen);
            if not quiet:
                if last_op =='c':
                    print('       Iteration %i, RMS_Error %10.8f' % (iterations
                        , RMS_Error))
                else:
                    print('Op %c, Iteration %i, RMS_Error %10.8f' % (op,
                        iterations, RMS_Error))
        last_op = op

        if seek_convergence:
            if Last_RMS_Error is not None:
                delta_S = abs(RMS_Error-Last_RMS_Error)
                TerminationConditionMet = delta_S < Tol
        else:
            TerminationConditionMet = True

    # After last operation, we end up here ...
    if not quiet: print()

return [m1,m2,m3,m4,m5,m5*Flwst/m6, m7/Flwst], weighting_ratio,
    number_iterations, RMS_Error
```